공학박사학위논문

Computationally Efficient Simulation and Optimization Strategies for Design of Multiphase Chemical Reactors with Complex Dynamics

복잡한 동특성을 갖는 다상 반응기의 설계를 위한 계산 효율적인 모사 및 최적화 전략

2020 년 2 월

서울대학교 대학원

화학생물공학부

박 성 언

Abstract

Computationally Efficient Simulation and Optimization Strategies for Design of Multiphase Chemical Reactors with Complex Dynamics

Seongeon Park
School of Chemical & Biological Engineering
The Graduate School
Seoul National University

This thesis presents a design strategy for industrial-scale chemical reactors which consists of multi-scale modeling, post-modeling calibration, and optimization. Although the reactor design problem is a primary step in the development of most chemical processes, it has been relied on simple models, experiments and rules of thumbs rather than taking advantage of recent numerical techniques. It is because industrial-size reactors show high complexity and scale differences both physically and chemically, which

makes it difficult to be mathematically modeled. Even after the model is constructed, it suffers from inaccuracies and heavy simulation time to be applied in optimization algorithms.

The complexity and scale difference problem in modeling can be solved by introducing multi-scale modeling approaches. Computational fluid dynamics (CFD)-based compartmental model makes it possible to simulate hours of dynamics in large size reactors which show inhomogeneous mixing patterns. It regards the big reactor as a network of small zones in which perfect mixing can be assumed and solves mass and energy balance equations with kinetics and flow information adopted from CFD hydrodynamics model at each zone. An aqueous mineral carbonation reactor with complex gas–liquid–solid interacting flow patterns was modeled using this method. The model considers the gas-liquid mass transfer, solid dissolution, ionic reactions, precipitations, hydrodynamics, heat generation and thermodynamic changes by the reaction and discrete operational events in the form of differential algebraic equations (DAEs). The total CO_2 removal efficiency, *p*H, and temperature changes were predicted and compared to real operation data. The errors were within 7 % without any post-adjustment.

The inaccuracy problem of model can be overcome by post-modeling approach, such as the calibration with experiments. The model for aqueous

mineral carbonation reactor was intensified via Bayesian calibration. Eight parameters were intrduced in the uncertain parts of the rigorous reactor model. Then the calibration was performed by estimating the parameter posterior distribution using Bayesian parameter estimation framework and lab-scale experiments. The developed Bayesian parameter estimation framework involves surrogate models, Markov chain Monte Carlo (MCMC) with tempering, global optimization, and various analysis tools. The obtained parameter distributions reflected the uncertain or multimodal natures of the parameters due to the incompleteness of the model and the experiments. They were used to earn stochastic model responses which show good fits with the experimental results. The fitting errors of all the 16 datasets and the unseen test set were measured to be comparable or lower than when deterministic optimization methods are used.

The heavy simulation time problem for mathematical optimization can be resolved by applying Bayesian optimizaion algorithm. CFD based optimal design tool for chemical reactors, in which multi-objective Bayesian optimization (MBO) is utilized to reduce the number of required CFD runs, is proposed. The developed optimizer was applied to minimize the power consumption and maximize the gas holdup in a gas-sparged stirred tank reactor, which has six design variables. The saturated Pareto front was

obtained after only 100 iterations. The resulting Pareto front consists of many near-optimal designs with significantly enhanced performances compared to conventional reactors reported in the literature.

It is anticipated that the suggested CFD-based compartmental modeling, post-modeling Bayesian calibration, and Bayesian optimization methods can be applied in general industrial-scale chemical reactors with complex physical and chemical features.

Keywords: Reactor; Reactor modeling; CFD reactor model; CFD-based compartmental model; Bayesian parameter estimation; Bayesian optimization, Optimal reactor design; Aqueous mineral carbonation; Carbon Capture Utilization & Storage (CCUS)

Student Number: 2015-21062

Contents

Abstract i

Contents v

List of Figures viii

List of Tables xii

1. Introduction 1

    1.1. Industrial-scale chemical reactor design 1

    1.2. Role of mathematical models in reactor design 2

    1.3. Intensification of reactor models through calibration 5

        1.3.1. Bayesian parameter estimation 6

    1.4. Optimization of the reactor models 7

        1.4.1. Bayesian optimization 9

    1.5. Aqueous mineral carbonation process : case study subject 10

    1.6. Outline of the thesis 12

2. Multi-scale modeling of industrial-scale aqueous mineral carbonation reactor for long-time dynamic simulation 14

    2.1. Objective 14

    2.2. Experimental setup 15

    2.3. Mathematical models 19

        2.3.1. Reactor model 19

        2.3.2. CFD model 28

        2.3.3. Numerical setting 30

    2.4. Results and discussions 32

        2.4.1. CFD-based compartmental model for industrial-scale reactor. 32

        2.4.2. Design and simulation of higher-scale reactors 42

2.5. Conclusions 47

3. Model intensification of aqueous mineral carbonation kinetics via Bayesian calibration 50

3.1. Objective 50

3.2. Experimental methods 51

3.2.1. Solution and gas preparation 51

3.2.2. Laboratory-scale mineral carbonation process 53

3.3. Mathematical models 56

3.3.1. Kinetics of aqueous mineral carbonation process 56

3.3.2. Differential algebraic equation (DAE) model for the reactor 65

3.3.3. Discrete events for simulation procedure 71

3.3.4. Numerical setting 72

3.4. Bayesian parameter estimation 72

3.4.1. Problem formulation 73

3.4.2. Bayesian posterior inference 76

3.4.3. Sampling 81

3.5. Results and discussions 82

3.5.1. Stochastic output response 82

3.5.2. Quality of parameter estimtates 86

3.5.3. Assessment of parameter uncertainties 91

3.5.4. Kinetics study with the proposed model parameters 99

3.6. Conclusions 103

4. Multi-objective optimization of chemical reactor design using computational fluid dynamics 106

4.1. Objective 106

4.2. Problem Formulation 107

4.3. Optimization scheme 113

4.3.1. Multi-objective optimization algorithm 113
4.3.2. CFD-MBO optimizer 120
4.4. CFD modeling 125
4.4.1. Tank specifications 125
4.4.2. Governing equations 125
4.4.3. Simulation methods 127
4.5. Results and discussion 128
4.5.1. CFD model validation 128
4.5.2. Optimization results 130
4.5.3. Analysis of optimal designs 139
4.6. Conclusions 144
5. Concluding Remarks 146
Bibliography 149
Abstract in Korean (국문초록) 163

List of Figures

Figure 2-1. Side and top views of industrial-scale reactor and configuration of nozzle. 17

Figure 2-2. Systematic diagram for CFD-based compartmental model..... 22

Figure 2-3. CO_2 holdup profiles of the CFD-based compartmental model in 119-zone (left), 179-zone (middle), and 291-zone (right) models in Experiment I-1 2nd reactor..... 33

Figure 2-4. Side and top view of the 179-zone model in the industrial-scale reactor. 34

Figure 2-5. Model results compared with operation data from (a) Experiment I-1 and (b) Experiment I-2..... 35

Figure 2-6. Concentration changes of involved species during Experiment I-1..... 39

Figure 2-7. CO_2 volume fraction changes at each zone during the operation..... 41

Figure 2-8. Side and top views of Type A (gas inlet 17,500 Nm^3/hr) and Type B (gas inlet 70,000 Nm^3/hr) reactors..... 43

Figure 2-9. Top) Side and top view of the 181 compartments for Type A reactor, Bottom) Side and top view of the 164 compartments for Type B reactor. 45

Figure 2-10. Predicted dynamic behaviors of Type A and Type B reactors. 46

Figure 3-1. Schematic process flow diagram of aqueous mineral carbonation process for CO_2 absorption and utilization. 55

Figure 3-2. Schematic diagram of the compartment reactor model..... 66

Figure 3-3. Schematic diagram of the problem setting. 74

Figure 3-4. (a) A graphical representation of model generation. The observed response is considered as a noisy version of the modeled (ideal) response. (b) Schematic for the Bayesian inference. 78

Figure 3-5. : a) Estimated output response (($\boldsymbol{\phi}_{\boldsymbol{CO2}}^{\boldsymbol{outlet}}$ fitting and b) joint marginal posterior distribution of $\mathbf{log_{10}}(\boldsymbol{\theta}_{\boldsymbol{k_l}})$ and $\mathbf{log_{10}}(\boldsymbol{\theta}_{\boldsymbol{A_s}})$ for Exp. 6 using mode, mean, and optimization method. 83

Figure 3-6. Tempering control (tempering factor as 1, 4, 8, and 10 respectively) for checking multimodal posterior distribution between $\boldsymbol{\theta}_{\boldsymbol{A_s}}$ and $\boldsymbol{\theta}_{\boldsymbol{k_l}}$; also compare the $\boldsymbol{\theta}_{\boldsymbol{mean}}$ and $\boldsymbol{\theta}_{\boldsymbol{mode}}$ movements. × denotes mean and + denotes mode. 85

Figure 3-7. Estimated output response ($\boldsymbol{\phi}_{\boldsymbol{CO2}}^{\boldsymbol{outlet}}$) fitting with experimental data, $\mathbf{f}_{\boldsymbol{mean}}$, $\mathbf{f}(\boldsymbol{\theta}_{\mathbf{mode}})$, $\mathbf{f}(\boldsymbol{\theta}_{\mathbf{mean}})$, and $\mathbf{f}(\boldsymbol{\theta}_{\mathbf{opt}})$. Uncertainty quantification using standard deviation and confidence interval is also conducted.... 87

Figure 3-8. Estimated output response (pH) fitting with experimental data, $\mathbf{f}_{\boldsymbol{mean}}$, $\mathbf{f}(\boldsymbol{\theta}_{\mathbf{mode}})$, $\mathbf{f}(\boldsymbol{\theta}_{\mathbf{mean}})$, and $\mathbf{f}(\boldsymbol{\theta}_{\boldsymbol{opt}})$. Uncertainty quantification using standard deviation and confidence interval is also conducted. 88

Figure 3-9. Error comparison through different parameter estimation methods. Visualize the error with a) CO_2 volumetric concentration of outlet flue gas ($\boldsymbol{\phi}_{\boldsymbol{CO2}}^{\boldsymbol{outlet}}$) and b) pH..... 89

Figure 3-10. Two dimentional joint marginal posterior distribution with 20,000 final samples of MCMC. The center of dotted crosslines is $\boldsymbol{\theta}_{\boldsymbol{mean}}$. 92

Figure 3-11. Marginal posterior distributions of each parameter from different kinds of datasets. Each gray line corresponds to the posterior which is inferred from two responses data from same experiment. 93

Figure 3-12. Two dimentional joint marginal posterior distribution with tempering factor (tmp=10). The center of dotted crosslines is $\boldsymbol{\theta}_{\boldsymbol{mean}}$. 94

Figure 3-13. Tempering control (tempering factor as 1, 4, 8, and 10 respectively) for checking multimodal posterior distribution between $\boldsymbol{\theta_{A_s}}$ and $\boldsymbol{\theta_{d_{s0}}}$; also compare the $\boldsymbol{\theta_{mean}}$ and $\boldsymbol{\theta_{mode}}$ movements. × denotes mean and + denotes mode. 98

Figure 3-14. The sensitivity analysis of design variables. While one design variable is perturbed at a time within a range of the specified low and high values, the other variables are fixed to the median value of the operating range, i.e. $\boldsymbol{T}$ to 46.5 ∘C, $\boldsymbol{\phi_{CO2}^{inlet}}$ to 16 %, $\boldsymbol{w_{Ca(OH)_2}}$ to 2 wt%, $\boldsymbol{w_{NaOH}}$ to 1.5 wt%, and $\boldsymbol{V}$ to 1.25 L/min. The perturbation is conducted to have same interval between the values. 100

Figure 3-15. The case study results using the estimated parameter values. 102

Figure 4-1. (a) Base design of a gas-sparged stirred tank reactor and (b) design parameters of the reactor. 108

Figure 4-2. Graphical illustration of the role of CFD as black-box performance functions. 112

Figure 4-3. Graphical illustration of EI. 119

Figure 4-4. Algorithm of CFD-MBO optimizer. 121

Figure 4-5. Implementation of CFD-MBO optimizer using STK toolbox, MATLAB, and Ansys software. 124

Figure 4-6. Comparison between the modeling and experimental local gas holdup data. 129

Figure 4-7. (a) Advance of the Pareto front as the number of iteration increases, (b) the trend of the first objective function ($\boldsymbol{power(x)^{0.4}}$) values along the iterations, and (c) the trend of the second objective function ($\boldsymbol{20 - egh(\mathbf{x})}$) values along the iterations. 131

Figure 4-8. Saturation of Pareto front with respect to the concept of dominated hypervolume. 132

Figure 4-9. Optimization results (a) in the objective function space and (b) with respect to the original performance functions. 135

Figure 4-10. Relationship between the impeller diameter and power consumption based on the data obtained during the optimization. 138

Figure 4-11. (a) The location of each group in the objective function space, (b) the structures and 2D contours of a gas holdup in good initial designs, (c) the structures and 2D contours of the gas holdup in the reference designs, and (d) the structures and 2D contours of the gas holdup in overwhelming optimal designs. 140

Figure 4-12. Liquid velocity vector space in reactors shown in Figure 4-11..... 142

Figure 5-1. Optimal design process of industrial-scale chemical reactor. 148

List of Tables

Table 2-1. Experimental conditions for industrial-scale process. 18

Table 3-1. 2-(4,5,1) orthogonal array experiment design..... 52

Table 3-2. Kinetic parameters for solid dissolutions..... 60

Table 3-3. Kinetic parameters of the ionic reactions..... 62

Table 3-4. Kinetic parameters for precipitations..... 64

Table 3-5. The prior range for the parameter $\boldsymbol{\theta}$ 80

Table 4-1. Pseudo code for general Bayesian optimization concept [111]. 115

Table 4-2. Detailed specifications and the performances of the initial, reference, and optimal reactors..... 141

Chapter 1.

Introduction

1.1. Industrial-scale chemical reactor design

The design of a chemical reactor is the most essential task in the development of a chemical process. In the conventional hierarchical process design process, the analysis of chemical reactors comes first followed by the investigation of separation and recycle, heat exchanger network and utilities, in turn. The other periphery units are designed after the performance of the reactors such as yield or selectivity as well as the mass and energy balances at the reactors are derived. However, the complexity of the phenomena taken place in the reactors make it hard to model and design them properly.

Engineers have achieved a rough insight of reactor designs from reaction engineering principles. Calculating the necessary residence time of the reactants and deciding the size of reactors can be done based on those principles. Engineers have then relied on experiments and empirical knowledge to develop the final design from the initial specifications. In case of conventional reactor types such as stirred tank reactors, bubble column reactors and fixed bed reactors, a lot of correlations between the design parameters and transport phenomena have been provided. Also, there are rules of thumbs for deciding design parameters such as the location and size of impellers in stirred tank reactors.

For the industrial-scale reactors, the design process starts from smaller units; it is rather referred to ‘scale-up’ because laboratory-, pilot-scale tests are indispensable before realizing the full-scale unit. In laboratory-scale experiments, basic information about the system that does not depend on the size such as thermodynamics and kinetics are to be obtained. In pilot-scale experiments, operational aspects such as equipment reliability or impurities in the materials as well as the physical aspects such as inhomogeneous flow and heat patterns and their interactions with chemical mechanisms must be revealed. Maintaining the similarity of important process variables and dimensionless groups between different scales is a primarily accepted scale-up method, which is also referred as dimensional and model analysis in general design problems.

1.2. Role of mathematical models in reactor design

In scale-up problems, the dimensional similitude approach shows a limitation on providing direct quantitative prediction on the performance of scaled-up reactors. It is rather expecting the scaled-up designs to show the similar performance proved from the experiments of smaller scales by maintaining indirect parameters in similar magnitude. It is also not always possible to derive the design which satisfies all the similarity criteria; sometimes engineers intuitively choose with experiences which criteria to apply or ignore.

Mathematical modeling of reactors can help overcoming these problems by providing full view of the system. It is possible to predict the most important features and even unmeasurable variables of the system. Furthermore, it enables engineers to

explore various alternative designs which are timely and costly prohibitive in physical experiments. Such exploration sometimes can reveal an innovative design idea that cannot be derived from heuristics. In addition, if the developed model is combined with mathematical optimization algorithms or integrated with process models, further improvement of the performance is possible.

Mathematical chemical reactor modeling starts from setting up mass and energy balance equations of the system in interest. Identifying the reactions kinetics and integrating them with the mass and energy balance equations are the next step. Then the transport phenomena of fluid, heat and mass must be considered. The resulting model is composed of a set of differential algebraic equations, or partial differential equations in case of describing full transport phenomena, which requires numerical methods to get a solution. Obtaining the numerical solutions of governing equations of transport phenomena, i.e. Navier-Stokes equation, is a challenging task that has been established as an academic field called computational fluid dynamics (CFD).

CFD model

Over the last decades, CFD has become a popular tool for reactor modeling owing to its ability to analyze the transport phenomena and evaluate the physical features of a certain design without real experiments. An abundance of studies have shown the results of CFD modeling with experimental validations in various types of reactors, such as in stirred tank reactors [1] bubble column reactors [2], and fixed bed tubular reactors [3]. Several research papers have shown the capacity of CFD in modeling the mass-transfer process [4, 5] and the reaction kinetics [6]. Beyond reproducing the transport phenomena, a number of studies have reported improvements in the reactor

designs with the aid of CFD through case studies, a sensitivity analysis, or a simple statistical analysis [7-10].

However, CFD simulations in current status have limitations on considering more than a couple of reactions owing to numerical instability and exorbitant simulation time, which poses a serious incapability in representing overall perspective of chemical reactors. In addition, CFD simulations of industrial-scale unit is too expensive due to huge number of calculation elements (meshes) and presence of strong turbulence to simulate more than a few tens of seconds. Therefore, full CFD simulation is an impossible option for batch reactors which haves operational cycle of more than hours.

CFD-based compartmental model

In such cases, traditional methods, such as a compartmental model or network-of-zones model, which are to account for the fluid dynamics in simplified ways have been employed [11]. Compartmental model regards a reactor as a network of hundreds of zones in which homogeneous conditions are satisfied as in a concept of continuous stirred-tank reactor [12] and between which the flow rates are estimated based on impeller conditions. Vrabel et al. [13, 14] and Zahradnik et al. [15] used this method to model large scale gas-liquid fermentation and bioreactors.

However, the compartmental model necessarily has a limitation in accuracies. Particularly in multiphase reactors [16], the flow rates of secondary phase is complicated to estimate. Unlike the liquid flow rates in single liquid phase reactors, which can be relatively well predicted from the impeller speed, the gas flow rates in gas-liquid reactors are complicated to estimate because they are affected by numerous

factors; not only by impeller rotational force but also buoyance force as well as a complex gas sparger configuration.

Combining CFD and the zonal method makes it possible to overcome the inaccuracy problem of the zonal method as well as to extend the limit of possible simulation time in CFD. This combined model is referred to as the CFD-based compartmental model [17, 18], which can also be regarded as a branch of multi-scale model. In the CFD-based compartmental model, mass flow rates between the zones are brought from the CFD model, instead of estimating them from empirical correlations. It is assumed that the steady-state hydrodynamics resulting from CFD simulations is not affected by the progress of reactions. Bezzo et al. [19] first reported the implementation of this method in a bioreactor. Other reports include the applications in the ozone process and CO_2 and $Ca(OH)_2$ precipitation reactor [20, 21].

1.3. Intensification of reactor models through calibration

Mathematical models or computer models always show deviated predictions from the actual plant operations, which is also called as model errors. Furthermore, the models are usually constructed to cover a wide range of conditions. Thus, to intensify the model in its accuracy or for the application in specific conditions, post-modeling calibration is recommended. The calibration can also be called as the parameter estimation because the model contains a few unknown parameters to adjust the model output, or to narrow down the applicable range to particular conditions; and the calibration can be done by estimating those unknown parameters. To learn the

unknown parameters, observations, or experiments in most of chemical engineering problems, are to be obtained and parameters are found to best-fit these observations.

1.3.1. Bayesian parameter estimation

Bayesian parameter estimation can find the posterior probabilistic distributions of the parameters by taking account of their distributed natures as well as the measurement errors of the experiments. The model can then be updated to a stochastic model using uncertainty quantification methods [22, 23] and used for stochastic model predictive control (SMPC) [24, 25]. Although there is no general Bayesian parameter estimation framework available, it is able to find a lot of applications in many different fields including chemical engineering [26, 27], carbon mitigation [28, 29], bioengineering [30], cognitive science [31], cosmology [32], electrical/ electronic engineering [33], and artificial intelligence [34]. One challenge of Bayesian estimation is that a huge amount of samples are required. Thus, when the computational load of the model is too expensive, function approximation methods such as second order polynomial [27, 35] and polynomial chaos expansion (PCE)[26, 36] are adopted together. Another big challenge is dealing with the multiple datasets with different levels of uncertainties. Experiments are usually performed under varying conditions (or design variables), so the amount of data and uncertainty inevitably varies as well. Therefore, a proper Bayesian parameter estimation framework which can handle these problems is demanded to resolve the issues in chemical engineering, particularly in mineral carbonation technology.

1.4. Optimization of the reactor models

The increasing capacity of computational tools have made engineers to apply computer modeling approach in actual applications. The mathematical chemical reactor models can be used to derive the optimal design, while the heuristic design process leads to safe, traditional, but suboptimal designs.

The increasing capacity of CFD as a modeling and design tool for reactors naturally leads to the desire for the systematic optimization of the CFD results. This task is referred to as CFD-based optimization, whose applications are more commonly found in other areas than chemical engineering, such as in aircraft designs. A large branch of CFD-based optimization is gradient-based optimization using an adjoint method [37]. Representative works applying this method include the design of wings to minimize the drag and maximize the lift [38], and the design of full aircraft configurations [39]. As with other gradient-based algorithms, intrinsic disadvantages of a local solver are incurred, although the local optima are quickly found. More critically, the identification of a consistent adjoint system is required prior to optimization, which is currently unattainable for complex systems such as a turbulent multiphase flow in a chemical reactor.

Another branch is simulation-based optimization (SBO), which does not require gradient information. This treats a CFD model as a black-box function between design variables and output results. Evolutionary algorithms (EAs) are a widely adopted SBO in CFD-based problems, particularly in multi-objective problems. Algorithms such as NSGA-II [40] or MOGA-II [41] are known to provide a set of trade-off solutions and are easily implemented with any independent simulation. A

few examples applying CFD-based reactor optimization have also employed these methods. A previous research [42] used MOGA-II to maximize the H_2/CO ratio and minimize the outlet temperature in a quench conversion reactor. Another one [43] optimized the topology of two impellers installed in a gas–liquid stirred tank using CFD and the NSGA-II method. Na et al. [44] integrated the genetic algorithm (GA) and ε-constraint method to simultaneously optimize the productivity and maximum temperature at the microchannel reactor using a 2D axisymmetric CFD model, which is represented using mixed integer non-linear programming (MINLP). However, the critical drawback of using EAs is that they require a significantly large number of expensive CFD runs.

Approaches used to minimize the number of CFD runs are developed to avoid this drawback. Adaptive hybrid methods [45], which couple population-based algorithms with gradient-based local searching methods, have been adopted in many aerospace and automotive engineering studies [46, 47]. Replacing expensive CFD simulations with cheap surrogate models, such as polynomial functions, radial basis functions, a neural network, or a Gaussian process, is another good approach. For an example, Jung et al. [48] optimized the geometry of a guiding fin at the Fischer-Tropsche microchannel reactor using a neural network surrogate model trained based on the CFD results. However, because this method starts the optimization after creating the complete surrogate model, it is necessary to evaluate the points that far from the optimum. This necessarily increases the number of CFD evaluations. An improved method is to use population-based EAs with a surrogate model [49]. In each population, the surrogate model evaluates the elements, picking out only the best-

fitted ones to undergo CFD evaluations. One group [50] successfully optimized a quench conversion reactor using CFD and a FAST optimizer [51], which is a surrogate-based EA, within a small number of iterations. However, the algorithms based on EAs rely on randomness in both exploration and exploitation when searching for new elements to evaluate. Thus, there is still further room to reduce the number of iterations using mathematically rigorous searching methods based on the probability.

1.4.1. Bayesian optimization

Bayesian optimization (BO) can be an effective tool for CFD-based optimization in that it purses the maximum efficiency through a solid theoretical background [52]. BO refers to a class of gradient-free global optimization algorithms, which use a Gaussian process (GP) as a surrogate model, and find a next candidate of the evaluation using the probabilistic information of the model. It also offers multi-objective [53, 54], constrained [54, 55], and even transfer-learning multi-task optimizations [56]. Although successful applications other than CFD exist, which also require expensive evaluations [57-60], only a limited number of studies have been conducted on CFD-based optimizations [61]. In particular, no studies have been reported for a reactor design optimization.

1.5. Aqueous mineral carbonation process : case study subject

Throughout this thesis, many computer-aided design approaches such as modeling, model intensification and optimization are proposed and applied in aqueous mineral carbonation process. This section provides the introduction as well as the precedent process systematic studies about mineral carbonation process.

Carbon capture and utilization or carbon conversion and utilization (CCU) technology have recently drawn attentions in both industry and academia because of their economic and environmental potentials [62, 63]. Current development progress of CO_2 utilization is at the technology readiness level 6 (TRL6), which is the stage of pilot plant demonstration [62].

There are several categories of technology under CCU that can convert CO_2 to useful chemicals and fuels. Some of them use electro-catalytic, photo-electrochemical, photo-catalytic, and thermochemical reduction [64], and others use CO_2 as a feedstock to produce various chemical products such as urea, methanol, and salicylic acid [63]. Mineral carbonation, one of promising CCU technologies, captures CO_2 in the form of mineral carbonates that can be fabricated as building compartments after post-processing [65, 66]. It is proved to be at least carbon-neutral, and carbon-negative when atmospheric CO_2 is used as feedstock. The advantages of this technology are manifold. First, it can directly use the flue gas from power plants or incineration plants without any preprocessing steps. Second, it can use the industrial wastes such as steel slags, fly ash, wastewater and brine as mineral sources [65, 67]. In addition, the solid carbonate products are thermodynamically stable and have a mature market as construction materials to anticipate the economic potentials [67].

Several companies have been actively engaged in the development of mineral carbonation process and made visible progress. Regarding industrial applications, an Australian based start-up, Mineral Carbonation International (MCi), invested by Orica since 2013, has operated CO_2 mineral carbonation pilot plant since 2016 [68]. They announced a plan to construct a full-scale production plant (20,000-50,000 tons/year of carbonate and silica by-products) by 2020 [69]. The pilot plants of Calera Corporation capture up to 2 tons/day of CO_2 into calcium carbonate product directly from the raw flue gas from power plants. They also constructed a commercial fiber cement board line integrated with the mineral carbonation pilot plant to produce full-size fiber cement board sheets [70]. The Carbon Capture Machine developed by the University of Aberdeen has reached TRL4, currently producing 200 kg/day of precipitated calcium carbonates. COSIA Carbon XPRIZE Challenge, which was launched in 2015, is now supporting its further development to TRL6 demonstration plant [71]. Daewoo E\&C in South Korea developed and operated a pilot plant which can capture 10 tons/day of CO_2 in 2012. They built the scaled-up plant which can process 40 tons/day of CO_2 in 2017 [72, 73], in which the authors have participated. U.K. start-up Carbon8 has a facility which treats 2,000 tons/year of CO_2 and produces building aggregates using wastes such as ashes from municipal incinerators and energy plants [74].

Although a lot of effort is being made to commercialize mineral carbonation processes as the main technology of CCU, there still remain challenges. First, the reaction rates are slow due to the mass transfer resistance between different phases - the system involves the dissolutions of mineral and hydroxide ions from the solid

reactants, e.g. $Ca(OH)_2$, and carbonate ions from the flue gas. In order to overcome the slow reaction rates, it is essential to optimize the reactants and the design of the reactor by modeling the entire reaction kinetics including the interphase mass transfer. The good reactor design can help accelerate the mass transfer rates by homogeneously distributing the gas bubbles and solid particles. Many studies on mineral carbonation kinetics and the reaction parameters have been reported and verified with experimental results [75]. All of them used deterministic methods for the parameter estimation and suggested deterministic values which best fit their experimental results. However, some of the parameters, especially the ones related to hydrodynamics and mass transfer, are likely to have different values under different operating conditions and disturbances, such as the fluctuation of the CO_2 concentration in the flue gas, the inhomogeneous size distributions of solid particles. Therefore, the use of the deterministic parameters in the model may hinder the accurate predictions of output responses.

1.6. Outline of the thesis

This thesis suggests computer modeling-oriented strategies to design industrial-scale chemical reactors; optimal reactor designs can be derived through modeling, model intensification (calibration) and optimization. Chapter 1 discusses the necessity of this approach and discussed the previous researches and their issues. Chapter 2 outlines the ability of CFD-based compartmental model in simulating the long-term dynamic behaviors of the industrial-scale aqueous mineral carbonation reactor. Chapter 3 provides a successful example of application of Bayesian

calibration in aqueous mineral carbonation process. It discusses practical tips and procedures to apply this method in general chemical kinetics model intensification problems. Chapter 4 proposes a strategy to optimize expensive reactor models, particularly CFD models, and apply it to gas-liquid stirred reactor. Finally, Chapter 5 illustrates the implication of this thesis as well as briefly summarize the previous chapters.

Chapter 2.

Multi-scale modeling of industrial-scale aqueous mineral carbonation reactor for long-time dynamic simulation[#]

2.1. Objective

This chapter introduces the CFD-based compartmental model to simulate industrial-scale mineral carbonation reactors with complex gas sparger configurations and high gas throughputs. In the CFD-based compartmental model, the CFD model calculates the mass flow rates of the gas between the zones, and then mass balance equations with the kinetics are formulated as a set of differential algebraic equations (DAEs) for each zone. The energy balance equation for the entire reactor is also developed to consider the temperature dependency of the system. Although there have been several attempts to model the kinetics of this system [76-78], this is the first study to integrate the CFD information and the heat balance model.

[#] This chapter cites the author's submitted journal article under review: Kim, M., Park, S., Lee, D., Lim, S., Park, M., & Lee, J. (2020). Modeling long-time behaviors of industrial multiphase reactors for CO_2 capture using CFD-based compartmental model. Chemical Engineering Journal, *under review*.

As a result, the long dynamics of aqueous mineral carbonation reactors, in which the time scales of reactions and hydrodynamics vary widely, are obtained; hydrodynamics stabilizes in a few seconds, whereas the reaction reaches steady state after a few hours. The proposed method can replace the process of simulating several hours of reactions in CFD with millions of meshes with simulating just 10–15 sec in CFD until the hydrodynamics stabilizes, and then solve the fast kinetic DAEs for the rest. The model results were compared with the experimental results at industrial-scale plants to validate the model. Furthermore, the model was used to analyze the scaled-up reactors 2.5 and 10 times larger than an industrial-scale reactor.

2.2. Experimental setup

Experiments were performed at the industrial-scale plants whose configuration of the industrial-scale plant reactor is shown in Figure 2-1. The industrial-scale reactor is 4 m in diameter and 4 m in height. The spargers are complex with many 8-mm-diameter nozzles. Three 2-m-diameter pitched blade impellers were installed in the middle of the reactor. The impeller rotational speed was fixed at 30 rpm in all experiments.

The flue gas with flow rate of 5000–7000 Nm^3/h containing approximately 15 vol% of CO_2 flows into the first reactor containing a $Ca(OH)_2$ solution. The effluent gas from the first reactor enters the second reactor to capture the remaining CO_2 after pressurization. The $Ca(OH)_2$ solution is filled in both the reactors until the reactions are complete and product mixtures are drawn out. Two test operations were

performed under different conditions (see Table 2-1 for details). Experiment I-1 was performed for 1 day using only one reactor, whereas Experiment I-2 was performed using two reactors in series for 2 days. In Experiment I-2, the reactors were left undisturbed after the first day's operation was over. The second day's operation started with the same solutions and decreased temperatures in the reactors.

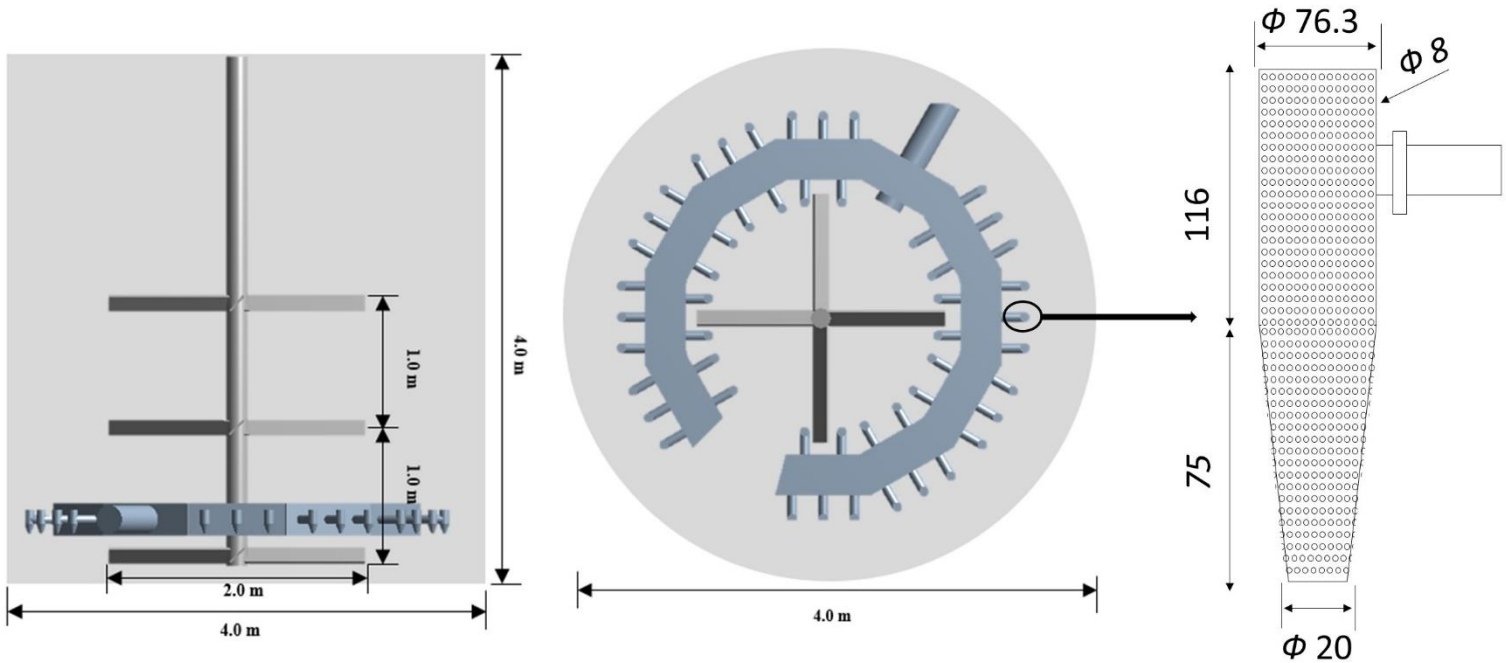

Figure 2-1. Side and top views of industrial-scale reactor and configuration of nozzle.

Table 2-1. Experimental conditions for industrial-scale process.

	Experiment I-1	Experiment I-2			
	Day 1	Day 1		Day 2	
Reactor	Single	1st	2nd	1st	2nd
Inlet flowrate (Nm^3/h)	6027	6748		6748	
CO_2 (vol%)	15.33	15.56		15.56	
Inlet gas temperature (°C)	47.44	54		52	
Initial solution height (m)	2.38	1.34	1.88	1.34	1.88
$Ca(OH)_2$ (initial wt%)	15	20	20		
Initial temperature (°C)	42	35	35	20	20

2.3. Mathematical models

2.3.1. Reactor model

Involved reactions

$$CO_2(g) \rightarrow CO_2(aq) \qquad \text{Eq. 2-1}$$

$$Ca(OH)_2(s) \underset{k_b}{\overset{k_f}{\rightleftharpoons}} Ca^{2+}(aq) + 2OH^-(aq) \qquad \text{Eq. 2-2}$$

$$CO_2(aq) + OH^-(aq) \underset{k_{12}}{\overset{k_{11}}{\rightleftharpoons}} HCO_3^-(aq) \qquad \text{Eq. 2-3}$$

$$HCO_3^-(aq) + OH^-(aq) \underset{k_{22}}{\overset{k_{21}}{\rightleftharpoons}} CO_3^{2-}(aq) + H_2O \qquad \text{Eq. 2-4}$$

$$H^+(aq) + OH^-(aq) \underset{k_{32}}{\overset{k_{31}}{\rightleftharpoons}} H_2O \qquad \text{Eq. 2-5}$$

$$CO_2(aq) + H_2O(l) \underset{k_{42}}{\overset{k_{41}}{\rightleftharpoons}} HCO_3^-(aq) + H^+(aq) \qquad \text{Eq. 2-6}$$

$$Ca^{2+}(aq) + {CO_3}^{2-}(aq) \underset{k_{52}}{\overset{k_{51}}{\rightleftharpoons}} CaCO_3(s) \qquad \text{Eq. 2-7}$$

$$Ca^{2+}(aq) + {HCO_3}^{-}(aq) \underset{k_{62}}{\overset{k_{61}}{\rightleftharpoons}} CaCO_3(s) + H^+(aq) \qquad \text{Eq. 2-8}$$

Mass balance equations

The reactors in this problem are significantly large to assume homogeneous distributions of reactants, particularly of the CO_2 gas. Therefore, the reactor volume is divided into several zones and set a mass balance equation for each zone with respect to CO_2(g). It is presumed that the concentrations of the solid and ions are the same in all zones because the solid and ion particles are small enough to make Stokes flow with circulating liquid streams.

The connections between zones are depicted in Figure 2-2. The exact mass balance equation at zone i can be written as

$$\frac{dm^i_{\mathrm{CO_2}(g)}}{dt} = \sum_{j\neq i}^{N} F_{j,i}\frac{m^j_{\mathrm{CO_2}(g)}}{m^j_{\mathrm{CO_2}(g)}(0)} - F_{i,i}\frac{m^i_{\mathrm{CO_2}(g)}}{m^i_{\mathrm{CO_2}(g)}(0)} - \dot{m}^i_{g\to l} \qquad \text{Eq. 2-9}$$

where $m^i_{\mathrm{CO_2}(g)}$ is the mass of CO_2 gas in zone i, $m^i_{\mathrm{CO_2}(g)}(0)$ is the initial value of $m^i_{\mathrm{CO_2}(g)}$, N is the total number of zones, $\dot{m}^i_{g\to l}$ is the CO_2 mass transfer rate from the gas phase to the liquid phase, and $F_{i,j}$ and $F_{i,i}$ are from the transition rate matrix defined as

$$\begin{bmatrix} F_{1,1} & F_{1,2} & \cdots & F_{1,N} \\ \vdots & \vdots & \ddots & \vdots \\ F_{N,1} & F_{N,2} & \cdots & F_{N,N} \\ F_{inlet,1} & F_{inlet,2} & \cdots & F_{inlet,N} \end{bmatrix}. \qquad \text{Eq. 2-10}$$

The transition rate matrix consists of $F_{i,j}$, which is the CO_2 mass flowrate from zone i to zone j. $F_{i,i}$ is the CO_2 mass outflow from zone i, and $F_{inlet,i}$ is the inlet mass flow rate from the sparger to zone i. All the components in the transition matrix besides $F_{i,i}$ (diagonal components) are imported from the CFD simulation. The

outflow, $F_{i,i}$, is not directly adopted from the CFD result; it is rather fixed as $F_{i,i} = -\sum_{j\neq i}^{N} F_{i,j}$ to ensure mass conservation at each zone because even a slight violation of the mass conservation can cause a convergence problem in subsequent steps.

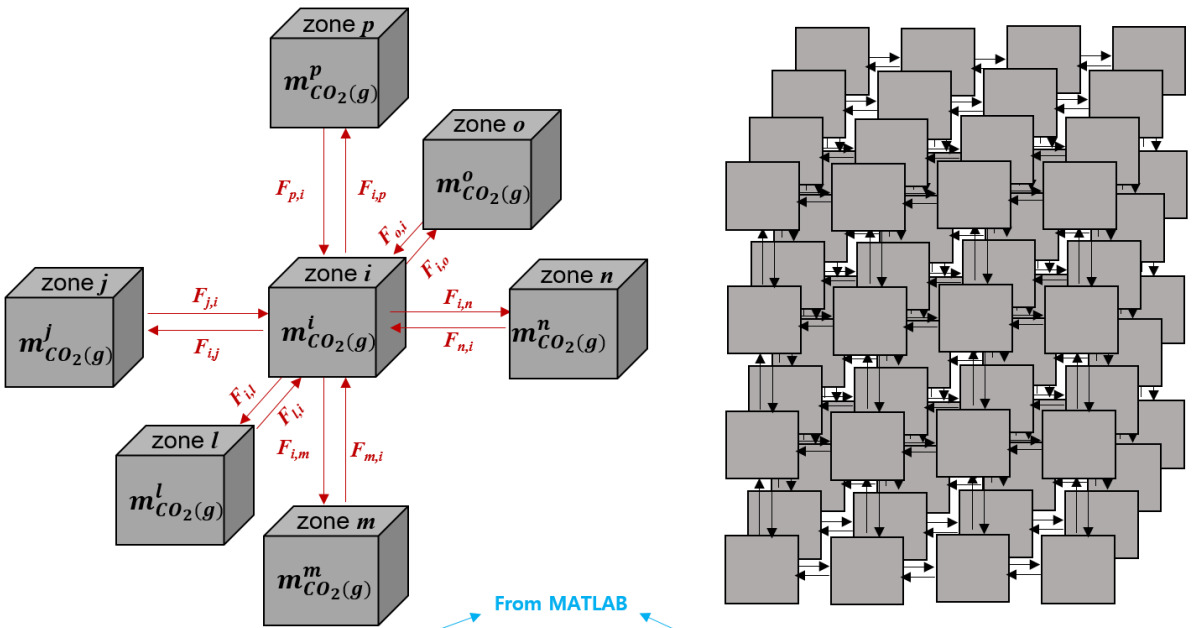

Figure 2-2. Systematic diagram for CFD-based compartmental model.

In Eq. 2-9, $F_{j,i}$ and $F_{i,i}$ are multiplied by $\frac{m^j_{\mathrm{CO_2}}}{m^j_{\mathrm{CO_2},initial}}$ and $\frac{m^i_{\mathrm{CO_2}}}{m^i_{\mathrm{CO_2},initial}}$, respectively. Because $F_{j,i}$obtained from CFD-hydrodynamics model does not include the reactions, it just provides the initial flow rates. Therefore, the CO_2 mass flow rate from j to i at time t, $F_{j,i}(t)$, was constrained to satisfy $F_{j,i}(t): F_{j,i}(0) = m^j_{\mathrm{CO_2}}(t): m^j_{\mathrm{CO_2},initial}$ to update the flowrates at every time step considering the proceeded reactions.

The CO_2 mass transfer rate, $\dot{m}^i_{g\to l}$, in Eq. 2- 9 is calculated as

$$\dot{m}^i_{g\to l} = k_L aE\left(H^{\mathrm{CO_2}}\frac{m^i_{\mathrm{CO_2}(g)}}{MW_{\mathrm{CO_2}}\cdot V^i_{gas}} - [\mathrm{CO_2}(aq)]\right)\cdot MW_{CO_2}, \qquad \text{Eq. 2-11}$$

where k_L is the overall CO_2 mass transfer coefficient, a is the interfacial area per unit volume, E is the enhancement factor to consider chemical mass transfer, $H^{\mathrm{CO_2}}$ is Henry's constant for the electrolyte solution, $MW_{\mathrm{CO_2}}$ is the molecular weight of CO_2, V^i_{gas} is the volume of gas at zone i obtained from CFD result, and $[\mathrm{CO_2(aq)}]$ is the molar concentration of $\mathrm{CO_2(aq)}$. The experimental or physical correlations are used for k_L, a, E, and $H^{\mathrm{CO_2}}$ found from the literature. Please refer to Section 3.3.1 for detailed equations. Some of these correlations include the Reynolds number. For its calculation, CFD results such as the average solution velocity u, w, v, and CO_2 velocity u, w, v in each zone are employed.

For the rest of the chemical species involved in the system, one mass balance equation per each one of them to represent the entire homogeneous reactor space is developed respectively. Because there are no inlet and outlet streams for the liquid

and solid, these equations do not include any flow rate terms.

$$\frac{d[\mathrm{CO_2(aq)}]}{dt} = -k_{11}[\mathrm{CO_2(aq)}][\mathrm{OH^-}] + k_{12}[\mathrm{HCO_3^-}] - k_{41}[\mathrm{CO_2(aq)}] + k_{42}[\mathrm{HCO_3^-}][\mathrm{H^+}] + \frac{1}{MW_{\mathrm{CO_2}} \cdot V_{liq}} \sum_{i=1}^{N} \dot{m}_{g\to l}^{i} \quad \text{Eq. 2-12}$$

$$\frac{\mathrm{d}[\mathrm{HCO_3^-}]}{dt} = k_{11}[\mathrm{CO_2(aq)}][\mathrm{OH^-}] - k_{12}[\mathrm{HCO_3^-}] - k_{21}[\mathrm{HCO_3^-}][\mathrm{OH^-}] + k_{22}[\mathrm{CO_3^{2-}}] + k_{41}[\mathrm{CO_2(aq)}] - k_{42}[\mathrm{HCO_3^-}][\mathrm{H^+}] - k_{61}[\mathrm{Ca^{2+}}][\mathrm{HCO_3^-}] + k_{62}[\mathrm{H^+}] \quad \text{Eq. 2-13}$$

$$\frac{\mathrm{d}\left[\mathrm{CO_3^{2-}}\right]}{dt} = k_{21}\left[\mathrm{HCO_3^-}\right]\left[\mathrm{OH^-}\right] - k_{22}\left[\mathrm{CO_3^{2-}}\right] - k_{51}\left[\mathrm{Ca^{2+}}\right]\left[\mathrm{CO_3^{2-}}\right] + k_{52} \quad \text{Eq. 2-14}$$

$$\frac{d[\mathrm{OH^-}]}{dt}$$

$$= -k_{11}\left[\mathrm{CO_2(aq)}\right][\mathrm{OH^-}] + k_{12}\left[\mathrm{HCO_3^-}\right]$$

$$- k_{21}\left[\mathrm{HCO_3^-}\right][\mathrm{OH^-}] + k_{22}\left[\mathrm{CO_3^{2-}}\right] \qquad \text{Eq. 2-15}$$

$$- k_{31}[\mathrm{OH^-}][\mathrm{H^+}]$$

$$+ 2A_s\left(k_f - k_b\left[\mathrm{Ca^{2+}}\right]f^2[\mathrm{OH^-}]^2 f^4\right)$$

$$\frac{\mathrm{d}[\mathrm{H^+}]}{dt}$$

$$= -k_{31}[\mathrm{OH^-}][\mathrm{H^+}] + k_{32} - k_{42}\left[\mathrm{HCO_3^-}\right][\mathrm{H^+}] \qquad \text{Eq. 2-16}$$

$$+ k_{41}\left[\mathrm{CO_2(aq)}\right] + k_{61}\left[\mathrm{Ca^{2+}}\right]\left[\mathrm{HCO_3^-}\right] - k_{62}[\mathrm{H^+}]$$

$$\frac{\mathrm{d}\left[\mathrm{Ca^{2+}}\right]}{dt}$$

$$= -k_{51}\left[\mathrm{Ca^{2+}}\right]\left[\mathrm{CO_3^{2-}}\right] + k_{52} - k_{61}\left[\mathrm{Ca^{2+}}\right]\left[\mathrm{HCO_3^-}\right] \qquad \text{Eq. 2-17}$$

$$+ k_{62}[\mathrm{H^+}] + A_s\left(k_f - k_b\left[\mathrm{Ca^{2+}}\right]f^2[\mathrm{OH^-}]^2 f^4\right)$$

$$\frac{\mathrm{d}\left[\mathrm{CaCO_3}\right]}{dt}$$

$$= k_{51}\left[\mathrm{Ca^{2+}}\right]\left[\mathrm{CO_3^{2-}}\right] - k_{52} + k_{61}\left[\mathrm{Ca^{2+}}\right]\left[\mathrm{HCO_3^-}\right] \qquad \text{Eq. 2-18}$$

$$- k_{62}[\mathrm{H^+}]$$

In Eq. 2-12, V_{liq} is the liquid volume of the reactor. In Eq. 2-15 and Eq. 2-17, A_s and f are the total surface area of $Ca(OH)_2$ and activity coefficient of the solution,

respectively. The term A_s is devised to decrease with the consumption of $Ca(OH)_2$. The correlations or values for all the rate constants are adopted from the literature (see Section 3.3.1).

Energy balance equation

It is very important to predict temperature accurately because several rate constants and terms in the mass transfer rate are functions of the temperature. Thus, a heat balance equation for the reactor was formulated as

$$\frac{\mathrm{d}T_{reactor}}{dt} = \frac{H_{in} - H_{out} - H_{water\ evaporation} + H_{reaction}}{C_{reactants}} \quad \text{Eq. 2-19}$$

$$H_{in} = \sum_{X=\mathrm{N_2},\mathrm{CO_2},\mathrm{H_2O}} n_{X,inlet} \cdot H_{m,X}\left(T_{inlet\ gas}\right), \quad \text{Eq. 2-20}$$

where $n_{X,inlet}$ and $H_{m,X}(T)$ denote the moles of X in the inlet stream and the molar enthalpy of X at temperature T, respectively.

$$H_{out} = \sum_{X=\mathrm{N_2},\mathrm{CO_2},\mathrm{H_2O}} n_{X,outlet} \cdot H_{m,X}(T_{reactor}), \quad \text{Eq. 2-21}$$

$$H_{water\ evaporation} = \left(n_{\mathrm{H_2O},outlet} - n_{\mathrm{H_2O},inlet}\right) \cdot \Delta H_{m,water\ evaporation} \quad \text{Eq. 2-22}$$

where $\Delta H_{m,water\ evaporation}$, the molar latent heat of water is 40660 J/mol.

$$H_{reaction} = \Delta H_{m,reaction} \cdot \frac{d[\mathrm{CaCO_3}]}{dt} \cdot V_{liq}, \qquad \text{Eq. 2-23}$$

where $\Delta H_{m,reaction}$, the heat of the net reaction, $\mathrm{CO_2 + Ca(OH)_2 \rightarrow CaCO_3 + H_2O}$, is 113.1 kJ/mol.

$$C_{\text{reactants}} = m_{\mathrm{H_2O}} \cdot c_{\mathrm{H_2O}} + m_{\mathrm{Ca(OH)_2}} \cdot c_{\mathrm{Ca(OH)_2}} + m_{\mathrm{CaCO3}} \cdot c_{\mathrm{CaCO_3}}, \qquad \text{Eq. 2-24}$$

is the heat capacity of all the reactants. To calculate $C_{\text{reactants}}$,

$$m_{\mathrm{H_2O}} = \frac{V_{\text{liq}}}{\rho_{\mathrm{H_2O}}}, \qquad \text{Eq. 2-25}$$

$$m_{\mathrm{Ca(OH)_2}} = m_{\mathrm{Ca(OH)_2,initial}} - ([\mathrm{Ca^{2+}}] + [\mathrm{CaCO_3}]) \cdot V_{liq} \cdot MW_{\mathrm{Ca(OH)_2}}, \qquad \text{Eq. 2-26}$$

$$m_{\mathrm{CaCO_3}} = V_{liq}[\mathrm{CaCO_3}] \qquad \text{Eq. 2-27}$$

are applied. For heat capacities, $c_{\mathrm{H_2O}}$ is 4.18 J/g·K, $c_{\mathrm{CaCO_3}}$ is 0.8343 J/g·K, a correlation (see Supporting Material of Na et al. [77]) is adopted for $c_{\mathrm{Ca(OH)_2}}$. When calculating H_{in} and H_{out}, $n_{N_2,inlet}$ and $n_{\mathrm{CO_2},inlet}$ are determined from the experimental setup. On the other hand, $n_{\mathrm{N_2},outlet} = n_{\mathrm{N_2},inlet}$ and $n_{\mathrm{CO_2},outlet} = n_{\mathrm{CO_2},inlet} - \frac{1}{MW_{\mathrm{CO_2}} \cdot V_{liq}} \sum_{i=1}^{N} \dot{m}_{g\rightarrow l}^{i}$, which means that CO_2 not transferred to the solution goes to the outlet stream. The quantities of water in the inlet and outlet streams are determined according to the maximum moisture content allowed for air at a given temperature, $\theta_{w,max}(T)$:

$$n_{\mathrm{H_2O}} = \left(n_{\mathrm{N_2}} + n_{\mathrm{CO_2}}\right) \cdot \theta_{w,max}(T) \qquad \text{Eq. 2-28}$$

For $H_{m,X}(T)$ and $\theta_{w,max}(T)$, regressed equations from the data table of the ideal gas properties are used (see Supporting Material [77]) for details).

2.3.2. CFD model

The flowrates between the zones are brought from CFD simulation results. Here, the CFD modeling methods for the mineral carbonation reactors are described.

Among the three phases involved in the system, only gas and liquid flows are modeled using Eulerian-Eulerian approach. The solid particles in the system is too small to affect the flow of other phases, so only the change of viscosity and density of the primary liquid phase are reflected. (see Kim et. al [5] for details.)

Mass and momentum conservation equations are given as

$$\frac{\partial\left(\alpha_{\mathrm{k}}\rho_k\right)}{\partial t} + \nabla \cdot (\alpha_k \rho_k \boldsymbol{u}_k) = 0 \qquad \text{Eq. 2-29}$$

$$\frac{\partial\left(\alpha_{\mathrm{k}}\rho_k \boldsymbol{u}_k\right)}{\partial t} + \nabla \cdot (\alpha_k \rho_k \boldsymbol{u}_k \boldsymbol{u}_k) = \nabla \cdot (\alpha_k \mu_{eff}(\nabla \boldsymbol{u}_k + (\nabla \boldsymbol{u}_k)^T)) - \alpha_k \nabla p_k + \boldsymbol{M}_k \qquad \text{Eq. 2-30}$$

where ρ, $\boldsymbol{u}$, μ_{eff}, and p are volume fraction, density, velocity, effective viscosity, and pressure, respectively, and the subscript k denotes the phase type (solution phase: m, gas phase: g). Interphase momentum exchange term between the k-phase and all other phases is given as $\boldsymbol{M}_k$.

$$\boldsymbol{M}_m = -\boldsymbol{M}_g = \boldsymbol{M}_{m,D} + \boldsymbol{M}_{m,L} + \boldsymbol{M}_{m,VM}, \qquad \text{Eq. 2-31}$$

$$\boldsymbol{M}_{m,D} = \frac{3}{4}\alpha_g \rho_m \frac{C_D}{d_B}\left|\boldsymbol{u}_g - \boldsymbol{u}_m\right|\left(\mathbf{u}_{\mathrm{g}} - \boldsymbol{u}_m\right), \quad \text{Eq. 2-32}$$

$$\boldsymbol{M}_{m,L} = \alpha_g \rho_m C_L\left(\boldsymbol{u}_g - \boldsymbol{u}_m\right) \times \nabla \times \boldsymbol{u}_m, \quad \text{Eq. 2-33}$$

$$\boldsymbol{M}_{m,VM} = \alpha_g \rho_m C_{VM}\left(\frac{D_g \boldsymbol{u}_g}{Dt} - \frac{D_m \boldsymbol{u}_m}{Dt}\right) \quad \text{Eq. 2-34}$$

where $\boldsymbol{M}_{m,D}$, $\boldsymbol{M}_{m,L}$, and $\boldsymbol{M}_{m,VM}$ denote drag, lift, and virtual mass force, respectively. The drag coefficient (C_D), lift coefficient (C_L), and virtual mass force coefficient (C_{VM}) were set as 0.44, 0.5, and 0.25 when α_g is less than 0.45; and 0.05, 0, and 0, otherwise. This is to prevent a high value of α_g causing numerical problems [79, 80].

For the turbulence flow modeling, a standard *k*-ε modeling approach as well as the effective viscosity term in Eq. 2-30 are introduced.

$$\begin{aligned} &\frac{\partial}{\partial t}(\rho_m \alpha_m k_m) + \nabla \\ &\cdot\left(\alpha_m(\rho_m \boldsymbol{u}_m k_m - \left(\mu_m + \frac{\mu_{t,m}}{\sigma_k}\right)\nabla k_m\right) \\ &= \alpha_m(P_m - \rho_m \epsilon_m), \end{aligned} \quad \text{Eq. 2-35}$$

$$\begin{aligned} &\frac{\partial}{\partial t}(\rho_m \alpha_m \epsilon_m) + \nabla \\ &\cdot\left(\alpha_m \rho_m \boldsymbol{u}_m \epsilon_m - \left(\mu_m + \frac{\mu_{t,m}}{\sigma_\epsilon}\right)\nabla \epsilon_m\right) \\ &= \alpha_m \frac{\epsilon_m}{k_m}(C_{1\epsilon} P_m - C_{2\epsilon} \rho_m \epsilon_m), \end{aligned} \quad \text{Eq. 2-36}$$

where the parameters C_μ, $C_{1\epsilon}$, $C_{2\epsilon}$, σ_k, and σ_ϵ have values of 0.09, 1.44, 1.92, 1.0, and 1.3, respectively, and P_m represents the turbulence production owing to buoyancy and viscous forces which is calculated as

$$P_m = \mu_{t,m}\nabla \boldsymbol{u}_m \cdot (\nabla \boldsymbol{u}_m + \nabla \boldsymbol{u}_m^T) - \frac{2}{3}\cdot \nabla \boldsymbol{u}_m (3\mu_{t,m}\nabla \cdot \boldsymbol{u}_m + \rho_m k_m) \quad \text{Eq. 2-37}$$

The effective viscosity is expressed as

$$\mu_{eff} = \mu_m + \mu_{t,m} \quad \text{Eq. 2-38}$$

where μ_m is the original solution viscosity and $\mu_{t,m}$ is turbulence viscosity defined as

$$\mu_{t,m} = \rho_m C_\mu \frac{k_m^2}{\epsilon_m}. \quad \text{Eq. 2-39}$$

2.3.3. Numerical setting

A commercial software ANSYS CFD 18.2 (Ansys., USA) is used on Intel Xeon E5-2690 (24 cores) machine with 128 GB RAM for all CFD simulations.

For the walls in the reactor, free-slip and no-slip conditions were adopted for the gas and solution phases, respectively. For the gas outlet, the de-gassing condition, which only allows the discharge of gas, was used. To prevent the computational time increase caused by excessively fine meshes around the gas sparger, the detailed configuration of nozzle holes are omitted. The rotation of the impellers are simulated using a multiple reference frame (MRF) method. For the advection and transient schemes, a high resolution and second-order backward Euler were used, respectively. The convergence is achieved when the residual drops to $1.0e^{-4}$. A time step of 0.01s is applied.

While obtaining the CO_2 mass transfer rates from the CFD-based compartmental model, the regions above the aqueous solution were not considered. In other words, it was assumed that the CO_2 mass transfer only takes place in the region where the gas is distributed in the form of particles throughout the liquid phase. In the CFD-based compartmental model, the zones near the liquid surface contain both the regions which does and does not satisfy the above statement. This necessarily happens because the angled shape compartments cannot accurately separate the curved surface of the liquid. The solution for this problem is to divide the reactor into a number of angled zones first, and then reset the zones located near the surface in the CFD simulation to only include the meshes with gas holdup less than 0.8.

For the kinetic model, MATLAB with Sundials IDAS solver was used. Particularly, dense linear solver with the relative tolerance 10^{-7} and zero-crossing root algorithm were employed.

2.4. Results and discussions

2.4.1. CFD-based compartmental model for industrial-scale reactor.

The CFD-based compartmental model with the full kinetics was implemented to simulate the industrial-scale reactor. The number of zones in the model was set to 179 because 119-zone model showed significantly different results while the 291-zone model showed little difference as shown in Figure 2-3. The detailed configuration of the 179 compartments is shown in Figure 2-4.

Two sets of data from the test operations performed at the Incheon plant were obtained. The data include time series measurements of the overall CO_2 removal efficiency and *p*H and temperature values of each reactor. Figure 2-5 shows the model prediction performance from the initial states until all $Ca(OH)_2$ is consumed.

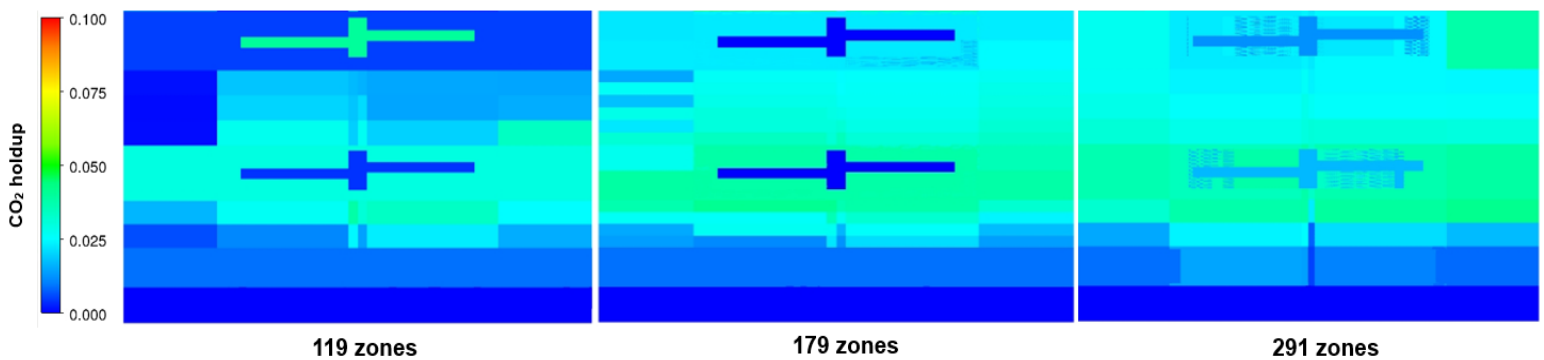

Figure 2-3. CO_2 holdup profiles of the CFD-based compartmental model in 119-zone (left), 179-zone (middle), and 291-zone (right) models in Experiment I-1 2nd reactor.

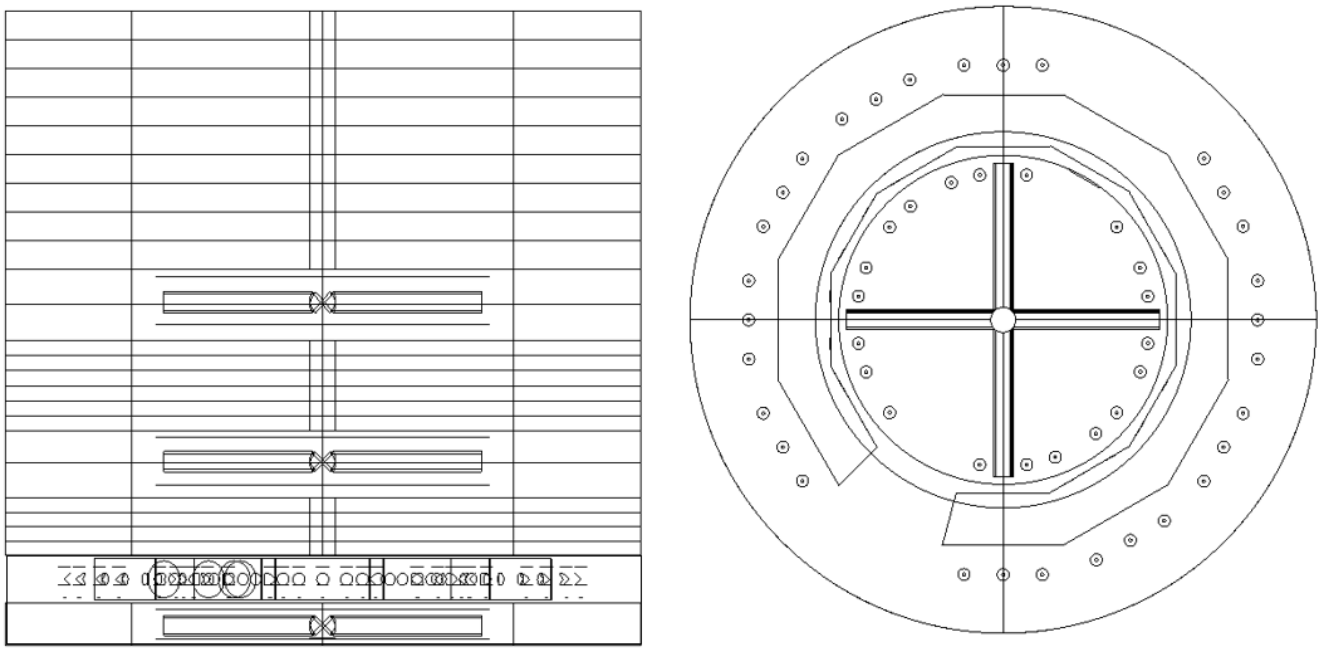

Figure 2-4. Side and top view of the 179-zone model in the industrial-scale reactor.

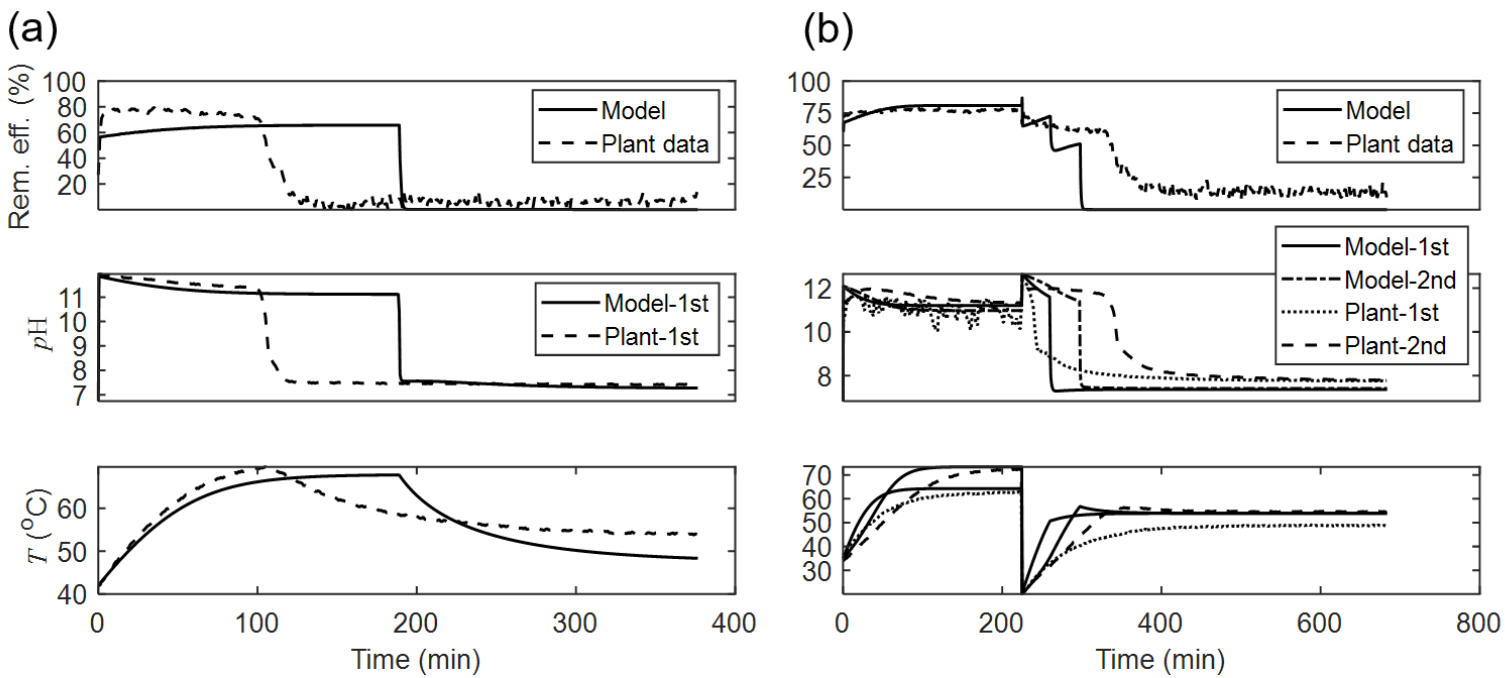

Figure 2-5. Model results compared with operation data from (a) Experiment I-1 and (b) Experiment I-2.

One cycle of batch process starts with reactors fully charged with $Ca(OH)_2$ to keep a high level of *p*H until the majority of $Ca(OH)_2$ is reacted. Because the net reaction is exothermic and the inlet gas temperature (usually around 50 °C) is higher than the initial reactor temperature, the temperatures increases as reactions proceed. When most of $Ca(OH)_2$ disappears, the *p*H and removal efficiency start to decrease. In Experiment I-2, the solution volume in the 1st reactor is only two third that of the 2nd reactor, which explains the faster termination of the 1st reactor operation. However, even if the reactors had the same volume of reactants, the reactions would end earlier in the 1st reactor because the concentration of CO_2 in the inlet stream is significantly higher and so is the driving force and rate of the interphase mass transfer. The temperatures do not increase linearly but saturate at some point because the higher the temperature, the more the water evaporated; consequently, more heat is lost as latent heat. Before the reactions end, the thermodynamic equilibrium is reached when the enthalpy of the inlet stream becomes equivalent to the sum of enthalpies of the outlet stream, heat of reaction, and latent heat from water evaporation. The temperatures start to decrease when the reactions are complete but saturate after a while again. In the model, it happens when the reactor temperature reach the inlet gas temperature.

Some mismatches between the model and the real process behaviors exist; however, most of these mismatches can be explained. First, there is difference in the times when the CO_2 removal efficiency and *p*H sharply decline, particularly in Experiment I-1. Because the decline starts when the base source, $Ca(OH)_2$, is completely consumed, initial amounts of $Ca(OH)_2$ in each reactor determine the starting time

point of the decrease. In the model, the initial amount of $Ca(OH)_2$ is calculated based on the measured height and concentration of the solution. Therefore, the errors in their measurement would easily result in a discrepancy in the disappearing moment of $Ca(OH)_2$. Second, the model does not behave as smooth around inflection points as the real plant. For example, the removal efficiency of the plant data (top graph of Figure 2-5 (a)) shows a gradually decreasing behavior whereas the model result has a sharp breaking point. In Figure 2-5 (b), the plant data also look like an averaged curve of the model results where the steps are observed. In the model, the dissolution of $Ca(OH)_2$ follows the same kinetics described in Eq 2-15 and Eq. 2-17 till the end. However, the real process may involve different reaction mechanisms when not much $Ca(OH)_2$ is left and the dissolution rate drops. One possible explanation is the precipitation of $CaCO_3$ on the $Ca(OH)_2$ surface [81]. $CaCO_3$ forms the shell of the particles and hinders the dissolution of $Ca(OH)_2$. However, CO_2 can diffuse through the shell and react with $Ca(OH)_2$ in the core part. This also explains the phenomenon in which a low level of the removal efficiency is still maintained after a significant drop in *p*H. Furthermore, the temperature changes are slightly different. It is because the model simplifies the complex thermodynamic behaviors of the involved materials; it is assumed that all the gas species follow the ideal gas law and binary interactions are ignored in enthalpy and density calculations. The water content of the gas stream was also forced to reach the 100% humidity of the temperature provided that the inlet gas from the flue gas is containing enough amount of water vapor after combustion and the outlet gas is from the reactor full of aqueous solution. However, as real gas behaves differently from the ideal gas, the total enthalpy of the inlet and outlet streams

in the model could be different from the real values. Nonetheless, the overall tendency and maximum temperature, which is important because it significantly influences the removal efficiency, matches the plant data. In Experiments I-1 and I-2, the removal efficiency shows around 7 % and 5% errors based on the steady state, respectively. At the same time, the maximum temperature in Experiment I-1 shows a discrepancy of 2.7% and Experiment I-2 has 2.1% and 1.2 % errors for the 1st and 2nd reactors, respectively.

The model is limited in predicting the termination of the batch cycle, but it predicts the beginning and the steady-state stages with significant accuracy. It shows that it is able to estimate the maximum removal efficiency and temperature of the reactor from only its design and the initial operating conditions. It is also able to monitor the changes in the concentration of each species as well as the accumulation of the product during the operation using the model. Figure 2-6 shows that the amount of remaining $Ca(OH)_2$ decreases, whereas the concentration of Ca^{2+} ions is still maintained at a certain level. It shows that the rate determining step of this process is not the dissolution of $Ca(OH)_2$ but the dissolution of the CO_2 gas. It is also supported by the negligible concentration of $CO_2(aq)$, HCO_3^-, CO_3^{2-} ions at the same time.

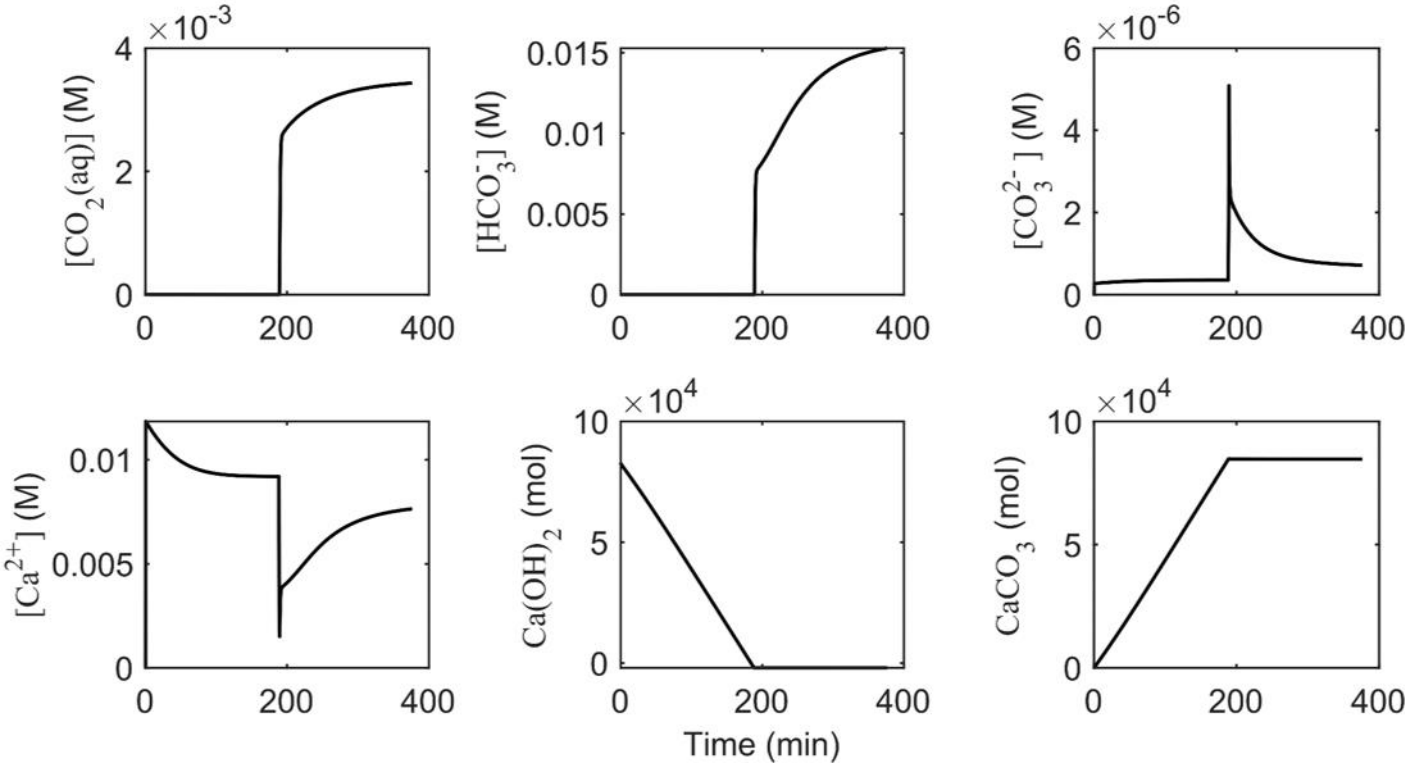

Figure 2-6. Concentration changes of involved species during Experiment I-1.

The concentration of CO_2 gas is different at each zone. Figure 2-7 shows that CO_2 volume fractions are generally low during the active period, in which the removal of CO_2 occurs. In addition, the CO_2 gas occupies less fraction of volume as it rises to the top, which means that CO_2 in the flue gas is gradually absorbed during the residence time. However, the simulation shows that the zones close to impellers do not have the CO_2 gas. This is because the MRF region that used to simulate rotating impellers in CFD cannot be divided into multiple zones in the compartmental model. The MRF zones have negligible inflow from the adjacent zones owing to the propelling power of impellers. However, reactions occur actively during the initial period. Therefore, the CO_2 holdup converges to 0 in a short time until the reactions are completed. If it was possible to divide the MRF zones in the angular direction, the inflow from the side zone would exist at a significant level and the CO_2 holdup would not drop to 0.

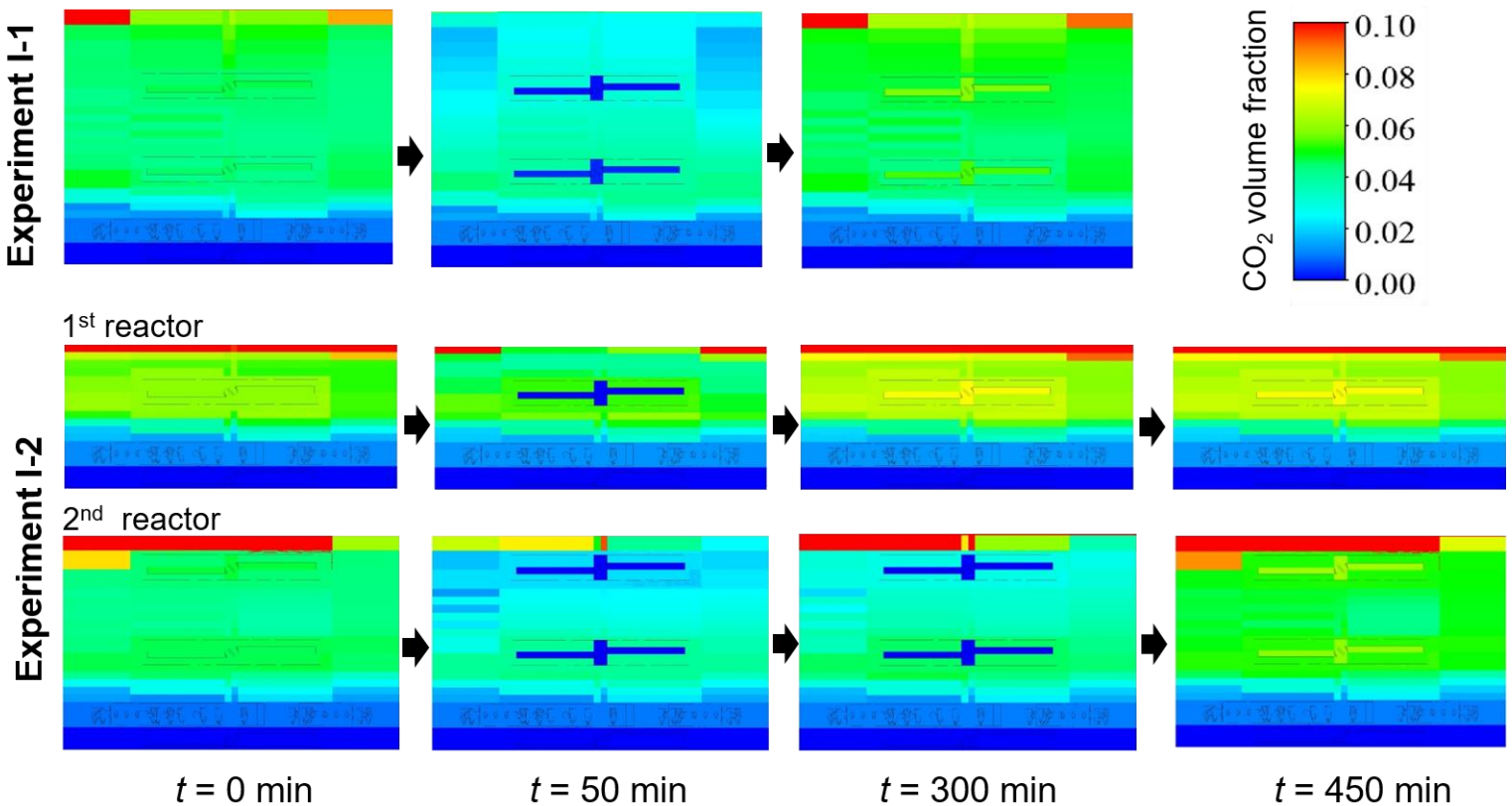

Figure 2-7. CO_2 volume fraction changes at each zone during the operation.

2.4.2. Design and simulation of higher-scale reactors

The CFD-based compartmental model can help in designing reactors of different sizes and for different purposes. The developed model was used to predict the CO_2 removal efficiency of larger reactor designs to scale up the mineral carbonation process. Here, two reactor designs of different sizes to handle 2.5 (Type A) and 10 times (Type B) more flue gas than the industrial-scale one are proposed. Proposed designs are not merely the scaled up versions of the current design; the internal structures are modified to improve the performance of the proposed reactors. The configurations of the two reactors are given in Figure 2-8.

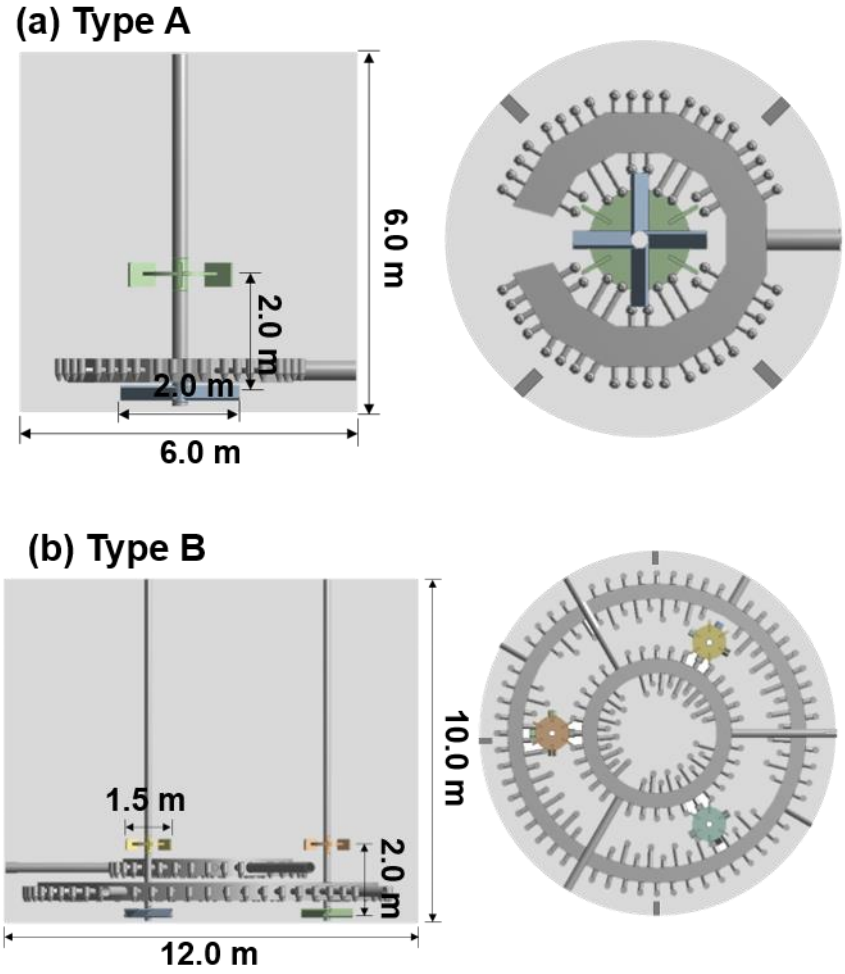

Figure 2-8. Side and top views of Type A (gas inlet 17,500 Nm^3/hr) and Type B (gas inlet 70,000 Nm^3/hr) reactors.

Because the *p*H and temperature of the reactor are not controlled under the current mode of operation, dynamic simulations should be conducted from the possible initial conditions to predict the CO_2 removal efficiency at the steady state. Note that it is already shown that the CFD-based compartmental model can predict the steady-state performances with good accuracies. The number of zones applied to Type A and Type B reactors are 181 and 164, respectively. The configurations are given in Figure 2-9. The inlet volumetric flow rates are 17,500 Nm^3/hr and 70,000 Nm^3/hr and the initial liquid heights are 4 m and 6 m for Type A and Type B, respectively. In both reactors, the volume fraction of CO2 in the inlet flue gas, the weight fraction of Ca(OH)2 in the liquid reactant, and the initial temperature of the reactant are set to 15%, 20% and 20 °C, respectively. The predicted dynamic behaviors are shown in Figure 2-10.

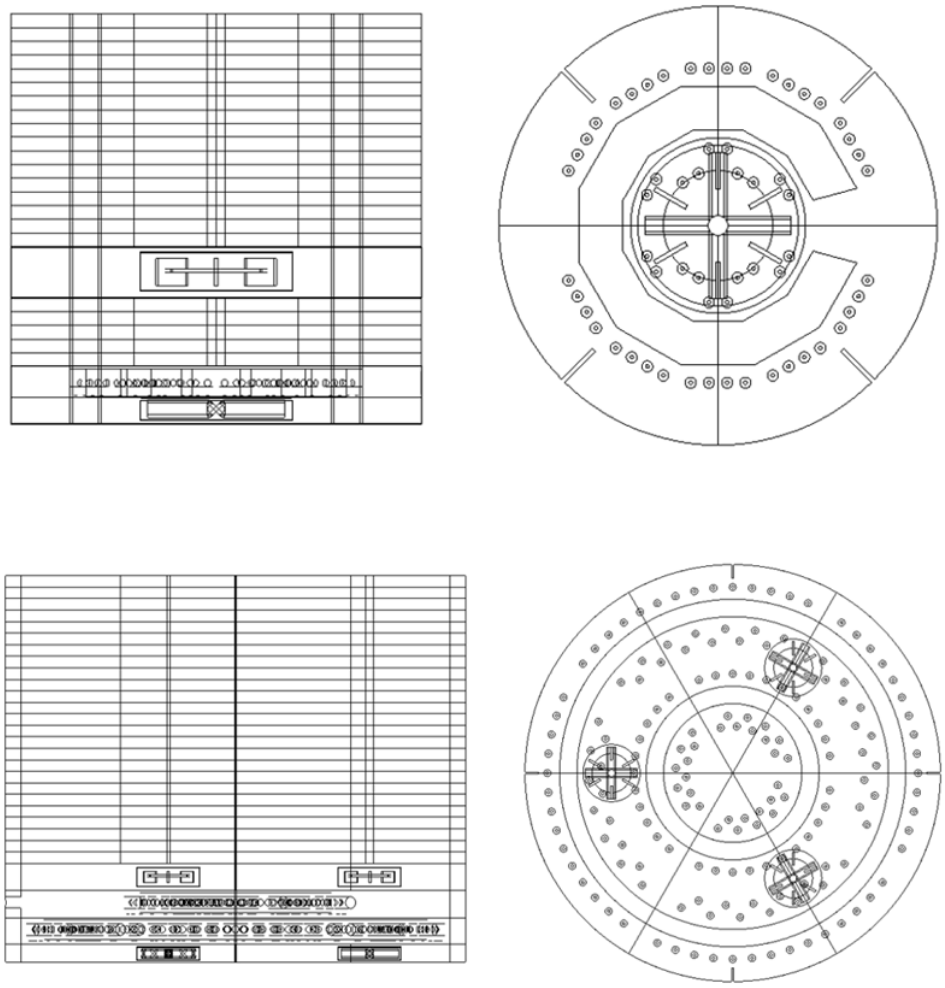

Figure 2-9. Top) Side and top view of the 181 compartments for Type A reactor, Bottom) Side and top view of the 164 compartments for Type B reactor.

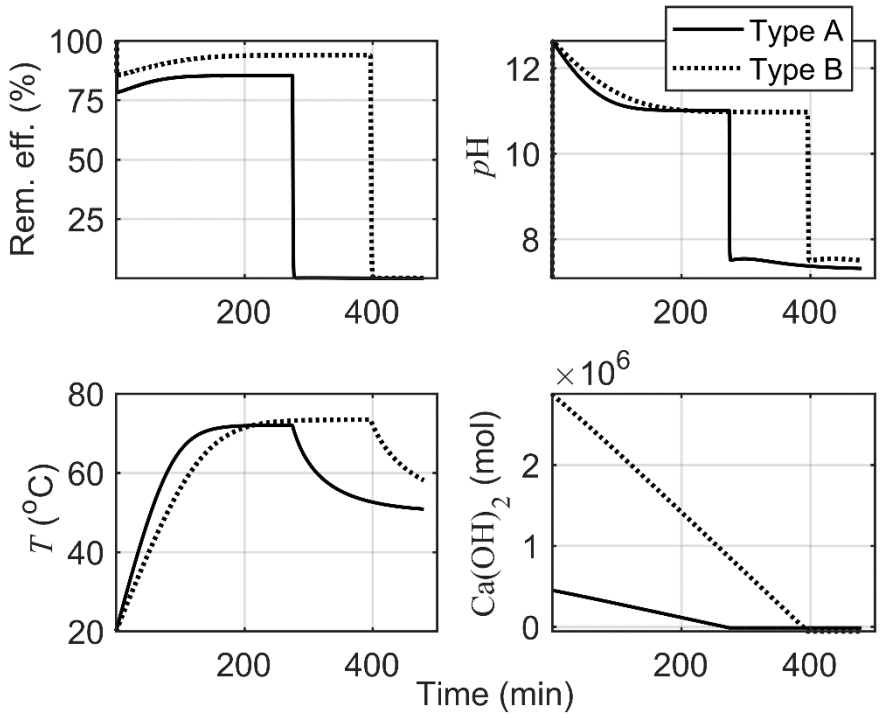

Figure 2-10. Predicted dynamic behaviors of Type A and Type B reactors.

The CO_2 removal efficiencies were derived only from one reactor for each type unlike the pilot- and industrial-scale plants in which two connected reactors were present and the CO_2 removal efficiencies were calculated from the sum of mass-transferred CO_2 in two reactors in series. The CO_2 removal efficiencies were 85.3% for Type A and 93.9 % for Type B with single reactor. The reason for the higher CO_2 removal efficiencies is the initial solution height. Owing to the greater solution height, the CO_2 residence time increased, and this led the high removal efficiencies.

2.5. Conclusions

CFD-based compartmental model is a great tool to implement the long-time dynamic simulations of industrial multiphase reactors. This chapter describes the modeling method as well as the validation results with pilot plant data.

Industrial-scale reactor built in Incheon, South Korea are modeled using CFD-based compartmental modeling method. The entire reactor space is divided into 179 zones, in which homogeneous distributions of gas are assumed. 179 mass balance equations for CO_2 gas including the reactions are set for each zone. In- and out- flow rates for each zone are brought from the CFD simulation results. For the mass balance equations of other aqueous species and heat balance equation, zoning method is not used; one equation is set for entire reactor. The formulated equations are in differential algebraic equations form and solved using Sundials IDAS solver.

The dynamic simulation was performed from the initial conditions based on the experiments at the industrial-scale plant. The model could predicted the CO_2 removal

efficiency, *p*H, and temperature changes over the batch operations of 5–10 h with good accuracy. Although the model failed at catching the termination moments, it was able to predict the maximum efficiency and the temperature of the given conditions very well. Furthermore, the model is capable of observing the hidden dynamics such as concentration changes in every chemical species, which was not possible to measure in real plants.

The CFD-based compartmental model was also used to predict the dynamic behavior of reactors larger scale reactors. Any type of multiphase industrial-scale reactors can be simulated using CFD-based compartment model as long as CFD and kinetic models of the system are available. It allows to simulate long-time dynamic behavior of the transient system as well as the effect of non-homogeneous mixing in industrial processes.

Suggestions on zone dividing method

The most critical parameter which influences the reactor performance must be identified when dividing the reactor into many zones. The identified parameter is recommended to be homogenous in each zone. In momentum transport dominant reactors, parameters related to mixing are critical. Mixing scales can subsequently categorized into micro-, meso- and macro- levels. Micromixing refers to the Kolmogorov scales of motion and it becomes critical in reactors with very fast reactions. Kolmogorov time scale is calculated as $\left(\frac{\nu}{\epsilon}\right)^{0.5}$, where ν is the kinematic viscosity of the fluid and ϵ is the average dissipation rate of turbulence kinetic energy. Mesomixing indicates the turbulent dispersion of a feed inlet stream and it largely

influences the performance of semi-batch reactors. Mesomixing time for dispersion of feed is expressed as $\frac{Q}{U(0.1k^2\epsilon)}$ [82], where Q is the volumetric inlet flowrate, U is the surrounding fluid velocity near inlet, and k is the turbulence kinetic energy. Macromixing is related to bulk motion of fluid and, for example, affects blend time in batch systems. Average energy dissipation could be a good indicator in such cases.

In mass transport dominant reactors, for example, in multiphase reactors where interphase reactions or heterogeneous catalytic reactions take place, different factors are recommended to use as a zone dividing criterion. For example, in the mineral carbonation reactor, the mass transport of CO_2 from gas to aqueous phase is the dominant phenomenon. Thus, the maintaining the homogenous gas holdup and interfacial area in each zone was the primary consideration in this thesis. In some reactors, the solid holdup could be the key parameter, and in other reactors where the mass transport is mostly affected by the temperature, the temperature gradient must be the main concern. However, the zone dividing with only one criterion (gas holdup in the current case) could ignore the effect of other factors; a potential pH gradient in the reactor was ignored in the proposed CFD-based compartment model which could bring partial contribution on model-plant mismatch.

Chapter 3.

Model intensification of aqueous mineral carbonation kinetics via Bayesian calibration*

3.1. Objective

Here, fundamental aqueous mineral carbonation kinetics model for three-phase (solid: $Ca(OH)_2$, NaOH, and $CaCO_3$}; liquid: absorbent solution with ions; gas: flue gas) reactor. The model takes a form of differential algebraic equations (DAEs). Using an existing DAE solver [83], it was able to solve the stiff and hybrid systems with significant magnitude differences among the parameters and discrete events such as the disappearance of solids after complete dissolutions. The parameters in the model are estimated through a Bayesian parameter estimation framework, which can quantify uncertainties in the experimental outputs. In order to show the efficacy of the developed framework and obtain the posterior distributions of mineral carbonation kinetic parameters, a lab-scale process is constructed and experiments according to an orthogonal array design of experiments (DoE) are conducted.

* This chapter cites the author's published journal article: Na, J., Park, S., Bak, J., Kim, M., Lee, D., Yoo, Y., Kim, I., Park, J., Lee, U., & Lee, J. (2019). Bayesian inference of aqueous mineral carbonation kinetics for carbon capture and utilization. Industrial & Engineering Chemistry Research, 58(19), 8246-8259.

This chapter is organized as follows. First, the experimental methods of lab-scale mineral carbonation process are presented. Then, the mathematical model of reaction kinetics for 3-phase mineral carbonation reactor is described. A Bayesian parameter estimation scheme is explained in the next section. In 3.5. physical interpretation of the experimental results and the parameter estimation. Finally, concluding remarks are provided.

3.2. Experimental methods

3.2.1. Solution and gas preparation

The absorbent solution was a mixture of $Ca(OH)_2$ (purity $>$ 95.0% $Ca(OH)_2$ ACS reaction, Sigma Aldrich) and NaOH (purity $>$ 97.0% NaOH ACS reaction, Sigma Aldrich) in distilled water. CO_2 and N_2 gas mixture was used as an artificial flue gas. The CO_2 volume concentration of inlet flue gas, ϕ_{CO2}^{inlet}, and the flue gas flow rate, $\dot{V}$ were controlled by mass flow controller (MFC) at 101.325 kPa. The reactor temperature, T, the weight fractions of $Ca(OH)_2$ ($w_{Ca(OH)2}$) and NaOH (w_{NaOH}), ϕ_{CO2}^{inlet}, and $\dot{V}$ were decided by an orthogonal array experiment design method (a strength 2, 4 levels, 5 factors and index 1; 2-(4,5,1)). 16 experiments were conducted according to the experiment design and one additional experiment for validation, as described in Table 1.

Table 3-1. 2-(4,5,1) orthogonal array experiment design

Exp. #	T (˚C)	ϕ_{CO2}^{inlet} (vol%)	$w_{Ca(OH)2}$ (wt%)	w_{NaOH} (wt%)	$\dot{V}$ (L/min)
1	25	2	1	0	0.5
2	25	10	1.5	1	1
3	25	20	2	2	1.5
4	25	30	3	3	2
5	40	2	1.5	2	2
6	40	10	1	3	1.5
7	40	20	3	0	1
8	40	30	2	1	0.5
9	50	2	2	3	1
10	50	10	3	2	0.5
11	50	20	1	1	2
12	50	30	1.5	0	1.5
13	68	2	3	1	1.5
14	68	10	2	0	2
15	68	20	1.5	3	0.5
16	68	30	1	2	1
Test	70	10	3	1	2

3.2.2. Laboratory-scale mineral carbonation process

The overall schematic process flow diagram is shown in Figure 1. 500 ml PYREX double-jacketed reactor was used as a gas mixer and a carbonation reactor. To filtrate the solid particles including calcium carbonate, calcium hydroxide, and sodium hydroxide, glass fiber filter with 1.6 pore was applied at the inlet blower of CO_2 gas. The temperature of the gas mixer and the carbonation reactor, T, were controlled by a thermostat water bath. To prevent concentration changes caused by evaporation of the absorbent solution, a condenser was installed with a water chiller. Experiment outputs were CO_2 volume concentration of the outlet flue gas, ϕ_{CO2}^{outlet}, and pH of the absorbent solution in the reactor. They were recorded from the gas analyzer (multi-gas analyzer, Sensoronic) and the pH meter (HM-41X, DKK-TOA) in time-series (sampling time was 30 seconds), respectively.

To start-up the process, temperatures of water baths of the gas mixer and the reactor were first set following the experiment design. In order to get perfectly mixed flue gas as well as to prevent fluctuations of the concentration and the temperature, the CO_2 gas was sent to a vent line for a while until the temperature reached a steady-state. Meanwhile, highly pure N_2 gas was purged to the reactor to remove the latent dissolved air and impurities. Afterwards, the N_2 purging was stopped and the reactor was filled with 500 of the absorbent solution. Lastly, the valve prior to the reactor was opended so the flue gas could be blown into the reactor. The reacting mixture was stirred in 300 rpm using a magnetic bar to distribute bubbles and solid particles. The experimental outputs were recorded every half a minute. When the CO_2 volume

concentration of the outlet flue gas showed no difference to the inlet gas, which means that the absorbent solution cannot absorb CO_2 gas any longer, it was assumed that the absorbents in the solution were entirely consumed. So the data logging was stopped and the process was shut down. Similar experimental settings and procedure were applied in the previous papers as well [84, 85].

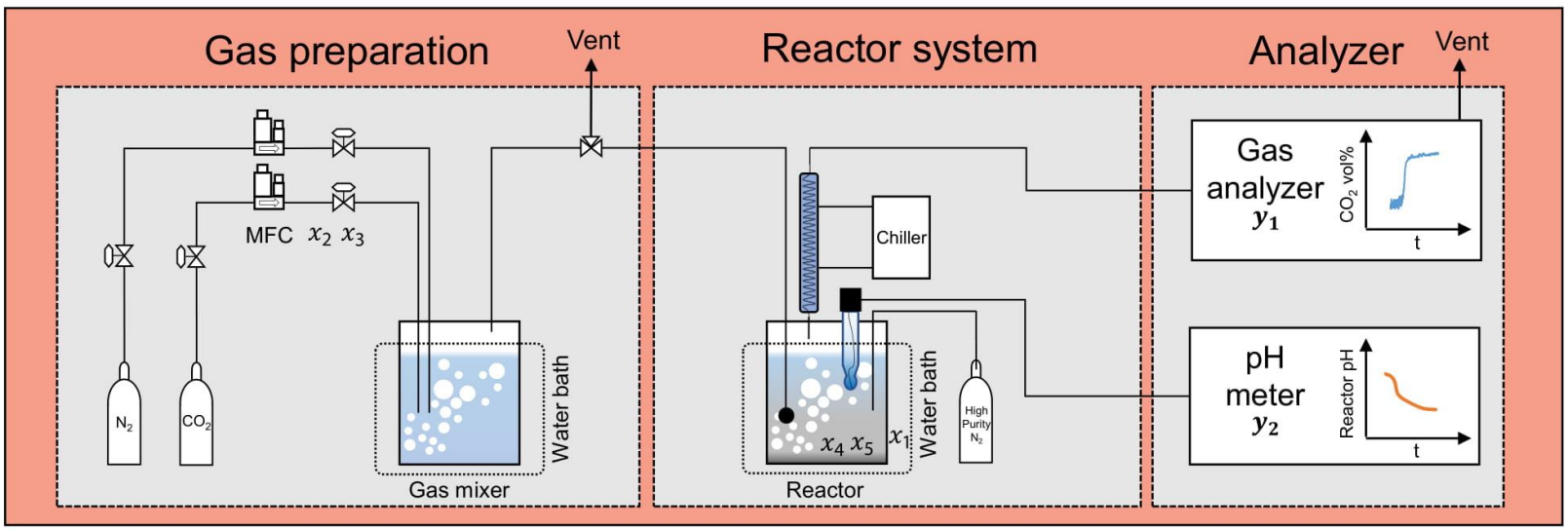

Figure 3-1. Schematic process flow diagram of aqueous mineral carbonation process for CO2 absorption and utilization.

3.3. Mathematical models

The reactions involved in the aqueous mineral carbonation process can be categorized into four groups: First, mass transfer of carbon dioxide gas into the water solution, which is the most important reaction that decides the overall CO_2 removal efficiency. Second, dissolutions of two solid species, NaOH and $Ca(OH)_2$. Third, ionic reactions between the dissolved ions derived from the gas and solid reactants. Last, the precipitation of $CaCO_3$, a final product. Generally, the ionic and precipitation reactions are fast, whereas the gas-liquid mass transfer and solid dissolutions are slow and regarded as rate-limiting steps because of the resistance between two different phases.

3.3.1. Kinetics of aqueous mineral carbonation process

Mass transfer between gas and liquid phase

$$\mathrm{CO_2(g)} \rightarrow CO_2(\mathrm{aq}). \qquad \text{Eq. 3-1}$$

This is a physical absorption of CO_2 gas to the liquid phase, whose transfer rate per unit gas volume is expressed as

$$r_{\mathrm{mass\ transfer}} = (\theta_{k_l} k_l) A_g (\theta_E E)(H^{CO2}[\mathrm{CO_2(g)}] - [CO_2(\mathrm{aq})]), \qquad \text{Eq. 3-2}$$

where k_l and E are the overall mass transfer coefficient and the enhancement factor by chemical reactions, to which the adjustment factors θ_{k_l} and θ_E are multiplied respectively, in order to compensate the uncertainties in the nominal parameters. A_g is the surface area per unit gas volume, H^{CO2} is the Henry constant of CO_2 in electrolyte solutions, and $[\cdot]$ denotes the molar concentrations of

corresponding species.

The overall mass transfer coefficient, k_l, is derived from Sherwood (Sh) relation [86],

$$Sh = \frac{k_l \theta_{d_b}}{D^{CO2}} = 2 + 0.015 Re^{0.89} Sc^{0.7}, \quad \text{Eq. 3-3}$$

where θ_{d_b} is the bubble diameter, which was assumed to have a constant value that must be found out by the parameter estimation. D^{CO2} is the diffusivity of CO_2 under alkaline environment, and Re and Sc are Reynolds and Schmidt numbers, respectively. The correlation of D^{CO2} is given by

$$\frac{D^{CO2}}{D_w^{CO2}} = 1 - 1.29 \times 10^{-4}[\mathrm{OH^-}], \quad \text{Eq. 3-4}$$

$$D_w^{CO2} = 2.35 \times 10^{-6} \exp\left(\frac{-2119}{T}\right), \quad \text{Eq. 3-5}$$

where D_w^{CO2} is the diffusivity of CO_2 in pure water [87].

Although the mass transfer coefficient can be calculated at each time step using the above correlations, uncertainties still exist in the hydrodynamics related terms like Re and Sc. Thus, an adjustment factor, θ_{k_l}, was introduced to compensate these uncertainties, and estimated from the experimental results.

The surface area per unit gas volume, A_g, is determined from the given bubble diameter, θ_{d_b}, and the gas holdup, α_g, as

$$A_g = \frac{\alpha_g}{\theta_{d_b}}. \quad \text{Eq. 3-6}$$

θ_{d_b} and α_g are uncertain but have significant influences on the mass transfer rate. Thus, it is advantageous to estimate them as parameters, rather than giving arbitrary

values. To reflect the change of gas holdup according to the gas inlet, a correlation with three parameters, θ_a, θ_b, and θ_c was introduced:

$$\alpha_g = \theta_a + \theta_b U_g^{\theta_c}, \qquad \text{Eq. 3-7}$$

where U_g is the superficial gas velocity. To sum up, four parameters, θ_{d_b}, θ_a, θ_b, and θ_c, are to be estimated.

The enhancement factor, E, is calculated from the correlation [88] of

$$E = \begin{cases} -\dfrac{Ha^2}{2(E_\infty - 1)} + \sqrt{\dfrac{Ha^4}{4(E_\infty - 1)^2} + \dfrac{E_\infty Ha^2}{E_\infty - 1} + 1}, & E_\infty > 1, \\ 1, & E_\infty \le 1, \end{cases} \qquad \text{Eq. 3-8}$$

where

$$E_\infty = \left(1 + \frac{[OH-]D^{CO2}}{2D^{CO2}H^{CO2}[\mathrm{CO_2(g)}]}\right)\sqrt{\frac{D^{CO2}}{D^{OH-}}}, \qquad \text{Eq. 3-9}$$

$$Ha = \frac{\sqrt{k_{11}D^{CO2}[\mathrm{OH^-}]}}{k_l}. \qquad \text{Eq. 3-10}$$

D^{OH-} is the diffusivity of OH^- ion, which takes the value of 5.3×10^{-9} [89], and k_{11} is the rate constant of a reaction between CO_2(aq) and OH^-(aq), which is discussed in the next part. The adjustment factor, θ_E, is multiplied to the Equation Eq. 3-8 when calculating the mass transfer rate. It is to represent all uncertain parameters involved in the Eq. 3-8 – Eq. 3-10.

The Henry constant for electrolyte solution, H^{CO2}, is obtained from

$$\log\left(\frac{H_w^{CO2}}{H^{CO2}}\right) = \sum_i (h_i + h_g)c_i, \qquad \text{Eq. 3-11}$$

$$H_w^{CO2} = 3.54 \times 10^{-7} RT \exp\left(\frac{2044}{T}\right), \qquad \text{Eq. 3-12}$$

where H_w^{CO2}, h_i, h_g and c_i are the Henry constant of CO_2 for pure water, the ion-specific parameter, the gas-specific parameter, and the concentration of each ion i, respectively. Eq. 3-11, Eq 3-12 and all the parameter values are adopted from literature [90, 91].

Solid dissolutions

$$\mathrm{Ca(OH)_2(s)} \underset{k_b}{\overset{k_f}{\rightleftharpoons}} \mathrm{Ca^{2+}(aq) + 2OH^-(aq)}, \qquad \text{Eq. 3-13}$$

$$\mathrm{CaOH^+(aq)} \underset{k_{b2}}{\overset{k_{f2}}{\rightleftharpoons}} \mathrm{Ca^{2+}(aq) + OH^-(aq)}, \qquad \text{Eq. 3-14}$$

$$\mathrm{NaOH(s)} \underset{k_{b3}}{\overset{k_{f3}}{\rightleftharpoons}} \mathrm{Na^+(aq) + OH^-(aq)}. \qquad \text{Eq. 3-15}$$

The dissolutions of alkaline solids provide mineral and hydroxide ions. All the forward and backward reaction rates of these reactions can be expressed as products of each reactant's concentration and the corresponding rate constants. The equilibrium and rate constants are given in Table 3-2. k_f and k_b in Eq. 3-13 are dependent on total surface area of the solid to reflect the decrease of dissolution rate owing to the shrinkage of the solid particles as the reaction proceeds. The value of k_{f2} was randomly set to 1,000 because relevant source could not be found. However, parameter estimation was not performed on it because the results were not affected by its value at all. k_{f3} and k_{b3} were also randomly set because they have negligible impacts on the results as long as NaOH completely dissolves in a short time.

Table 3-2. Kinetic parameters for solid dissolutions

	Definition	Unit	Reference
k_f	$2.2 \times 10^{-8} \cdot \exp\left(\frac{0.0297(T-298.15)}{298.15RT}\right)$	$\frac{\text{mol}}{L \cdot s \cdot \text{cm}^2}$	[92]
k_b	$1.9 \times 10^{-3} \cdot \exp\left(\frac{0.0528(T-298.15)}{298.15RT}\right)$	$\frac{\text{L}^2}{\text{mol}^2 \cdot s \cdot \text{cm}^2}$	[92]
K_{CaOH^+}	$10^{-1.299+260.388\left(\frac{1}{298}-\frac{1}{T}\right)}$	$\frac{mol}{L}$	[93]
k_{f2}	1,000	$\frac{1}{\text{s}}$	
k_{b2}	$\frac{k_{f2}}{K_{CaOH^+}}$	$\frac{\text{L}}{\text{mol} \cdot \text{s}}$	
k_{f3}	10^9	$\frac{\text{mol}}{\text{L} \cdot \text{s}}$	
k_{b3}	0	$\frac{\text{L}}{\text{mol} \cdot s}$	

Ionic reactions

$$\mathrm{CO_2(aq) + OH^-}(aq) \underset{k_{12}}{\overset{k_{11}}{\rightleftharpoons}} \mathrm{HCO_3^-(aq)}, \qquad \text{Eq. 3-16}$$

$$\mathrm{HCO_3^-(aq) + OH^-}(aq) \underset{k_{22}}{\overset{k_{21}}{\rightleftharpoons}} \mathrm{CO_3^{2-}(aq) + H_2O}, \qquad \text{Eq. 3-17}$$

$$\mathrm{H^+(aq) + OH^-}(aq) \underset{k_{32}}{\overset{k_{31}}{\rightleftharpoons}} \mathrm{H_2O}, \qquad \text{Eq. 3-18}$$

$$\mathrm{CO_2(aq) + H_2O} \underset{k_{42}}{\overset{k_{41}}{\rightleftharpoons}} \mathrm{HCO_3^-(aq) + H^+}(aq). \qquad \text{Eq. 3-19}$$

The above reactions represent the conversion of $\mathrm{CO_2(aq)}$ into bicarbonate and carbonate ions in an acid-base equilibrium. The forward and backward reaction rates follow the elementary reaction rate equations, like in the solid dissolutions. The equilibrium constants and rate constants are given in Table 3-3.

Table 3-3. Kinetic parameters of the ionic reactions

	Definition	Unit	Reference
K_1	$\frac{K_4}{K_w}$		
$k_{11}{}^{a}$	$\log\left(\frac{k_{11}}{k_{11}^{\infty}}\right) = 0.221I - 0.016I^2$	$\frac{\mathrm{L}}{\mathrm{mol}\cdot s}$	[94]
$k_{11}^{\infty\,b}$	$10^{11.916-\frac{2382}{T}}$	$\frac{\mathrm{L}}{\mathrm{mol}\cdot s}$	[94]
k_{12}	$\frac{k_{11}}{K_1}$		
K_2	$10^{\frac{1568.94}{T}+0.4134-0.00673T}$	$\frac{m^3}{mol}$	[95]
k_{21}	5×10^{7}	$\frac{m^3}{\mathrm{mol}\cdot\mathrm{s}}$	[96]
k_{22}	$\frac{k_{21}}{K_2}$		
K_w	$10^{-\frac{5839.51}{T}-22.4773\log(T)+61.2062}$	$\frac{mol^2}{L^2}$	[97]
k_{31}	1.4×10^{8}	$\frac{m^3}{mol\cdot\mathrm{s}}$	[97]
k_{32}	$K_w\cdot k_{31}$		[97]
K_4	$\mathrm{e}^{-\frac{12092.1}{T}-36.786\ln(T)+235.482}$	$\frac{kmol}{m^3}$	[98]
k_{41}	0.024	s^{-1}	[99]
k_{42}	k_{41}/K_4		[99]

[a] I is the ionic strength, $\mathrm{I} = 0.5\sum_i(\mathrm{c_i}\cdot\mathrm{z_i^2})$, where $\mathrm{z_i}$ is the absolute charge of a corresponding ion,

[b] $\mathrm{k_{11}}$ value at pure water.

Precipitations

$$Ca^{2+}(aq) + {CO_3}^{2-}(aq) \underset{k_{52}}{\overset{k_{51}}{\rightleftharpoons}} CaCO_3(s), \qquad \text{Eq. 3-20}$$

$$Ca^{2+}(aq) + {HCO_3}^{-}(aq) \underset{k_{62}}{\overset{k_{61}}{\rightleftharpoons}} CaCO_3(s) + H^{+}(aq). \qquad \text{Eq. 3-21}$$

Two reactions here explain production of the main product, calcium carbonate. Neither of these becomes a rate-limiting step because they are fast ionic reactions producing the thermodynamically stable product. The equilibrium and rate constants are given in Table 3-4.

Table 3-4. Kinetic parameters for precipitations.

	Definition	Unit	Reference
$K_{sp,CaCO_3}$ [a]	$10^{-171.9773+0.077993\mathrm{T}+\frac{2903.293}{\mathrm{T}}+71.595\log(T)}$	$\frac{mol^2}{L^2}$	[100]
k_{51}	$\frac{k_{52}}{K_{sp,CaCO_3}}$	$\frac{\mathrm{L}}{\mathrm{mol}\cdot\mathrm{s}}$	
k_{52}	9×10^{-3}	$\frac{\mathrm{mol}}{\mathrm{L}\cdot\mathrm{s}}$	[78]
k_{61}	4×10^{-2}	$\frac{\mathrm{L}}{\mathrm{mol}\cdot\mathrm{s}}$	[78]
k_{62}	10^6	s^{-1}	[78]

[a] This solubility product equation is for aragonite calcium carbonate.

3.3.2. Differential algebraic equation (DAE) model for the reactor

A set of differential algebraic equations (DAEs) was constructed based on the kinetics described in the previous parts. The exact formulations as well as the assumptions used in the model are explained in this section.

Assumptions

- The reactor consists of 10 vertical compartments with a same volume where the gas passes through each of them from the bottom. The concentration of CO_2(g) declines as it moves to the upper compartment (See Figure 3-2).
- The gas distribution is homogeneous everywhere, i.e. gas holdup has a constant value in all the compartments.
- Gas bubbles have a constant diameter and do not shrink during the reactions. It is reasonable because the portion of CO_2 is small compared to N_2.
- $Ca(OH)_2$ particles shrink as the reaction proceeds. The number of particles is fixed, while the total volume, surface area, and diameter vary. When $Ca(OH)_2$ is completely consumed, the surface area becomes zero and the dissolution no longer takes place.
- Solids and ions are uniformly distributed throughout the reactor, i.e. their concentrations have the same value in every compartment.

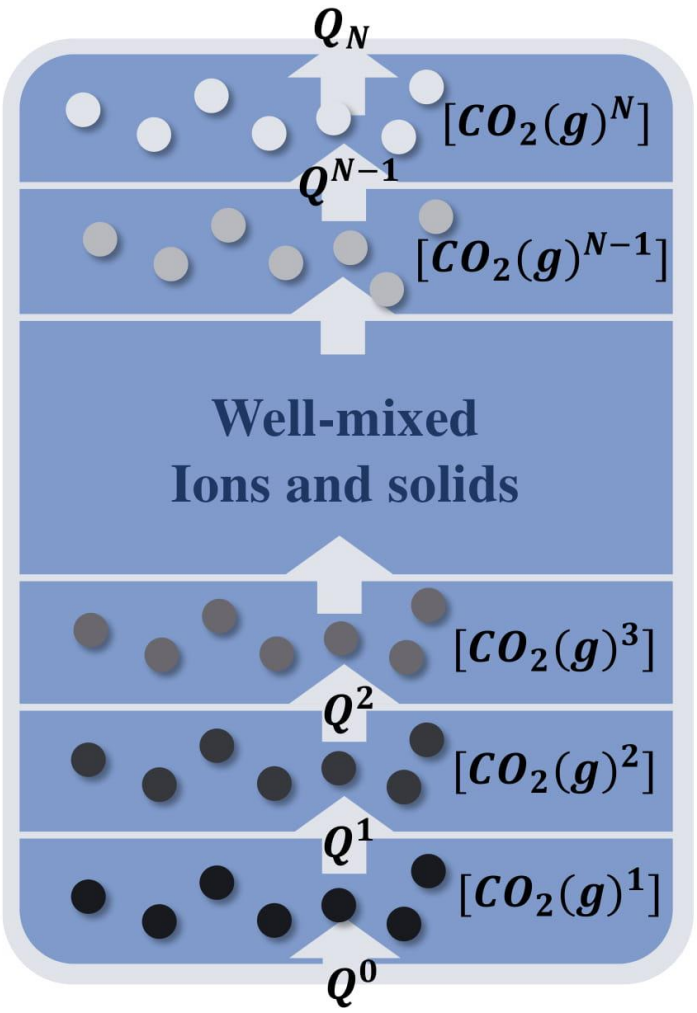

Figure 3-2. Schematic diagram of the compartment reactor model.

Model formulations

$$\frac{d[\mathrm{CO_2(g)}^i]}{dt} = Q^{i-1}\frac{[\mathrm{CO_2(g)}^{i-1}]}{V_{gas}} - Q^i\frac{[\mathrm{CO_2(g)}^i]}{V_{gas}} - \theta_{k_l}k_l\frac{6\left(\theta_a+\theta_b U_g^{\theta_c}\right)}{\theta_{d_b}}\theta_E E(H^{CO2}[\mathrm{CO_2(g)}^i] - [\mathrm{CO_2(aq)}]), \quad i = 1,\ldots,N, \qquad \text{Eq. 3-22}$$

$$\frac{d[\mathrm{CO_2(aq)}]}{dt} = -k_{11}[\mathrm{CO_2(aq)}][\mathrm{OH^-}] + k_{12}[\mathrm{HCO3^-}] - k_{41}[\mathrm{CO_2(aq)}] + k_{42}[\mathrm{HCO3^-}][\mathrm{H^+}] + \frac{V_{gas}}{V_R}\sum_{i=1}^{N}\left(\theta_{k_l}k_l\frac{6\left(\theta_a+\theta_b U_g^{\theta_c}\right)}{\theta_{d_b}}\theta_E E(H^{CO2}[\mathrm{CO_2(g)}^i] - [\mathrm{CO_2(aq)}])\right), \qquad \text{Eq. 3-23}$$

$$\frac{\mathrm{d}[\mathrm{HCO_3^-}]}{dt} = k_{11}[\mathrm{CO_2(aq)}][\mathrm{OH^-}] - k_{12}[\mathrm{HCO_3^-}] - k_{21}[\mathrm{HCO_3^-}][\mathrm{OH^-}] + k_{22}[\mathrm{CO_3^{2-}}] + k_{41}[\mathrm{CO_2(aq)}] - k_{42}[\mathrm{HCO_3^-}][\mathrm{H^+}] - k_{61}[\mathrm{Ca^{2+}}][\mathrm{HCO_3^-}] + k_{62}[\mathrm{H^+}], \qquad \text{Eq. 3-24}$$

$$\frac{\mathrm{d}\left[\mathrm{CO_3^{2-}}\right]}{dt}$$

$$= k_{21}\left[\mathrm{HCO_3^-}\right]\left[\mathrm{OH^-}\right] - k_{22}\left[\mathrm{CO_3^{2-}}\right] \qquad \text{Eq. 3-25}$$

$$- k_{51}\left[\mathrm{Ca^{2+}}\right]\left[\mathrm{CO_3^{2-}}\right] + k_{52},$$

$$\frac{\mathrm{d}[\mathrm{H^+}]}{dt}$$

$$= -k_{31}[\mathrm{OH^-}][\mathrm{H^+}] + k_{32} - k_{42}[\mathrm{HCO_3^-}][\mathrm{H^+}] \qquad \text{Eq. 3-26}$$

$$+ k_{41}[\mathrm{CO_2(aq)}] + k_{61}[\mathrm{Ca^{2+}}][\mathrm{HCO_3^-}] - k_{62}[\mathrm{H^+}],$$

$$\frac{d[\mathrm{OH^-}]}{dt}$$

$$= -k_{11}[CO_2(\mathrm{aq})][OH^-] + k_{12}[\mathrm{HCO_3^-}]$$

$$- k_{21}[\mathrm{HCO_3^-}][\mathrm{OH^-}] + k_{22}[\mathrm{CO_3^{2-}}]$$

$$- k_{31}[\mathrm{OH^-}][\mathrm{H^+}] \qquad \text{Eq. 3-27}$$

$$+ 2\left(\theta_{A_s} \cdot A_s\right)\left(k_f - k_b[\mathrm{Ca^{2+}}]f^4[\mathrm{OH^-}]^2 f^2\right)$$

$$+ k_{f2}[\mathrm{CaOH^+}] - k_{b2}[\mathrm{Ca^{2+}}][\mathrm{OH^-}] + k_{f3}$$

$$- k_{b3}[\mathrm{Na^+}][\mathrm{OH^-}],$$

$$\frac{d[Ca^{2+}]}{dt}$$

$$= -k_{51}[\mathrm{Ca^{2+}}][\mathrm{CO_3^{2-}}] + k_{52} - k_{61}[\mathrm{Ca^{2+}}][\mathrm{HCO_3^-}]$$

$$+ k_{62}[\mathrm{H^+}] + \theta_{A_s}A_s(k_f[\mathrm{Ca(OH)_2}] \qquad \text{Eq. 3-28}$$

$$- k_b[\mathrm{Ca^{2+}}]f^2[\mathrm{OH^-}]^2 f^4) + k_{f2}[\mathrm{CaOH^+}]$$

$$- k_{b2}[\mathrm{Ca^{2+}}][\mathrm{OH^-}] + k_{f3},$$

$$\frac{d[\mathrm{CaOH^+}]}{dt}$$

$$= -k_{f2}[\mathrm{CaOH^+}] + k_{b2}[\mathrm{Ca^{2+}}][\mathrm{OH^-}] + k_{f3}, \quad \text{Eq. 3-29}$$

$$\frac{d[\mathrm{Na+}]}{dt} = k_{f3} - k_{b3}[\mathrm{Na^+}][\mathrm{OH^-}], \quad \text{Eq. 3-30}$$

$$\frac{d[\mathrm{CaCO_3}]}{dt}$$

$$= k_{51}[\mathrm{Ca^{2+}}][\mathrm{CO_3^{2-}}] - k_{52} + k_{61}[\mathrm{Ca^{2+}}][\mathrm{HCO_3^-}] \quad \text{Eq. 3-31}$$

$$- k_{62}[\mathrm{H^+}],$$

$$Q^i$$

$$= Q^{i-1}$$

$$- \frac{RT}{P}\theta_{k_l}k_l\frac{6\left(\theta_a + \theta_b U_g^{\theta_c}\right)}{\theta_{d_b}}\theta_E E(H^{CO2}[\mathrm{CO_2(g)}^i] \quad \text{Eq. 3-32}$$

$$- [CO2(aq)])V_{gas},$$

$$V_{CaOH_2}$$

$$= \frac{1}{\rho_{Ca(OH)_2}}(Z^0_{Ca(OH)_2} - ([\mathrm{Ca^{2+}}] + [\mathrm{CaOH^+}] \quad \text{Eq. 3-33}$$

$$+ [\mathrm{CaCO_3}])MW_{CaOH_2}V_R),$$

$$A_s = (\frac{\pi}{n_s})^{\frac{1}{3}}(6V_{Ca(OH)_2})^{\frac{2}{3}}, \quad \text{Eq. 3-34}$$

$$n_s = \frac{Z_0}{\frac{4}{3}\rho_{Ca(OH)_2}\pi\left(\frac{\theta_{d_s^0}}{2}\right)^3}, \quad \text{Eq. 3-35}$$

$$\log(f) = \frac{-0.5\sqrt{I}}{1 + 1.4\sqrt{I}}, \quad \text{Eq. 3-36}$$

$$I = 0.5(4[\mathrm{Ca^{2+}}] + [\mathrm{H^+}] + [\mathrm{OH^-}] + [\mathrm{HCO_3^-}] + 4[\mathrm{CO_3^{2-}}] + [\mathrm{CaOH^+}] + [\mathrm{Na^+}]). \quad \text{Eq. 3-37}$$

In Eq. 3-22, $[\mathrm{CO_2(g)^i}]$, V_{gas}, and Q^i are the concentrations of $\mathrm{CO_2(g)}^i$ in the i^{th} compartment, the volume of mixed gas in one compartment, and the volumetric gas flow rate from the compartment $i-1$ to i, respectively. $[\mathrm{CO_2(g)^0}]$ is the inlet CO_2(g) concentration, which can be calculated from the design variable, ϕ_{CO2}^{inlet}, using the ideal gas law. Q^0 is the volumetric gas flow rate, which is equivalent to the design variable, V. V_{gas} can be calculated as the product of the gas holdup and the compartment volume, i.e., $V_{gas} = (\theta_a + \theta_b U_g^{\theta_c}) \times \frac{V_R}{N}$. V_R in Eq. 3-23 is the volume of the reactor. A_s in Eq. 3-27, is the total surface area of $Ca(OH)_2$ particles, θ_{A_s} is an adjustment factor to compensate the uncertainty in A_s, and f is the activity coefficient. In Eq. 3-33, $\rho_{Ca(OH)_2}$, $Z^0_{Ca(OH)_2}$, and $MW_{Ca(OH)_2}$ are the density, molecular weight and initial weight of $Ca(OH)_2$, respectively. In Eq. 3-34 and Eq. 3-35, n_s is the number of the particles and $\theta_{d_s^0}$ is the initial diameter of $Ca(OH)_2$ particles, which is one of the important but uncertain parameters in this work. The other algebraic equations such as k_{11}, H^{CO_2}, k_l, and E are already explained in previous sections.

Parameters ($\boldsymbol{\theta}$) to estimate

To sum up, there are eight parameters ($\boldsymbol{\theta}$) to estimate in total: θ_a, θ_b, and θ_c are the parameters which are related to the gas holdup, θ_{d_b} and $\theta_{d_s^0}$ are the initial

diameters of gas bubbles and solid particles, and θ_{k_l}, θ_E, and θ_{A_s} are the adjustment factors for uncertain parameters in the reactor model.

Output responses (y)

Two output responses, $\mathbf{y}_1$(CO_2 volume concentration of outlet flue gas) and $\mathbf{y}_2$ (*p*H), were monitored during the experiments. From the proposed model, they are defined as

$$\mathbf{y}_1 = \phi_{CO2}^{outlet}, \quad \text{Eq. 3-38}$$

$$\mathbf{y}_2 = -\log(K_w) + \log([\mathrm{OH}^-]). \quad \text{Eq. 3-39}$$

3.3.3. Discrete events for simulation procedure

Three discrete events, which need the reinitialization of the DAE model, can happen. The first is the entrance of the gas to the reactor. In the experiments, the gas is allowed to enter the reactor after given a time for NaOH and $Ca(OH)_2$ to sufficiently dissolve in water. The model reproduced the same procedure by first running the DAE model without CO_2-related variables. The second and third are the complete dissolution of NaOH and $Ca(OH)_2$, respectively. After the complete dissolution of solid particles, the dissolution kinetics of each solid species were deactivated. If not, Na^+, Ca^{2+}, and OH^- ions can be generated infinitely even after the sources are gone. Furthermore, if the kinetic parameters were forced to be zero rather than finding an exact event time using a root finding algorithm, convergence problems could happen. To prevent this, external functions, $g([Ca(OH)_2])$ and $g([NaOH])$, are introduced to calculate the remaining weights of $Ca(OH)_2$ and NaOH:

$$g([\mathrm{Ca(OH)_2}]) = Z^0_{CaOH} - ([\mathrm{Ca^{2+}}] + [\mathrm{CaCO_3}] + [\mathrm{CaOH^+}])MW_{\mathrm{Ca(OH)_2}}, \quad \text{Eq. 3-40}$$

$$g([\mathrm{NaOH}]) = Z^0_{NaOH} - [\mathrm{Na^+}]MW_{NaOH}, \quad \text{Eq. 3-41}$$

where Z^0 and MW are the initial weight and molecular weight of each species, respectively. When these functions give zero values, k_f, k_b, k_{f3}, and k_{b3} are set to zero and the model is reinitialized.

3.3.4. Numerical setting

The proposed mathematical model was written in Matlab script. Sundials IDAS solver with the dense linear solver and zero-crossing root-finding algorithm [83] was used to handle the stiff and hybrid DAEs system. Furthermore, since the kinetics show stiff behaviors like $10^8 - 10^9$ order-of-magnitude difference among parameters, the model occasionally fails to converge within a feasible time. Thus, the divergence of the solver was monitored and solver parameters such as relative tolerance (10^{-7}) and absolute tolerance (10^{-7}) are tuned to make as many samples converged as possible. The simulations were done on Intel Xeon E5-2667 v4 (3.2 GHz) machine on which the average simulation time for one scenario was less than one second.

3.4. Bayesian parameter estimation

One objective of this study is to infer posterior distributions $\mathcal{P}(\boldsymbol{\theta})$ of the unknown parameters, $\boldsymbol{\theta}$, from experimental data. This problem has characteristics that data

acquisition is expensive, a non-adpative black-box (a factorial method) [101-104] is used as an experiment design method, and the mathematical model is complex to perform Markov chain Monte Carlo (MCMC) sampling. Taken together, this problem is tackling the Bayesian parameter estimation problem with a small number of data sets and complex model.

3.4.1. Problem formulation

Here, the response is a time series: $\mathbf{y} = \{y_1, y_2, \cdots, y_t, \cdots, y_T\}$, written in the form of a T-dimensional vector. Each experiment reports multiple response types, $\{\mathbf{y}_1, \cdots, \mathbf{y}_D\}$, where each response $\mathbf{y}_d$ is a T-dimensional vector. The number of total responses are two ($D = 2$) in this problem: $\mathbf{y}_1$ measures the CO_2 volume concentration of outlet flue gas, and $\mathbf{y}_2$ the *p*H of the solution. In the experiments, the response length T is fixed for $\mathbf{y}_1$ and $\mathbf{y}_2$ from the same experiment, because they are measured simultaneously (See Figure 3-3). A finite sets of design variables $\{\mathbf{x}^{(1)}, \cdots, \mathbf{x}^{(M)}\}$ that correspond to multiple experiments, where $\mathbf{x} = (T, \phi_{CO2}^{inlet}, w_{Ca(OH)2}, w_{NaOH}, \dot{V})$ are considered. The number of total experiments, $M = 16$; M cannot be very large in most cases, because experiments are costly. The length of response T may be different for different experiments. With $M = 16$ experiments and $D = 2$ response types, the total datases are $M \times D = 32$; a single "dataset" indicates $\{\mathbf{x}^{(m)}, \mathbf{y}_d^{(m)}\}$ of a particular (m, d), where $m = 1, \cdots, M$ and $d = 1, \cdots, D$.

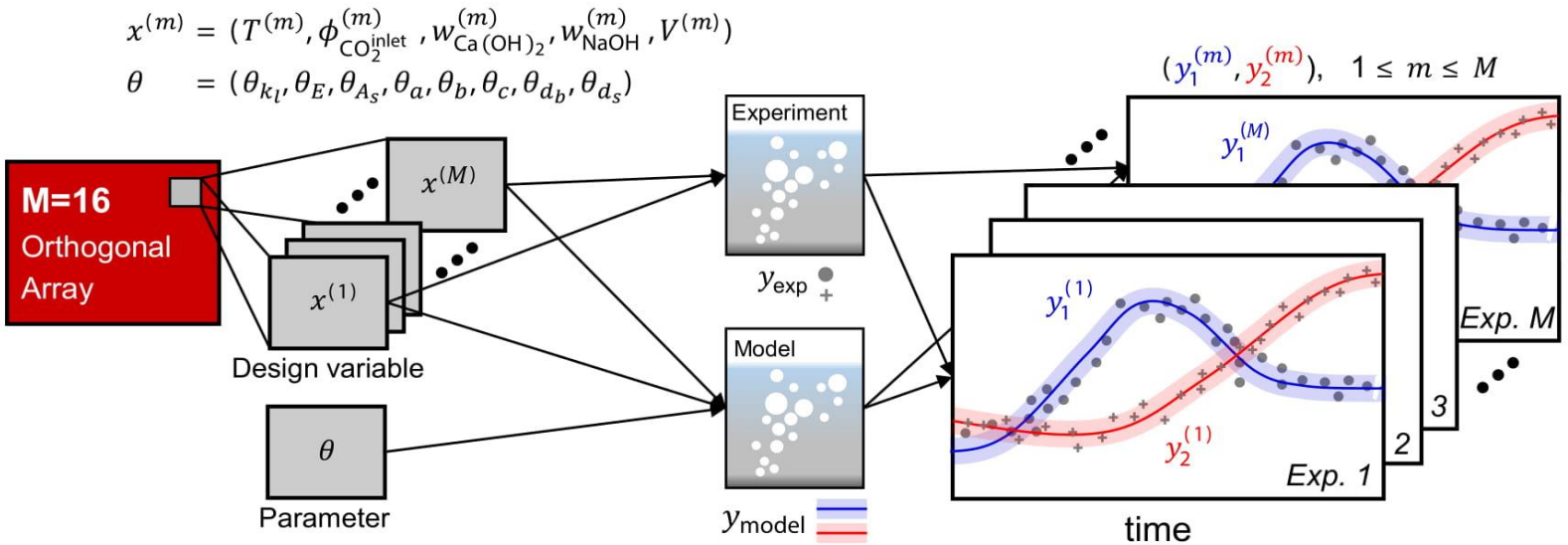

Figure 3-3. Schematic diagram of the problem setting.

Let me denote the first-principle model in previous section by $\mathbf{f}$. Given a set of design variables $\mathbf{x}$ and a fixed set of parameters $\boldsymbol{\theta}$, the model predicts a response time series as $\mathbf{y}_{model} = \mathbf{f}(\mathbf{x}, \boldsymbol{\theta})$. Here $\boldsymbol{\theta}$ is a K-dimensional parameter vectors, where $K = 8$ in the current problem. Specifically, $\boldsymbol{\theta} = (\theta_E, \theta_{A_s}, \theta_a, \theta_b, \theta_c, \theta_{d_b}, \theta_{d_s^0}, \theta_{k_l})$. In general, there is always some discrepancy (or model-plant mismatch) between the actually observed response $\mathbf{y}$ and the modeled response $\mathbf{y}_{model}$. It is mathematically expressed as $\mathbf{y} = \mathbf{f}(\mathbf{x}, \boldsymbol{\theta}) + \boldsymbol{\epsilon}$, where $\boldsymbol{\epsilon}$ is the error vector. An assumption that the error $\boldsymbol{\epsilon}$ is distributed according to a multivariate normal distribution, with a $T \times T$ covariance matrix Σ [27, 35] is introduced:

$$\boldsymbol{\epsilon} = \mathbf{y} - \mathbf{f}(\mathbf{x}, \boldsymbol{\theta}) \sim \mathcal{N}(\mathbf{0}, \Sigma). \qquad \text{Eq. 3-42}$$

For a complicated kinetic model, calculation of the model response $\mathbf{f}(\mathbf{x}, \boldsymbol{\theta})$ while varying the value of $\boldsymbol{\theta}$ can be computationally demanding. To make computations affordable, various surrogate models can be applied such as neural networks, Gaussian process, and PCE. This study approximates the modeled response using a quadratic hyper-surface to avoid additional training step:

$$\mathbf{f}(\mathbf{x}, \boldsymbol{\theta}) \approx \tilde{\mathbf{f}}(\boldsymbol{\theta}) = c + \mathbf{b}^{\top}\boldsymbol{\theta} + \boldsymbol{\theta}^{\top} A \boldsymbol{\theta}, \qquad \text{Eq. 3-43}$$

where $\tilde{\mathbf{f}}(\boldsymbol{\theta})$ is the surrogate model response, A is a symmetric $K \times K$ matrix, $\mathbf{b}$ is a vector of length K, and c is a scalar, and K is the dimensionality of $\boldsymbol{\theta}$. The parameters were sampled on a Central Composite Design (CCD) and a Latin hypercube sampling (LHS)[105] (1,000 samples in total) within the prior hypercube. The quadratic surface fit was performed separately for each dataset (m, d), to obtain an approximate response function $\tilde{\mathbf{f}}^{(m,d)}$ such that $\mathbf{y}_d^{(m)} \approx \tilde{\mathbf{f}}^{(m,d)}(\mathbf{x}^{(m)}, \boldsymbol{\theta})$.

3.4.2. Bayesian posterior inference

According to the Bayes rule, the posterior distribution $\mathcal{P}(\boldsymbol{\theta})$ is formulated like

$$\mathcal{P}(\boldsymbol{\theta}) \equiv p(\boldsymbol{\theta}|\mathrm{d}ata) \propto p(\mathrm{d}ata|\boldsymbol{\theta}) \cdot p(\boldsymbol{\theta}), \qquad \text{Eq. 3-44}$$

where $p(\mathrm{d}ata|\boldsymbol{\theta})$ is the likelihood of observing the data from a model parameterized by $\boldsymbol{\theta}$, and $p(\boldsymbol{\theta})$ is the prior distribution on $\boldsymbol{\theta}$. In the rest of this section outlines how to construct the posterior distribution by calculating the likelihood and specifying a prior distribution, and how the posterior can be sampled by the MCMC method. Please refer to the Supplementary Material of my paper [77] for the details.

Likelihood

According to the Gaussian error assumption, the likelihood of a given set of data depends not only on $\boldsymbol{\theta}$, but also on the covariance matrix Σ. In this sense, Σ is another parameter in the inference problem, although it is not of my primary interest; only interested is the distribution of $\boldsymbol{\theta}$. A full-fledged Bayesian approach for this problem is to consider the joint parameter space of $(\boldsymbol{\theta}, \Sigma)$ and then to marginalize over Σ at the end, as in some of the previous works [27, 35]. This work takes a different approach, in which the error covariance $\hat{\Sigma}$ is directly estimated from the data and an inferred distribution over $\boldsymbol{\theta}$, and the distribution over Σ is simply assumed to be highly localized around its "true" value, $\hat{\Sigma}$. In other words, it is aimed to calculate

$$p(\mathrm{d}ata|\boldsymbol{\theta}) = \int d\Sigma\, p(\mathrm{d}ata|\boldsymbol{\theta}, \Sigma)\, p(\Sigma)$$
$$\approx p(\mathrm{d}ata|\boldsymbol{\theta}, \hat{\Sigma}).$$

Eq. 3-45

The error covariance $\hat{\Sigma}$ is estimated separately for each dataset, reflecting the fact that each observation may come with a different amount of uncertainty. Specifically, the covariance matrix is parameterized in an exponential form, so that the covariance element between the two time-points t_i and t_j is modeled as $\Sigma_{ij} = \sigma^2 \exp(-|t_i - t_j|/\tau)$, and estimate the fluctuation scale σ and the de-correlation timescale τ. Estimation of the fluctuation scale σ is performed by taking an average over the posterior distribution, which requires an iterative algorithm. See Figure 3-4 for a schematic illustration.

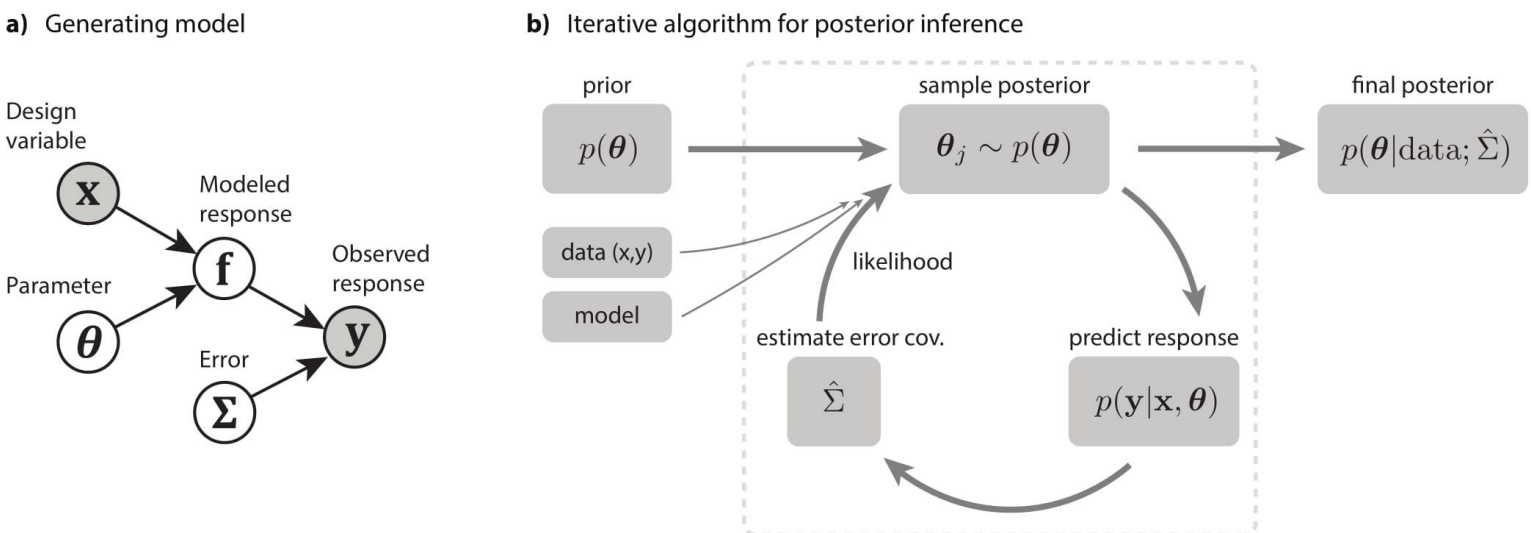

Figure 3-4. (a) A graphical representation of model generation. The observed response is considered as a noisy version of the modeled (ideal) response. (b) Schematic for the Bayesian inference.

For multiple datasets, in general, the likelihood $p(\mathrm{d}ata|\boldsymbol{\theta})$ involves a multiple integral over the Σ's; if all M experiments and D responses are considered, the total likelihood will be written as

$$p(\mathrm{d}ata|\boldsymbol{\theta}) = \int d\Sigma_{1,1} \cdots \int d\Sigma_{M,D}\, p(\mathrm{d}ata|\boldsymbol{\theta}, \Sigma_{1,1}, \cdots, \Sigma_{M,D})\, p(\Sigma_{1,1}) \cdots p(\Sigma_{M,D}). \quad \text{Eq. 3-46}$$

With the localization assumption of Eq. 3-45, the total likelihood can be simply separated as

$$p(\mathrm{d}ata|\boldsymbol{\theta}) \approx \prod_{m=1}^{M} \prod_{d=1}^{D} p((\mathbf{x}^{(m)}, \mathbf{y}_d^{(m)})|\boldsymbol{\theta}, \Sigma_{m,d}). \quad \text{Eq. 3-47}$$

Therefore, the joint likelihood of multiple datasets can be expressed as the product of the individual-dataset likelihoods.

Prior

A uniform prior distribution with a range constraint, such that $p(\theta) \propto 1$ if $\boldsymbol{\theta} \in \mathcal{C}$ and $p(\theta) = 0$ otherwise, defined by a hypercube $\mathcal{C} \subset \mathbb{R}^8$, is used. The detailed boundary values of the hypercube $\mathcal{C}$, which are basically ranges of each parameter, are described in Table 3-5. In order to ensure that the entire parameter space is efficiently explored by the MCMC sampling, the log of a parameter elements are implemented when the prior range spans multiple orders of magnitude.

Table 3-5. The prior range for the parameter $\boldsymbol{\theta}$

Parameter	Min.	Max.	Description
$\log(\theta_E)$	-3	3	Adjustment factor for enhancement factor
$\log(\theta_{A_s})$	-3	3	Adjustment factor for surface area of $CaCO_3$
θ_a	0	0.3	Related to gas holdup
θ_b	0	0.3	Related to gas holdup
$\log(\theta_c)$	-2	2	Related to gas holdup
$\log(\theta_{d_b})$	0	1.48	Initial diameter of bubbles
$\log(\theta_{d_s^0})$	-7	-1	Initial diameter of $CaCO_3$ particles
$\log(\theta_{k_l})$	-3	3	Adjustment factor for mass transfer coefficient

3.4.3. Sampling

MCMC sampling with the Metropolis-Hastings algorithm [106] was performed to approximate the posterior distribution. This work uses an iterative sampling algorithm to adaptively adjust the proposal distribution of the Metropolis-Hastings sampler, as well as to estimate the error covariance at the same time. Once a chain of parameters, $\{\boldsymbol{\theta}_1, \cdots, \boldsymbol{\theta}_N\}$ has been sampled, the response to a given design variable $\mathbf{x}$ that is predicted by the posterior is:

$$\mathbf{f}_{mean}(\mathbf{x}) = \frac{1}{N}\sum_{n=1}^{N} \mathbf{f}(\mathbf{x}, \boldsymbol{\theta}_n), \qquad \text{Eq. 3-48}$$

where N is the number of parameter samples in the chain. Similarly, the mean of all obtained samples can be obtained as the representative value of the posterior distribution:

$$\boldsymbol{\theta}_{mean} = \frac{1}{N}\sum_{n=1}^{N} \boldsymbol{\theta}_n. \qquad \text{Eq. 3-49}$$

It is also possible to extract mode ($\boldsymbol{\theta}_{mode}$) among a chain of parameters in two-dimensional parameter space. However, it is difficult to extract mode from the multi-dimensional parameter space because of the difficulty of defining the unit volume for calculating the number samples. Thus, the mode is sequentially extracted from two-dimensional parameter space and the final one is used.

3.5. Results and discussions

3.5.1. Stochastic output response

When the entire process of Bayesian parameter estimation is completed, the probability distributions of the output responses as well as $\boldsymbol{\theta}$ can be obtained as in Figure 3-5. It shows that the deterministic model can be non-intrusively extended to the stochastic model through Bayesian parameter estimation. The uncertainties from the model-plant mismatch or the plant disturbance are reflected in the parameters and propagated to the output responses through them. The propagated uncertainties in the output responses are visualized in Figure 3-5 (a) with the standard deviation or the confidence interval (CI).

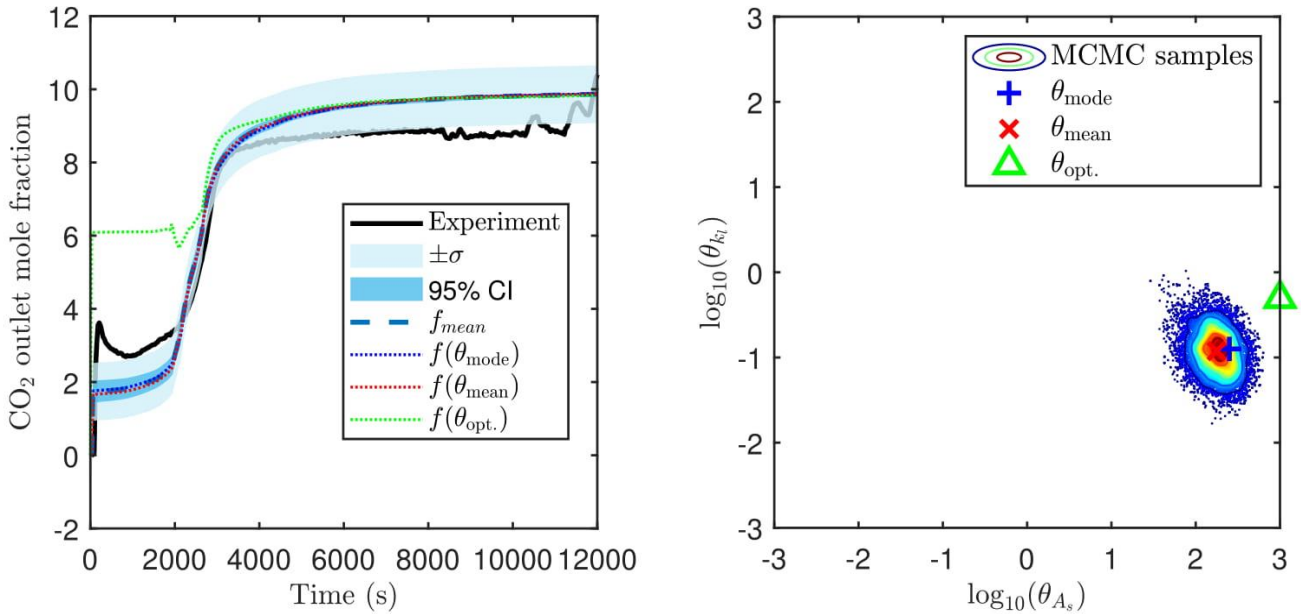

Figure 3-5. : a) Estimated output response (ϕ_{CO2}^{outlet}) fitting and b) joint marginal posterior distribution of $\log_{10}(\theta_{k_l})$ and $\log_{10}(\theta_{A_s})$ for Exp. 6 using mode, mean, and optimization method.

However, there are occasions where it is needed to pick a single response curve rather than handling a stochastic model. A straightforward way is to choose a single representative value of $\boldsymbol{\theta}$ like $\boldsymbol{\theta}_{mode}$ or $\boldsymbol{\theta}_{mean}$ from the posterior distribution and solve the model with it to earn a single response, i.e. $\mathbf{f}(\boldsymbol{\theta}_{mode})$ or $\mathbf{f}(\boldsymbol{\theta}_{mean})$. Another way is to sample many $\boldsymbol{\theta}$ from the posterior, solve the model using each of them and take the average to get the representative response, i.e. $\mathbf{f}_{mean}$. If the posterior had the normal distribution, all three of them, namely $\mathbf{f}(\boldsymbol{\theta}_{mode})$, $\mathbf{f}(\boldsymbol{\theta}_{mean})$ and $\mathbf{f}_{mean}$, would follow an exactly same trajectory. However, when the posterior has multiple peaks like in Figure 3-6, it is beneficial to adopt $\mathbf{f}_{mean}$ among them because $\mathbf{f}(\boldsymbol{\theta}_{mode})$ has a risk that $\boldsymbol{\theta}_{mode}$ is not picked from the highest peak and $\mathbf{f}(\boldsymbol{\theta}_{mean})$ could be inferior to $\mathbf{f}(\boldsymbol{\theta}_{mode})$ when $\mathbf{f}$ is not monotonic with respect to $\boldsymbol{\theta}$.

Figure 3-5 a) shows $\mathbf{f}(\boldsymbol{\theta}_{mode})$, $\mathbf{f}(\boldsymbol{\theta}_{mean})$ and $\mathbf{f}_{mean}$. It is noticeable that $\mathbf{f}(\boldsymbol{\theta}_{mean})$ and $\mathbf{f}_{mean}$ are almost overlapped, suggesting that the response is changing monotonically with respect to $\boldsymbol{\theta}$. Based on these observations, it is concluded to use $\mathbf{f}(\boldsymbol{\theta}_{mean})$ and $\mathbf{f}_{mean}$ throughout the further discussions where a deterministic single response curve is required.

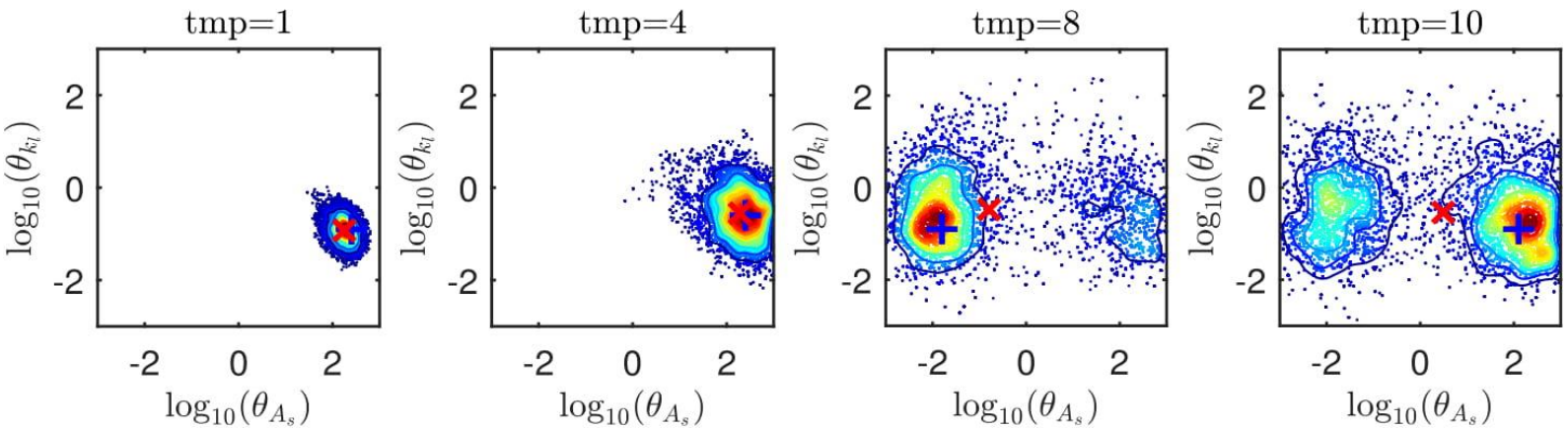

Figure 3-6. Tempering control (tempering factor as 1, 4, 8, and 10 respectively) for checking multimodal posterior distribution between θ_{A_s} and θ_{kl}; also compare the θ_{mean} and θ_{mode} movements. $\times$ denotes mean and $+$ denotes mode.

3.5.2. Quality of parameter estimtates

It was able to fit most of the observed responses with good accuracies. (See Figures 3-7, 8.) This means that the DAE model captures the important features of a complicated CCU system in which multiple phases and reactions are involved in a discrete manner and that the proposed parameter estimation method works. The goodness of fit of the model responses is quantitatively measured and compared with the results from several optimization methods using the following fitting error equation,

$$error = \sqrt{\sum_{m=1}^{M}\sum_{d=1}^{D}\frac{(\mathbf{y}_d^{(m)} - \tilde{\mathbf{f}}^{(m,d)}(\mathbf{x}^{(m)}, \boldsymbol{\theta}))(\mathbf{y}_d^{(m)} - \tilde{\mathbf{f}}^{(m,d)}(\mathbf{x}^{(m)}, \boldsymbol{\theta}))^{\top}}{(\sigma^{(m,d)})^2 T^{(m)}}}. \quad \text{Eq. 3-50}$$

Three different solvers, a genetic algorithm (GA), a dividing hyper-rectangle (DIRECT) [107-109], and a sequential quadratic programming (SQP), were used to find the $\boldsymbol{\theta}_{opt}$ which minimizes Eq. 3-50. The maximum number of iterations was same as in the Bayesian method for a fair comparison.

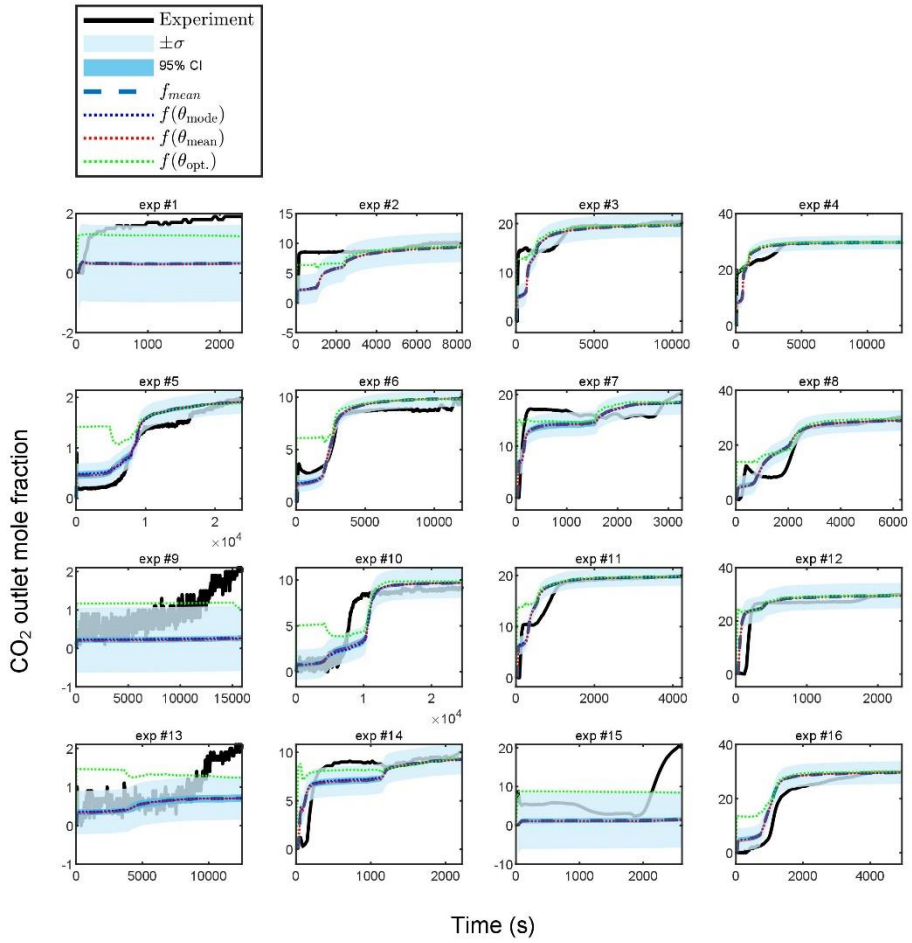

Figure 3-7. Estimated output response (ϕ_{CO2}^{outlet}) fitting with experimental data, f_{mean}, $f(\theta_{mode})$, $f(\theta_{mean})$, and $f(\theta_{opt})$. Uncertainty quantification using standard deviation and confidence interval is also conducted.

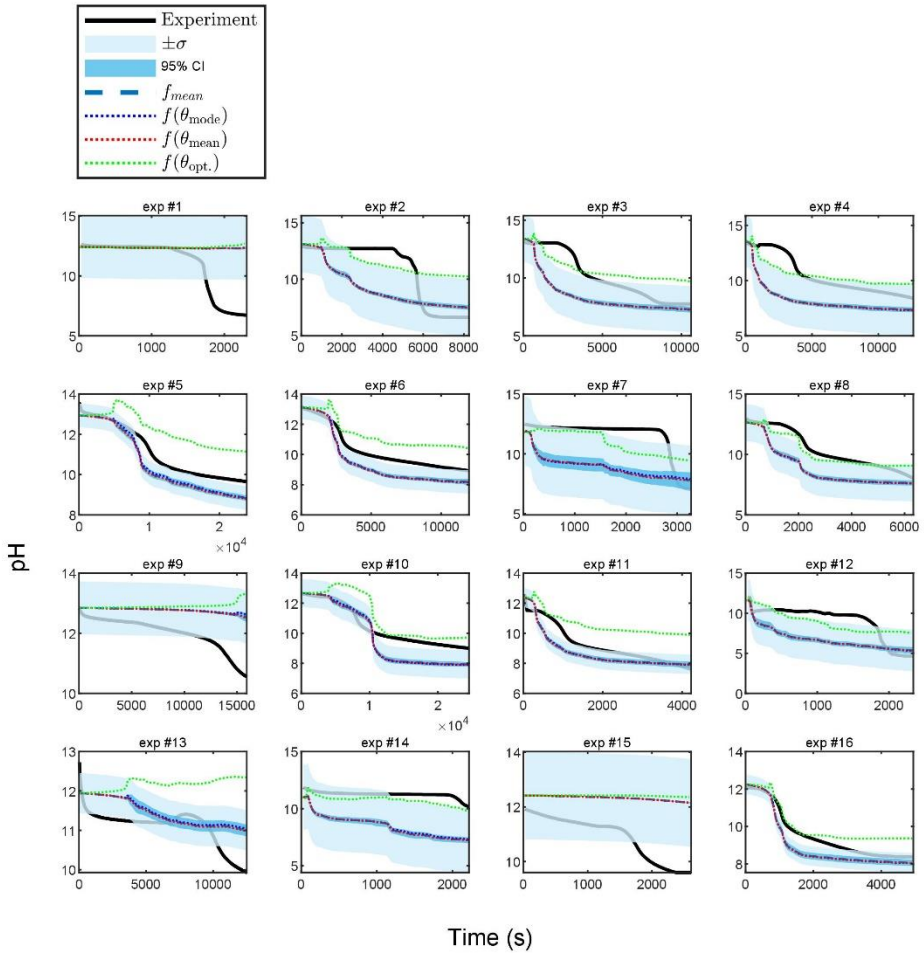

Figure 3-8. Estimated output response (pH) fitting with experimental data, $\mathbf{f}_{mean}$, $\mathbf{f}(\boldsymbol{\theta}_{mode})$, $\mathbf{f}(\boldsymbol{\theta}_{mean})$, and $\mathbf{f}(\boldsymbol{\theta}_{opt})$. Uncertainty quantification using standard deviation and confidence interval is also conducted.

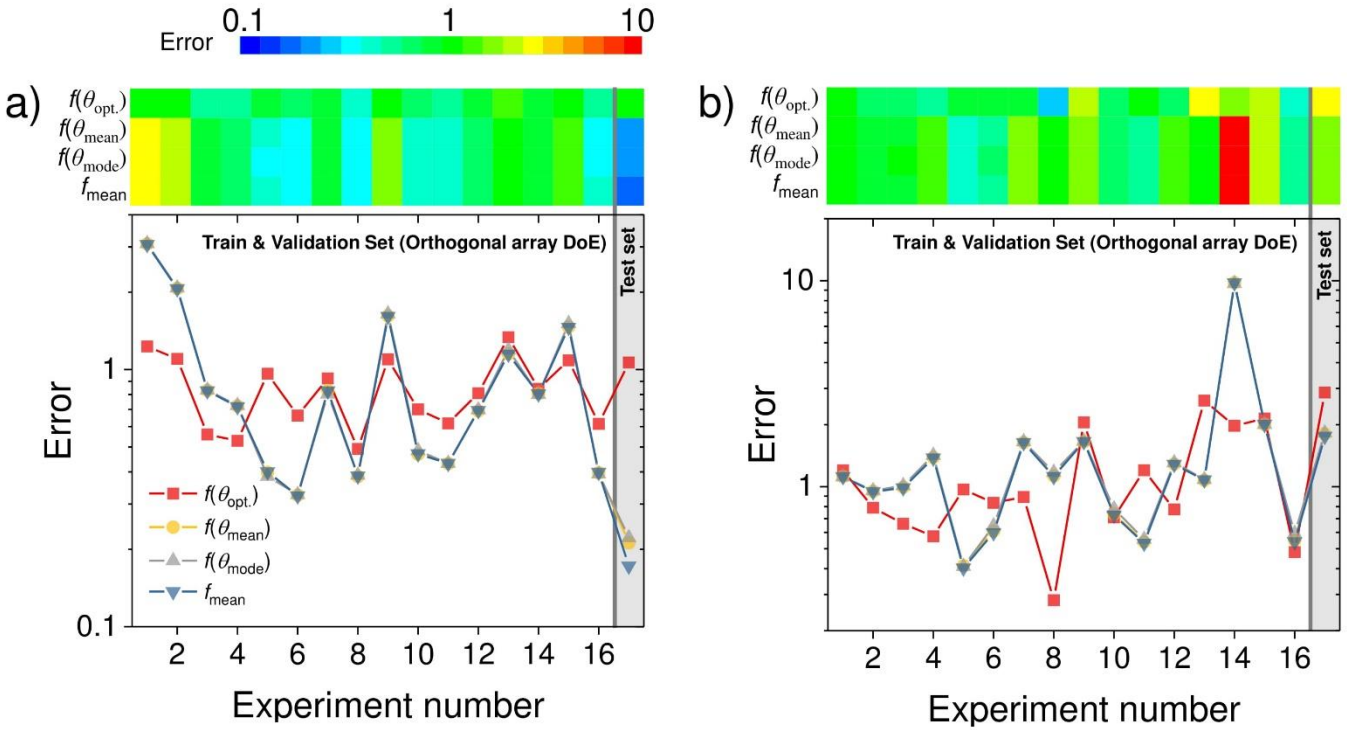

Figure 3-9. Error comparison through different parameter estimation methods. Visualize the error with a) CO_2 volumetric concentration of outlet flue gas (ϕ_{CO2}^{outlet}) and b) pH

In Figure 3-9 , the fitting errors of $\mathbf{f}(\boldsymbol{\theta}_{mean})$, $\mathbf{f}(\boldsymbol{\theta}_{mode})$, $\mathbf{f}_{mean}$ and $\mathbf{f}(\boldsymbol{\theta}_{opt})$ for all 17 experiments and 2 responses are shown. Overall, none of them shows dominant performance to others. Although the variance of errors is higher in the Bayesian estimation than in the optimization, the average of them have similar magnitudes in both methods. It means that the estimation method can provide deterministic parameter values which are as feasible as optimizations can give while suggesting the probability distributions as well. In addition, one dataset was left unseen during the parameter estimation to measure the fitting errors of obtained parameters on the test dataset. The resulting test set errors are acceptable compared to the other experiments. Particularly, the errors from Bayesian estimation are distinctively lower than the errors from the optimizations in both responses. It supposes that my method is better in covering the unseen operating ranges than deterministic approaches are.

However, Exp. 1 and 14 seem to show particularly higher errors than the others. It is suspected to have two reasons. First, since the MCMC sampling cannot perform sampling outside the parameter boundaries, the optimal parameter cannot be estimated correctly near the boundary. Second, the absence of NaOH makes ϕ_{CO2}^{outlet} reach ϕ_{CO2}^{inlet} very quickly and the experiment terminate early. Thus, $\mathrm{T}^{(m)}$ is shortened and the error is increased. The error in Eq. 3-50 is divided by $\mathrm{T}^{(m)}$. In addition, short experiments cannot reflect the slow dynamics of $Ca(OH)_2$. However, Exp. 7 and 12 show lower errors than Exp. 14 although they are lack of NaOH as well. In Exp. 14, the removal efficiency converges to 0 and the experiment is over before pH drops enough. It seems like the proposed algorithm, which focuses on stiff response dynamics through de-correlation timescale τ, recognized little contribution

on this dataset compared to the others.

3.5.3. Assessment of parameter uncertainties

Final MCMC sampling was conducted with 5,000 samples, 10 maximum iterations, tight chain criterion, and 0.5 step scale factor at each iteration step. At the final sampling, the number of samples and burn set to 20,000 and 2,000, respectively.

Figure 3-10 gives the visulaizations of two-dimensional joint marginal posterior distributions as well as marginal posterior distributions of the parameters which were sampled using the entire datasets (all 16 experiments and 2 responses). Figure 3-11 provides each parameter's marginal posterior distributions inferred from each experiment. It is clearly seen that every experiment results in a different posterior distribution. This is due to the errors derived from both model and experiments. If the model were perfect and the parameters perfectly independent of the design parameters, all the experiments would bring a same posterior distribution. However, there are some dependencies between the parameters and the design variables, that could not be included in the model like the effect of suspending solids on the gas holdup and the reaction rates. It means that even the true values of the parameters can be varied under different conditions. In addition, the potential amount of error of each experiment would be all different. Some experiments were more sensitive to external disturbances than the others. For example, an experiment with higher solid loading has more chance to have the gas sparger clogged, or the one with lower gas volumetric flow is more susceptible to measurement errors.

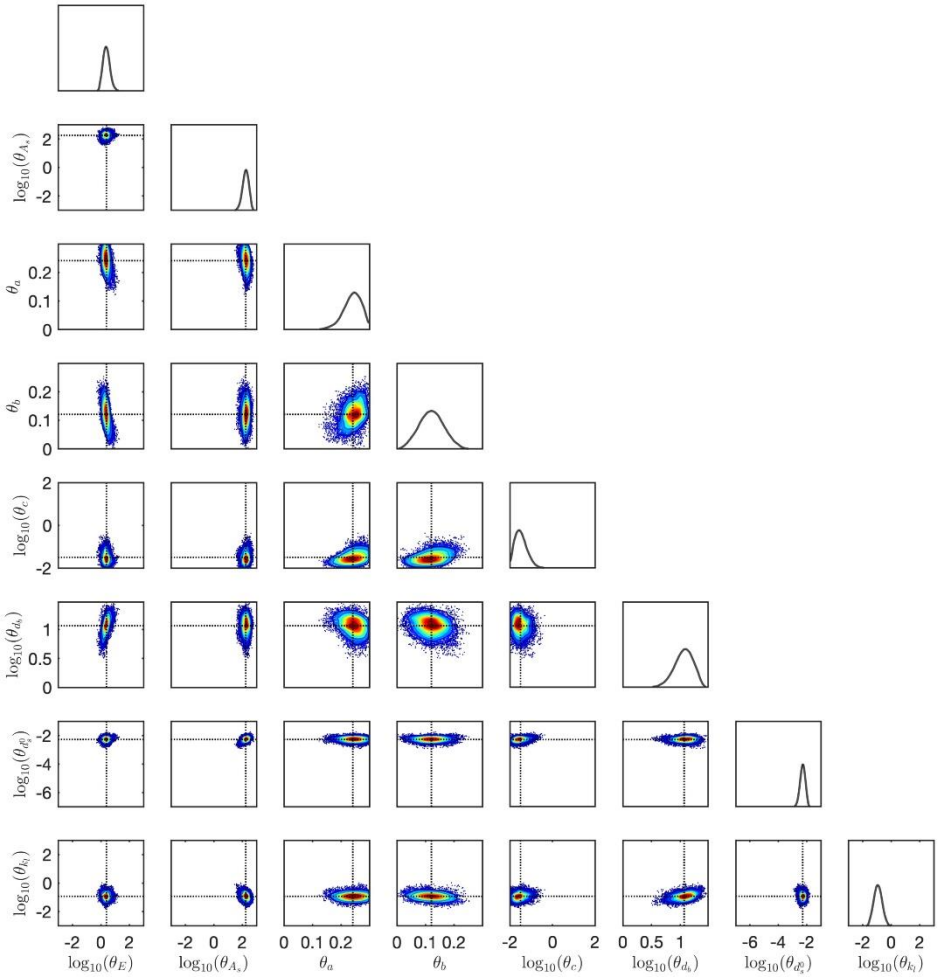

Figure 3-10. Two-dimensional joint marginal posterior distribution with20 000 final samples of MCMC. The center of dotted crosslines is θ_{mean}.

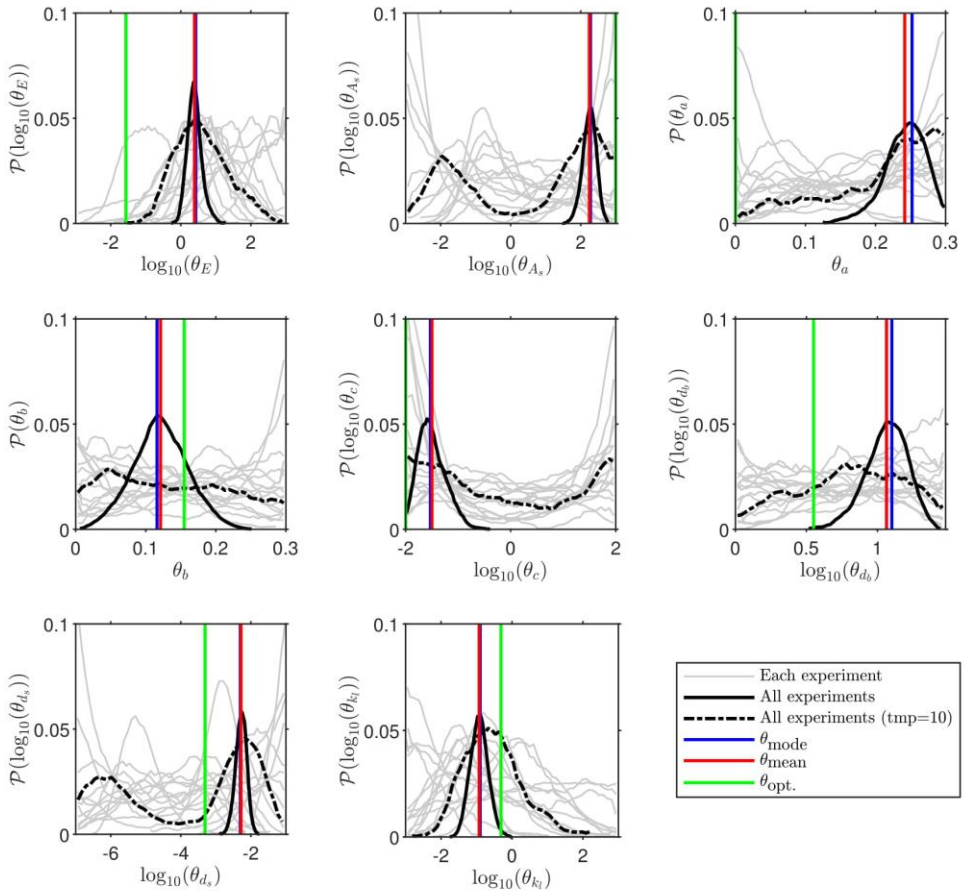

Figure 3-11. Marginal posterior distributions of each parameter from different kinds of datasets. Each gray line corresponds to the posterior which is inferred from two responses data from same experiment.

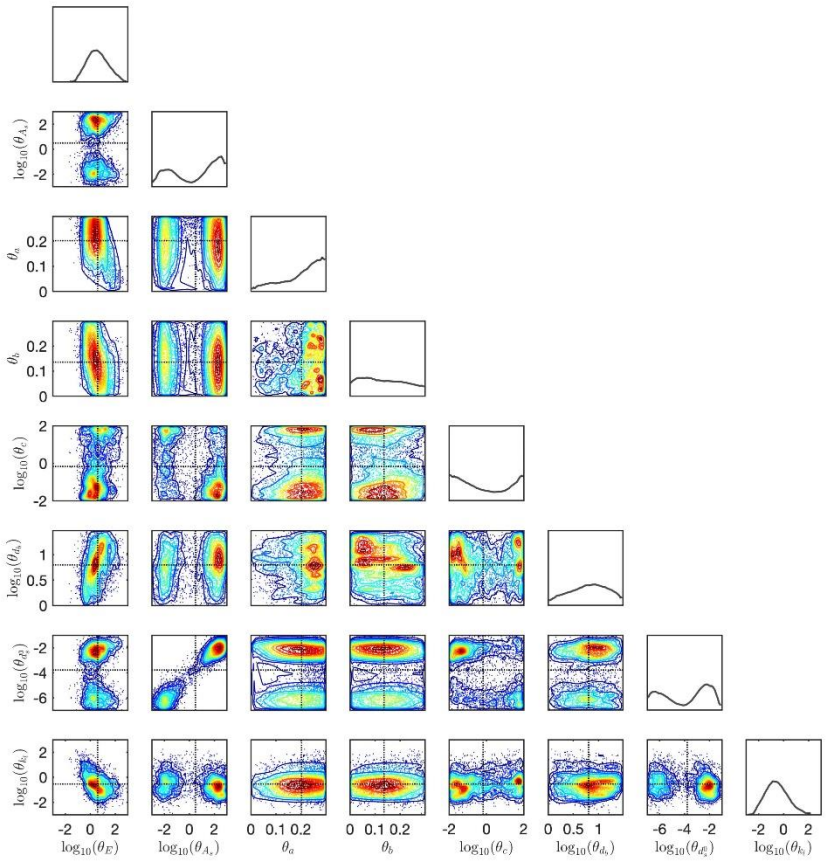

Figure 3-12. Two-dimensional joint marginal posterior distribution with tempering factor (tmp=10). The center of dotted crosslines is $\boldsymbol{\theta_{mean}}$.

When investigating characteristics of the posterior distributions in Figure 8 and Figure 9 , it is possible to categorize the parameters into three groups. The first group consists of θ_E and θ_{k_l}, whose posteriors show unimodal behavior. In this group, the posteriors inferred from all experiments are narrowed to the area where the posterior distributions from each experiment are mostly concentrated. These parameters are likely to have deterministic true values derived from physical and chemical natures of the system. For example, θ_E has a value greater than 1 because the pH could have a greater impact on the response in reality than in the model, and θ_{k_l} has a value less than 1 probably because of the existence of the suspensions which hinder the mass transfer between gas and liquid. The second group are θ_a, θ_b, θ_c and θ_{d_b} , which have broad distributions not only in the single-experiment posteriors but also in all experiments posterior. It is interesting that the bubble diameter, θ_{d_b}, turns out to show a distribution although it was regarded as a constant when the model was first designed. The third group includes θ_{A_s} and θ_{d_s}, which show multimodal behavior in their posteriors. These two parameters might have inherent multimodal natures because their posteriors from single experiments are pointing at very different values. However, the posterior from all experiments shows only one sharp peak. This is because more local peaks are observed when more data are used, but MCMC algorithm cannot easily escape from a local peak once it is trapped.

It is possible to partly explain the multimodal or broad natures of the second and third parameter groups with their many-to-one properties; multiple sets of (θ_{A_s}, θ_{d_s}) and (θ_a, θ_b, θ_c) that produce very similar results can be found. Also, the core-shell

structure of the solid particle, which is formed by the precipitation of $CaCO_3$ on the surface of $Ca(OH)_2$ [81], can be the reason as well because it must show completely different dissolution kinetics than original $Ca(OH)_2$.

However, multimodal distributions are hardly observed when multiple datasets are used for the inference. In this case, the potential existence of other local peaks can be checked by increasing the tempering factor. Sampling with a larger tempering factor means accepting worse solutions with a higher probability; graphically, it is equivalent to sampling from a flatter (or tempered) distribution than the original one which has a tempering factor of 1. Although the tempered distribution is not as same as the original distribution, it is useful when learning the overall shape of the distribution, especially when detecting small local peaks. However, the tempering factor does not affect the position of the biggest peak which has a dominant effect on the mean and mode values of the parameters. Figure 3-11 (see dashed lines) and Figure 3-12 clearly show that the increase of the tempering factor can reveal broad or multimodal natures of the posterior distributions.

For more investigations, the changes of $\boldsymbol{\theta}_{mode}$, $\boldsymbol{\theta}_{mean}$ and the joint posterior along the tempering factor increases are tracked (Figure 3-6 and Figure 3-13). $\boldsymbol{\theta}_{mode}$ shows a significant movement as no distinctive global peak exists. $\boldsymbol{\theta}_{mean}$ is close to $\boldsymbol{\theta}_{mode}$ at low tempering factors where only one peak is detected, but moves far from $\boldsymbol{\theta}_{mode}$ to middle of newly observed peaks when the tempering factor increases. $\boldsymbol{\theta}_{mode}$ would give a better fit for a specific response although it could be too sensitive sometimes, whereas $\boldsymbol{\theta}_{mean}$ would give more reasonable response when there are multiple datasets and the best parameters found out from each dataset is different.

A strong correlation is found between θ_{A_s} and θ_{d_s} from Figure 3-13. It seems like the model underestimates the solid dissolution rate when the particles are large and the other way around when the particles are small. In the case of θ_{A_s} and θ_{k_l}, there is no correlation because generally the mass transfer rate and the solid dissolution rate are not correlated.

To conclude, the proposed Bayesian estimation approach provides quantified information about uncertainties in all the parameters as well as the relations between them. This is a big advantage of this method over the optimization which can only give a deterministic value for a parameter, even when it has a multimodal or distributed characteristic.

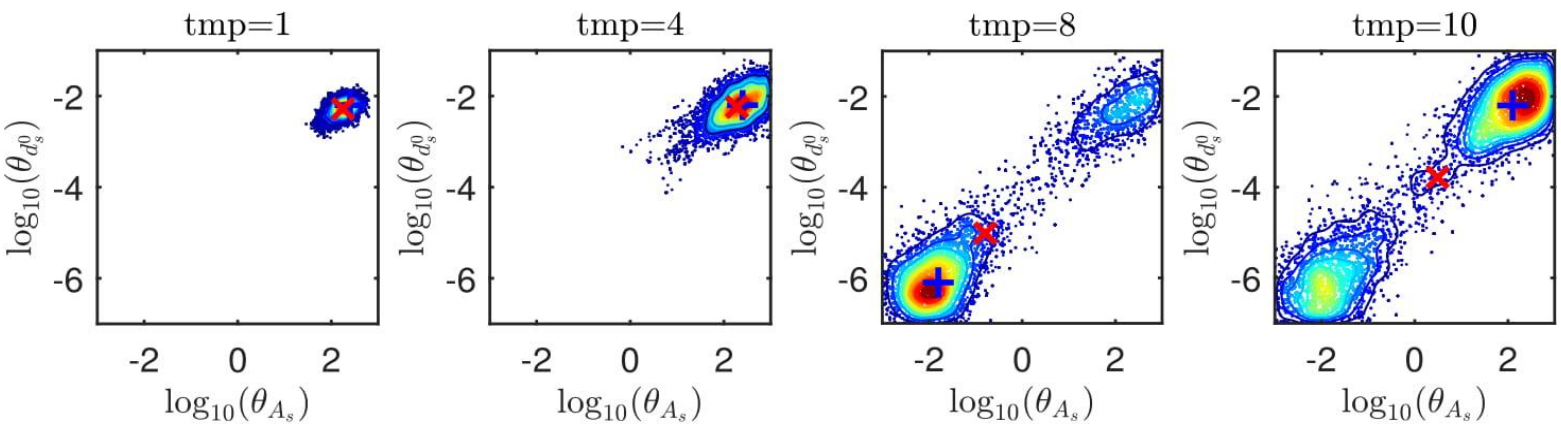

Figure 3-13. Tempering control (tempering factor as 1, 4, 8, and 10 respectively) for checking multimodal posterior distribution between θ_{A_s} and $\theta_{d_s^0}$; also compare the θ_{mean} and θ_{mode} movements. $\times$ denotes mean and $+$ denotes mode.

3.5.4. Kinetics study with the proposed model parameters

Sensitivity analysis is conducted using the inferred parameters ($\boldsymbol{\theta}_{mean}$); each design variable is perturbed at a time and the according CO_2 removal efficiency (%) $= 100 \cdot \left(\dot{n}_{CO2}^{inlet} - \dot{n}_{CO2}^{outlet}\right)/\dot{n}_{CO2}^{inlet}$ changes are observed.

As shown in Figure 3-14 , all the design variables have significant impacts on the removal efficiency. First, when the reactor temperature increases, the CO_2 removal efficiency is maintained high for longer period and the basic reactants, NaOH or $Ca(OH)_2$, are consumed earlier. It is because a high temperature can speed up the dissolution rate of $Ca(OH)_2$ as well as the enhancement factor E and the mass transfer rate through the rate constant k_{11}. Although the gas solubility, H^{CO2}, drops when the temperature becomes high, the increase in E would offset the decrease. However, it seems like that the removal efficiency no longer increases above a certain temperature as shown in the saturating profile in Figure 3-14.

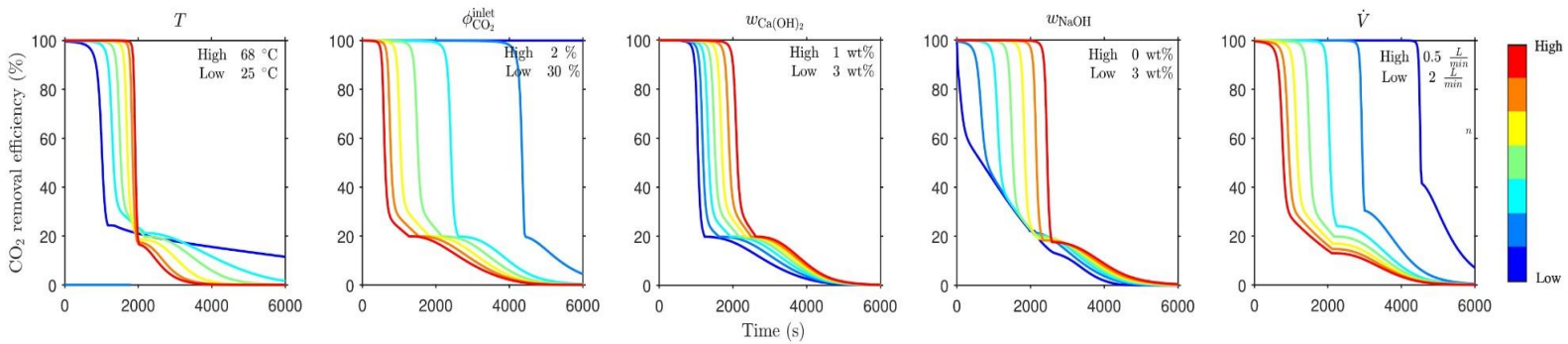

Figure 3-14. The sensitivity analysis of design variables. While one design variable is perturbed at a time within a range of the specified low and high values, the other variables are fixed to the median value of the operating range, i.e. T to 46.5 °C, ϕ_{CO2}^{inlet} to 16 %, $w_{Ca(OH)2}$ to 2 wt%, w_{NaOH} to 1.5 wt%, and $\dot{V}$ to 1.25 L/min. The perturbation is conducted to have same interval between the values.

Second, ϕ_{CO2}^{inlet} and $\dot{V}$, both of which are related to the inlet flow rate of $CO2$, have significant effects on the removal efficiency. When the inlet flow rate is low, the basic reactants, $NaOH$ or $Ca(OH)2$, are consumed slowly and the CO_2 removal efficiency stays high for longer period. However, the duration of high efficiency is not solely dependent on the inlet flow rate; CO_2 capture rate, which is closely related to the removal efficiency, decreases when ϕ_{CO2}^{inlet} or $\dot{V}$ is reduced. It is because the reduction of ϕ_{CO2}^{inlet} and $\dot{V}$ lead to the decrease of the driving force of the mass transfer (the concentration gradient between gas and liquid phase) as well as the overall gas holdup. However, although a high percentage of CO_2 removal is attained by maintaining low CO_2 inlet flowrate, the absolute amount of captured CO_2 capture would be low as well.

Third, the increase of $w_{Ca(OH)2}$ shows an obvious effect on the removal efficiency profile. It helps to prolong the active CO_2 capture period. However, in reality, it must be considered that a large loading of $Ca(OH)_2$ could harm the mechanical operation such as impeller rotation or gas distribution. The increase of w_{NaOH} also has similar effects unless NaOH does not exist at all. (See the dark line in the fourth plot of Figure 3-14). In the absence of NaOH, the solution cannot completely remove the CO_2 coming into the reactor. It is because the dissolution rate of $Ca(OH)_2$ is much slower than NaOH to catch the CO_2's consumption of OH^- ion.

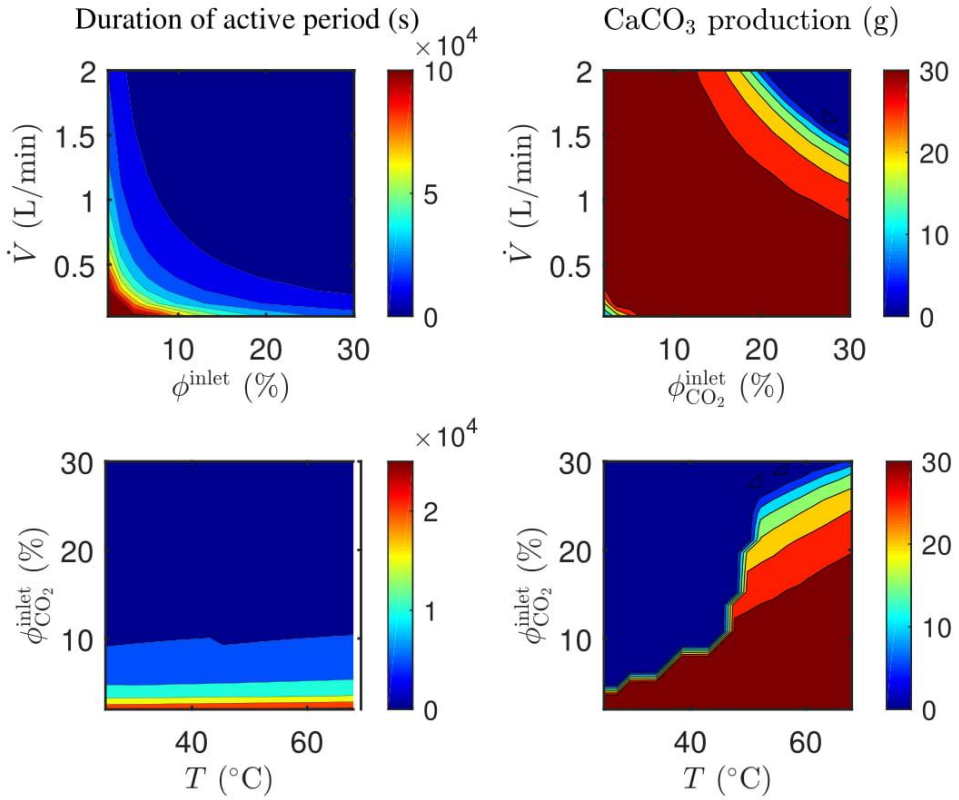

Figure 3-15. The case study results using the estimated parameter values.

Another analysis is provided here using the obtained kinetics. In real applications, the successful operation of the process would be evaluated by how long the high removal efficiency is maintained in a single batch when fixed amount of basic materials are given and how much CO_2 is captured during that time. The latter can be evaluated by how much $CaCO_3$ is produced as well. Here two case studies, in which how they are affected by (ϕ_{CO2}^{inlet}, $\dot{V}$) and (T, ϕ_{CO2}^{inlet}), are done (Figure 3-15). In the former case, it is shown that the duration of active period increases as both design variables decrease, whereas the $CaCO_3$ production is high at the middle of the ranges. It seems like that the southwest end region in the right upper plot of Figure 3-15 represents the best operating conditions. In case of (T, ϕ_{CO2}^{inlet}), the region with dark red color in both left lower and right lower graphs, could be regarded as the best. It is expected that further uncertainty analysis using uncertainty propagation techniques such as PCE, which could be one of the future studies, can help deriving more robust operating conditions.

3.6. Conclusions

This chapter presented a mathematical model for aqueous mineral carbonation process for CCU. The model describes gas-liquid mass transfer, solid dissolutions, ionic reactions and precipitation kinetics in differential algebraic equations. Eight parameters are inserted in the parts where the model seems to have uncertainties. 17 sets of experiments were carried out under different conditions including one for the result validation and monitored two responses, outlet CO_2 fraction and pH of the

solution, in each experiment. The data from the experiments were used to estimate the posterior distributions of the parameters using Bayesian parameter estimation framework.

The purpose of the Bayesian parameter estimation is to find the posterior distribution of each parameter. The posterior is defined by the product of the prior distribution of the parameter and the likelihood of data, but MCMC sampling method is necessary because the algebraic formulation of the posterior with respect to θ is unattainable. For the prior, uniform distribution was adopted and for the likelihood, Gaussian error assumption in which iterative samplings were used to estimate the covariance vector of Gaussian error is used.

As a result, the stochastic model responses which fit the experimental measurements very well are obtained. It shows that the proposed model and the parameter estimation method were capable of capturing the important features of the mineral carbonation reactor. Some of the parameters were revealed to have multimodal or distributed natures, although they were not designed to have deterministic values in the model development stage. It shows that a deterministic model can be extended to a stochastic model through Bayesian inference.

Based on the obtained parameter estimates, a rigorous analysis on the effect of each design variable on the reactor's performance such as CO_2 removal efficiency and the production of $CaCO_3$ was done. This can be useful information for operating the mineral carbonation process.

This methodology would be useful for the parameter estimation problems which have non-ideal or hard-to-predict behaviors in systems. If model errors are not fully

unavoidable, it is good to keep the uncertainties with the model for follwing applications. There is a distributed toolbox based on this chapter's contents (https://github.com/jihyunbak/BayesChemEng) with an end-to-end pipeline from creating surrogate models for dynamic responses through inferencing posterior distributions using MCMC to analyzing results with plotting tools. It can be applied in other fields which requires a stochastic model to quantify uncertainties in the output response, such as robust design, stochastic optimal control, and model-based design of experiments.

Chapter 4.

Multi-objective optimization of chemical reactor design using computational fluid dynamics[†]

4.1. Objective

In this chapter, a CFD-based design optimizer for chemical reactors based on the multi-objective Bayesian optimization framework is proposed. This optimizer is applied to the design of a gas-sparged stirred tank reactor with dual Rushton turbines, which are widely used in many applications such as bio-hydration processes. Two objective functions are the effective gas holdup and the power consumption and six optimization variables are the design parameters related to the shape of the tank, the position and size of impellers and gas sparger, and the topological constraints. As a result, a saturated Pareto front is obtained within 100 iterations, which include ten initial cases drawn from a Latin hypercube, and ten constraint violation cases. The designs included in the saturated Pareto front outperform the heuristic designs reported in the literature. A platform to automate the optimal design process by connecting the multi-objective BO (MBO) with commercial CFD software.

[†] This chapter cites the author's published journal article: Park, S., Na, J., Kim, M., & Lee, J. (2018). Multi-objective Bayesian optimization of chemical reactor design using computational fluid dynamics. Computers & Chemical Engineering, 119, 25-37.

4.2. Problem Formulation

In this chapter, the multi-objective optimal design problem to maximize the effective gas holdup (*egh*) and minimize the power consumption (*power*) of a gas-sparged stirred tank reactor with two Rushton turbines and four baffles is solved. Figure 4-1 (a) shows an illustration of the general design of this reactor type.

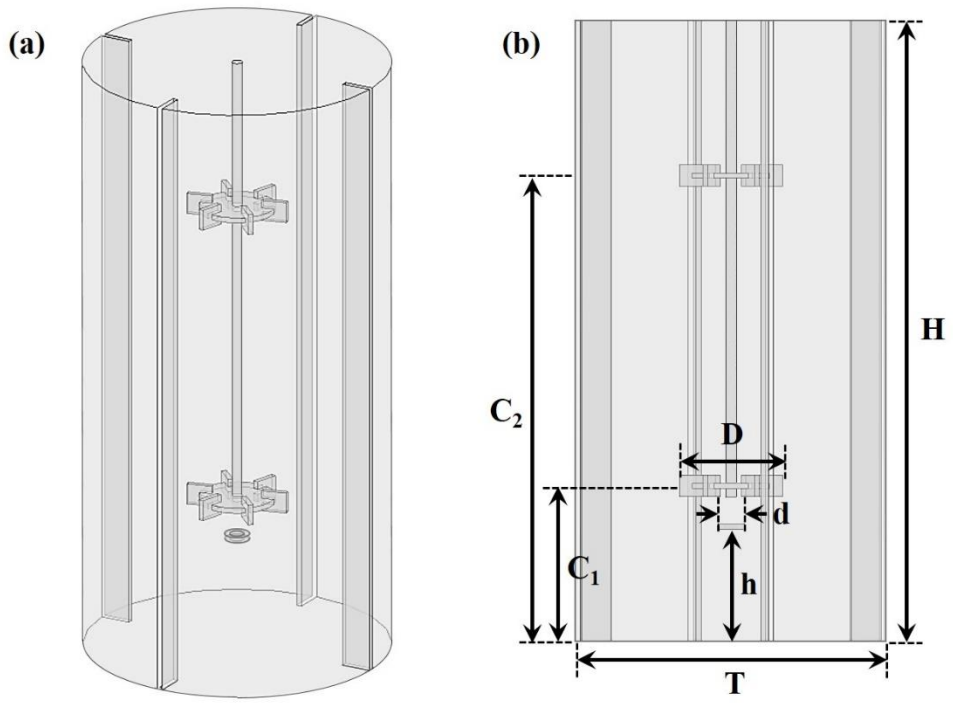

Figure 4-1. (a) Base design of a gas-sparged stirred tank reactor and (b) design parameters of the reactor.

The concept of an effective gas holdup is slightly different from a typical gas holdup in that it only calculates the gas fraction where the volume fraction of gas is below 0.3 [110]. It is introduced to penalize the excessive accumulation of gas [43] and prevent a reactor with an extreme gas flow in only one region to become optimal. A higher value of the effective gas holdup means the impellers distribute more gas throughout the reactor. The power consumption is the amount of energy consumed by the impellers per unit of time. A lower power consumption is desirable to lower the operating costs of the reactor.

The structure of the reactor can be determined through the following parameters, as illustrated in Figure 4-1 (b): the tank diameter (*T*), tank height (*H*), clearance of the lower and upper impellers (C_1, C_2), diameter of the impeller (*D*), and diameter (*d*) and height (*h*) of the sparger. When the volume of the reactor is fixed, which is a reasonable assumption in this type of reactor in which the required amount of reagent is calculated at a higher decision level, the number of parameters is reduced to six: the tank aspect ratio ($\frac{H}{T}$), the lower impeller clearance to the tank height ratio ($\frac{C_1}{H}$), the upper impeller clearance to the tank height ratio ($\frac{C_2}{H}$), the sparger diameter to the impeller diameter ratio ($\frac{\mathrm{d}}{\mathrm{D}}$), the impeller diameter to the tank diameter ratio ($\frac{D}{T}$), and the sparger height to the lower impeller clearance ratio ($\frac{h}{C_1}$). The type of the impeller is fixed to a Rushton turbine because this is the most accepted type for a gas distribution, and assumed that the tank is fully baffled.

The optimization problem is mathematically formulated as

$$\min\left(\mathrm{f}_1(\boldsymbol{x}), \mathrm{f}_2(\boldsymbol{x})\right)$$

$$\text{where} \quad \mathrm{f}_1(\boldsymbol{x}) = power(\boldsymbol{x})[\mathrm{W}]^{0.4}$$

$$\mathrm{f}_2(\boldsymbol{x}) = (20 - egh(\boldsymbol{x}))[\%],$$

$$\boldsymbol{x} = \left[\frac{H}{T}, \frac{C_1}{H}, \frac{C_2}{H}, \frac{d}{D}, \frac{D}{T}, \frac{h}{C_1}\right] \in \mathrm{X},$$

$$\mathrm{X} = \left\{ \boldsymbol{x} = \left[\frac{H}{T}, \frac{C_1}{H}, \frac{C_2}{H}, \frac{d}{D}, \frac{D}{T}, \frac{h}{C_1}\right] \middle| \, \boldsymbol{x} \in \mathbb{D}^6, \right.$$

$$\frac{H}{T} \in \{1, 1.5, 2, 2.5, 3\},$$

$$\frac{C_1}{H} \in \{0.1, 0.2, 0.3, 0.4, 0.5\},$$

$$\frac{C_2}{H} \in \{0.5, 0.6, 0.7, 0.8, 0.9\},$$

$$\frac{d}{D} \in \{0.25, 0.5, 0.75, 1, 1.25\},$$

$$\frac{D}{T} \in \{0.25, 0.333, 0.417, 0.5, 0.583\},$$

$$\left.\frac{h}{C_1} \in \{0.5, 0.6, 0.7, 0.8, 0.9\} \right\},$$

Eq. 4-1

$$\mathbf{s.t.}\ \boldsymbol{x} \text{ comprises the topologically available reactor.}$$

In Eq. 4-1, the optimization variable $\boldsymbol{x}$ is a vector of six discrete design parameters. Functions f_1 and f_2 are objective functions whose forms are variations in the performance functions, $power(\boldsymbol{x})$ and $egh(\boldsymbol{x})$. The performance function maps the specific design defined through a set of design parameters to a performance indicator. Here, X is the search domain or design space of a reactor in which each point corresponds to a different design.

Here, the design space is a discrete space of six dimensions, $\mathbb{D}^6$. Each design parameter constitutes one axis in the design space, and can have five values with a

constant grid spacing. Thus, $5^6 = 15{,}625$ grid points exist in the design space of a hyper-rectangle shape. However, not every combination of design parameter values comprises a topologically feasible reactor structure. For example, if both $\frac{C_1}{H}$ and $\frac{C_2}{H}$ have the same value of 0.5, two impellers overlap. The designs that do not violate the topological constraints are 8,655 in number.

Regarding the objective functions, the performance functions, $power(\mathbf{x})$ and $egh(\mathbf{x})$, are reformulated to $power(\mathbf{x})^{0.4}$ and $20 - egh(\mathbf{x})$, respectively. The former is to scale the power consumption, which has a much broader range compared to the effective gas holdup, and the latter is to convert a maximization problem into a minimization problem. The important fact of these performance functions is that they are black-box functions, which cannot be described in algebraic form; their values can be determined only through a CFD simulation, as illustrated in Figure 4-2.

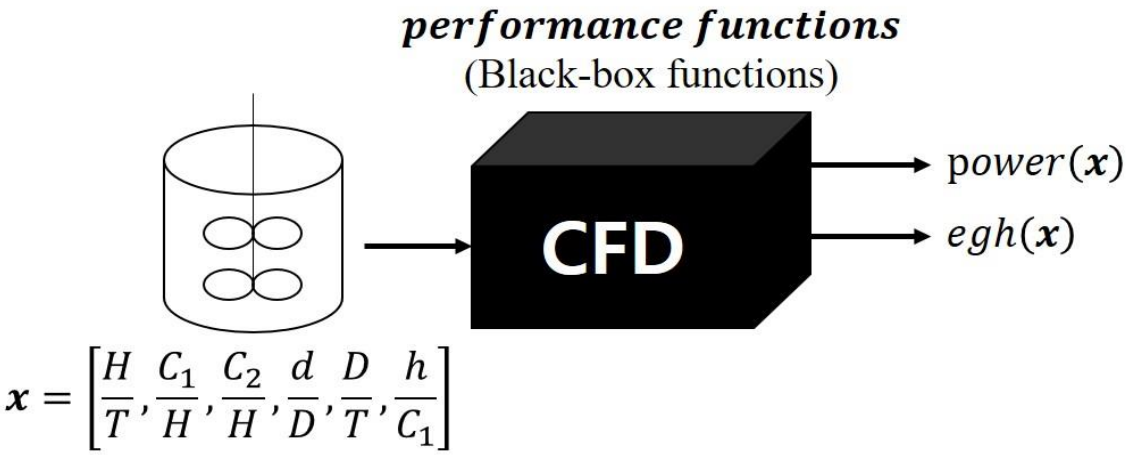

Figure 4-2. Graphical illustration of the role of CFD as black-box performance functions.

The final purpose of a general multi-objective optimization problem is to find the Pareto set that satisfies the following:

$$S = \{ \boldsymbol{s} \in Y: \nexists \boldsymbol{s}' \in Y \; such \; that \; f(\boldsymbol{s}') \prec f(\boldsymbol{s})\}, \quad \text{Eq. 4-2}$$

where $f = [f_1, f_2]$, Y is the image of f, and $\prec$ indicates the Pareto domination rule, which is defined as

$$\boldsymbol{a} = [a_1, \dots, a_p] \prec \boldsymbol{b} = [b_1, \dots, b_p] \Leftrightarrow \begin{array}{l} \forall i \leq p, \;\; a_i \leq b_i \,, \\ \exists j \leq p, \;\; a_i < b_i \,. \end{array} \quad \text{Eq. 4-3}$$

However, in this study, the final Pareto front is likely to be sub-optimal because of sampling inputs in a continuous space. The resulting optimization variables have only five discrete values because saving computational time is preferable to finding a global optimum in practical applications.

4.3. Optimization scheme

4.3.1. Multi-objective optimization algorithm

BO is a branch of nonlinear optimization in which a sampling for the unknown objective function occurs at every iteration based on the analysis of a stochastic process surrogate model [111]. There are many variations depending on which type of stochastic process and sampling criterion are used. The Gaussian process (GP) is the most widely accepted surrogate model, whereas different sampling criteria are applied for different problems.

Table 4-1 describes a general algorithm of single-objective BO, adopted from

Brochu et al. [112]. The process of determining a new sampling point $\boldsymbol{x}_n$, evaluating an objective function at $\boldsymbol{x}_n$, and updating the surrogate model with the newly added sample $(\boldsymbol{x}_n, \mathrm{y_n})$ is repeated every iteration until the stopping criterion is met. The acquisition function plays a role as a sampling criterion. It instructs us how much each point in the search domain is worth sampling by calculating the probability of the objective function to reach the maximum (or minimum) at the point of interest.

Table 4-1. Pseudo code for general Bayesian optimization concept [112].

Algorithm Bayesian Optimization

1: **for** n = 1,2,… **do**

2: Find $\boldsymbol{x}_n$ that maximizes the acquisition function over the GP:

$$\boldsymbol{x}_n = argmax_{\boldsymbol{x}}\, \mathrm{u}(\boldsymbol{x}|\mathcal{D}_{1:t-1})$$

3: Evaluate the objective function:

$$\mathrm{y_t} = \mathrm{f}(\boldsymbol{x_n})$$

4: Augment the sample as $\mathcal{D}_{1:n} = \{\mathcal{D}_{1:n-1}, (\boldsymbol{x}_n, \mathrm{y_n})\}$ and update the GP.

5: **end for**

Here, $\mathrm{u}(\boldsymbol{x})$ is the acquisition function, $\mathrm{f}(\boldsymbol{x})$ is the function to be optimized, and $\mathcal{D}_{1:\mathrm{n}}$ is the observed dataset from iteration 1 ton.

The use of the GP as a surrogate model makes the probability calculations easy to conduct. The key principle of the GP is that any finite linear combination of the function values has a joint Gaussian distribution. Thus, with the GP, when there are N sample points at $\boldsymbol{x_1}, \dots, \boldsymbol{x_N}$, their function values, $\mathrm{f}(\boldsymbol{x_1}) \dots \mathrm{f}(\boldsymbol{x_N})$, are in a multivariate Gaussian distribution whose mean and covariance matrix are expressed as functions of the input $\boldsymbol{x_1}, \dots, \boldsymbol{x_N}$:

$$\mathrm{f}_{1:\mathrm{N}} \sim \mathcal{N}\left(\mathrm{m}_{1:\mathrm{N}}, \mathbf{K}\right), \qquad \text{Eq. 4-4}$$

where $\mathrm{f}_{1:\mathrm{N}} \equiv (\mathrm{f}(\boldsymbol{x_1}) \dots \mathrm{f}(\boldsymbol{x_N}))^{\mathrm{T}}$, $\mathrm{m}_{1:\mathrm{N}} \equiv (\mathrm{m}(\boldsymbol{x_1}) \dots \mathrm{m}(\boldsymbol{x_N}))^{\mathrm{T}}$, and $\mathbf{K}_{ij} = \mathrm{k}(\boldsymbol{x_i}, \boldsymbol{x_j})$. The mean function, $\mathrm{m}(\boldsymbol{x})$, is usually set to a zero function, whereas the covariance kernel function, $\mathrm{k}(\boldsymbol{x_i}, \boldsymbol{x_j})$, has many different forms. The covariance kernel functions provide a prior belief on the attributes of an objective function, such as the smoothness, periodicity, or oscillatory behaviors. As an example, Isotropic Matérn 5/2 kernel applied in CFD-MBO optimizer is given:

$$\mathrm{k}(\boldsymbol{x_i}, \boldsymbol{x_j}) = \sigma_f{}^2 \left(1 + \frac{\sqrt{10}r}{\rho} + \frac{10r^2}{3\rho^2}\right) \exp\left(-\frac{\sqrt{10}r}{\rho}\right), \qquad \text{Eq. 4-5}$$

where σ_f and ρ are the hyper-parameters, and $r = \sqrt{(\boldsymbol{x_i} - \boldsymbol{x_j})^{\mathrm{T}}(\boldsymbol{x_i} - \boldsymbol{x_j})}$. The formulation in (5) implicates that the closer the distance is between two points in the input space, the stronger the correlation between their function values. Two hyperparameters, σ_f and ρ, are used to fine-tune the model shape.

The prediction of the unknown function value at point $\boldsymbol{x}_*$ is conducted using a

property in which $f_{1:N}$ and $f(\boldsymbol{x}_*)$ also have a joint Gaussian distribution:

$$\begin{pmatrix} f_{1:N} \\ f_* \end{pmatrix} \sim \mathcal{N}\left(\begin{pmatrix} m_{1:N} \\ m_* \end{pmatrix}, \begin{pmatrix} \mathbf{K} & \mathbf{K}_* \\ \mathbf{K}_*{}^{\mathrm{T}} & \mathbf{K}_{**} \end{pmatrix} \right) \quad \text{Eq. 4-6}$$

where $f_* = f(\boldsymbol{x}_*)$, $m_* = m(\boldsymbol{x}_*)$, $\mathbf{K}_* \equiv (k(\boldsymbol{x_1}, \boldsymbol{x}_*) \ldots k(\mathbf{x_N}, \mathbf{x}_*))^{\mathrm{T}}$, and $\mathbf{K}_{**} = k(\boldsymbol{x}_*, \boldsymbol{x}_*)$. The probability distribution of f_* conditioned upon $f_{1:N}$ data is given in a closed form using the Bayes rule:

$$p(f_* | \boldsymbol{x}_*, \boldsymbol{x}_{1:N}, f_{1:N}) = \mathcal{N}(\mu_*, \sigma_*^2) \quad \text{Eq. 4-7}$$

where $\mu_* = m(\boldsymbol{x}_*) + \mathbf{K}_*{}^{\mathrm{T}} \mathbf{K}^{-1} (f_{1:N} - m_{1:N})$, and $\sigma_*^2 = \mathbf{K}_{**} - \mathbf{K}_*{}^{\mathrm{T}} \mathbf{K}^{-1} \mathbf{K}_*$.

Given the exact probability distribution, the acquisition function can compute the likeliness of $\boldsymbol{x}_*$ as the optimum. One of the widely used acquisition functions is the expected improvement (EI), u_{EI} [113], which evaluates the expected improvement over the incumbent minimum (assuming the minimization problem), where improvement I is defined as follows:

$$I(f(\boldsymbol{x}_*)) \equiv (\min(f_{1:N}) - f(\boldsymbol{x}_*)) \cdot \mathbf{1}_{[\min(f_{1:N}) > f(\boldsymbol{x}_*)]}, \quad \text{Eq. 4-8}$$

where $\mathbf{1}_{[E]}$ is the indicator function, which has a value of 1 if E is true and 0 if it is false. Because $f(\boldsymbol{x}_*)$ follows a Gaussian distribution, u_{EI} is expressed in a closed form as

$$\begin{aligned} u_{EI}(\boldsymbol{x}_*) &\equiv \mathbb{E}\left[I\left(f(\boldsymbol{x}_*)\right)\right] \\ &= \left(\min(f_{1:N}) - \mu_*\right) \Phi\left(\frac{\min(f_{1:N}) - \mu_*}{\sigma_*}\right) \\ &+ \sigma_* \phi\left(\frac{\min(f_{1:N}) - \mu_*}{\sigma_*}\right), \end{aligned} \quad \text{Eq. 4-9}$$

where $\mathbb{E}[\cdot]$ is the expected value, and $\Phi(\cdot)$ and $\phi(\cdot)$ are the cumulative distribution function and probability density function of a standard normal distribution, respectively. Figure 4-3 shows the concept of the EI as a graph.

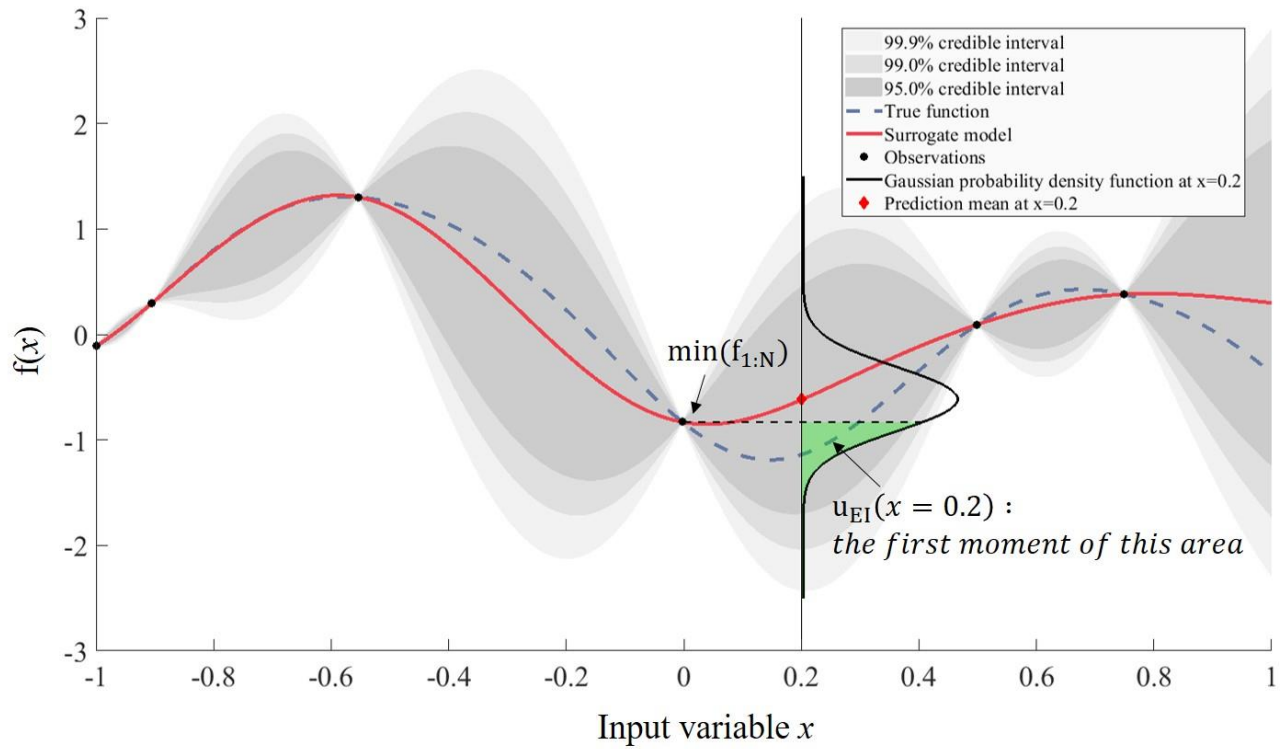

Figure 4-3. Graphical illustration of EI.

The extension to the multi-objective optimization is achieved by introducing different acquisition functions. One of the acquisition functions developed for multiple objectives is the expected maximin improvement (EMmi) function, u_{EMmi} [114], which was applied in this work. The EMmi function is used to compute the expected value of the maximin improvement I_M, which is defined as

$$\begin{aligned} & I_M\left(f(\boldsymbol{x}_*)\right) \\ & \equiv -\max_{\boldsymbol{x_i} \in \mathcal{P}_x} \min_{j = 1,2,\ldots} \left(f_j(\boldsymbol{x}_*) - f_j(\boldsymbol{x_i})\right) \\ & \times \mathbf{1}_{\left[-\max_{\mathbf{x_i} \in \mathcal{P}_x} \min_{j=1,2,\ldots} \left(f_j(\boldsymbol{x}_*) - f_j(\boldsymbol{x_i})\right) > 0\right]}, \end{aligned} \qquad \text{Eq. 4-10}$$

where $\mathcal{P}_x$ is the incumbent Pareto set configured until that point, and the maximum value of j represents the number of objective functions. Here, I_M measures how much a new point will be distant from the incumbent Pareto front in an objective space. However, unlike a single-objective case, u_{EMmi} does not exist in an analytic formulation, and thus numerical methods such as Monte Carlo sampling are needed to calculate its values.

4.3.2. CFD-MBO optimizer

CFD-MBO optimizer is developed to optimize the reactor performances, which can only be evaluated through expensive CFD simulations. The multi-objective BO algorithm and a CFD platform are connected and thus, the entire process is completely automated. In this section, the detailed algorithms and implementation methods of the optimizer are described.

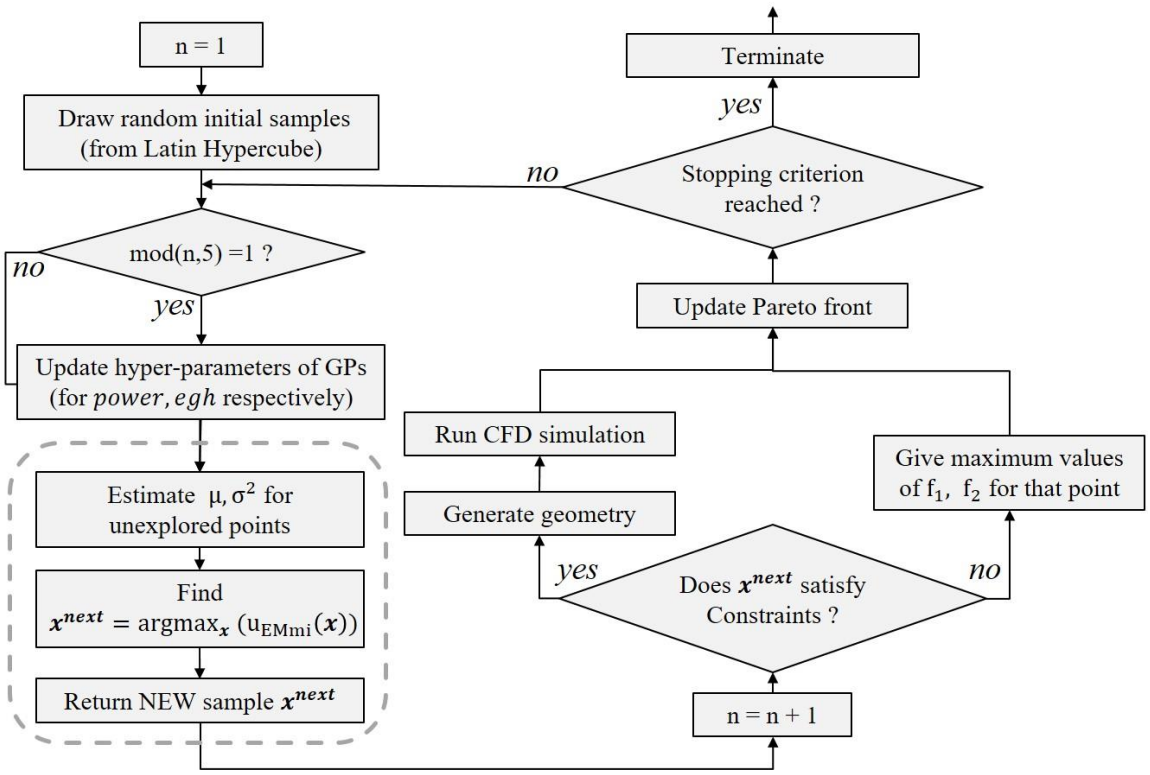

Figure 4-4. Algorithm of CFD-MBO optimizer.

The flow chart in Figure 4-4 shows the algorithm of the CFD-MBO optimizer. The first task of the optimizer is to sample an initial training set using the Latin Hypercube sampling method. Herein, the number of initial samples is ten, although this number is adjustable depending on the available computational resources. Then, surrogate models, two GPs with zero mean function and Isotropic Matérn 5/2 covariance kernel, are created for both objective functions based on the initial data. The hyperparameters of the kernel, σ_f and ρ, are optimized every fifth iteration using the restricted maximum likelihood method to best fit the sampled data.

At every iteration, the mean and variance of the objective function values are estimated at all points in the input domain. The acquisition function, $\mathrm{u_{EMmi}}$, is then computed using the Monte Carlo method. The optimizer samples 20,000 random pairs of objective function values from the posterior Gaussian distributions, calculates the maximin improvement of each sample, and then approximates the expected values by taking their averages. Although finding the argmax value of an acquisition function is generally another optimization problem, this work adopted an exhaustive searching method owing to the relatively small number of grid points in the search domain.

Once the next sampling point is determined, the optimizer first judges whether the topological constraints are satisfied in this new design. When all constraints are satisfied, it automatically generates the geometry and mesh files for a CFD simulation by launching the Workbench program of Ansys©, and executes the CFX© solver. However, when there is a constraint violation, which means that the design

parameters of the new sampling point do not form a feasible structure, the optimizer allocates the maximum values for both objective functions without a CFD simulation. After the simulation, the performance indicators, namely, the effective gas holdup and power consumption, are extracted from the CFD result file, and then the Pareto front is updated with the new result.

The stopping criterion is the exhaustion of the time budgets or the saturation of the Pareto front. Whether the Pareto front is saturated is determined based on two criteria: the hypervolume of the dominated area in the output space, and the average u_{EMmi} value of all points in the input space. These can give both quantitative and qualitative information to stop the iterations. More discussions on these are provided in the following section.

The CFD-MBO optimizer is built using Ansys CFX and the MATLAB-based open toolbox STK, version 2.5.0 [115]. Ansys Workbench provides tools for drawing a geometry, generating a mesh from the geometry, running CFD simulations using the CFX solver, and post-processing the CFD results. STK provides various source codes required to implement the MBO algorithms, such as GP regression codes, acquisition function codes, and a Pareto front finding code. Ansys software can be executed without a graphical user interface by running pre-built command files, called journal or session files, which are written in Python, Perl, or Ansys's own language depending on the tools. The CFD-MBO optimizer creates command files that contain the geometry information of new reactor design and then runs the CFD simulation using these files. Figure 4-5 illustrates the detailed work flow of the optimizer. The overall framework including MBO is implemented in MATLAB.

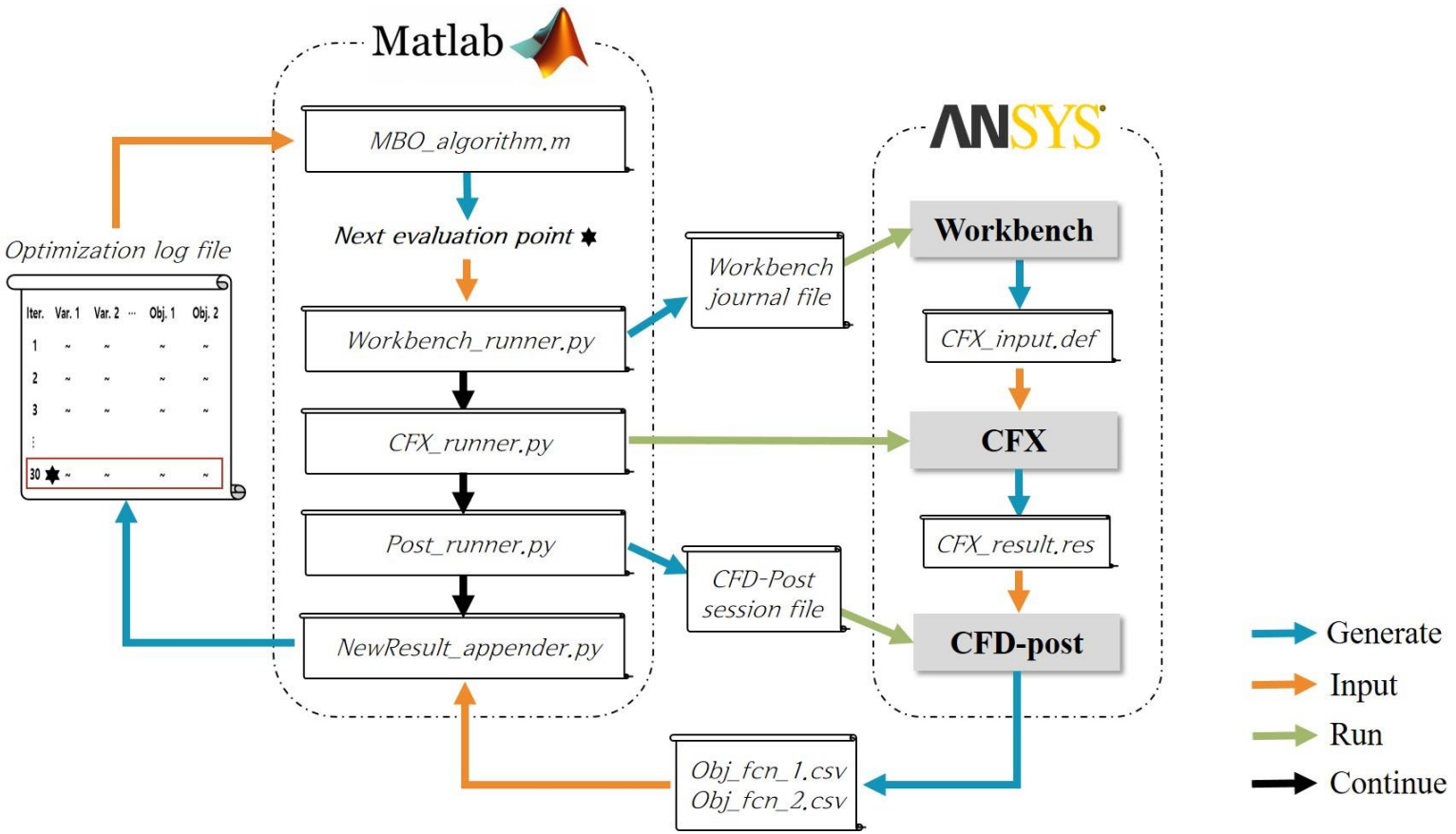

Figure 4-5. Implementation of CFD-MBO optimizer using STK toolbox, MATLAB, and Ansys software.

4.4. CFD modeling

This section provides the modeling method of a gas-sparged stirred tank reactor using CFD. The reactor of Alves et al. [75], which includes measurement data of a local and global gas holdup and the design variables falling within the range of this problem, was chosen as a reference. Because it is impossible to validate all results during the optimization, the CFD setting that best fits the experimental results [75] was found first, and then maintained for the remaining iterations. For many aspects, the work of Kerdouss et al. [116], who conducted the CFD simulation of the same reactor was referred.

4.4.1. Tank specifications

Figure 4-1 depicts the exact reactor used in validation. It is a flat-bottomed and fully baffled tank, which has a diameter of 0.292 m and a height of 0.584 m. Two standard Rushton turbines are installed and rotated at a speed of 450 rpm. Water at 25°C is filled into the reactor, and the air under ambient conditions is sparged from the ring sparger at a rate of 1.67×10^{-4} m^3/s.

4.4.2. Governing equations

To model the two-phase flow, Eulerian–Eulerian approach, which describes the gas and liquid as interpenetrating continua and solves the Reynolds averaged mass and momentum conservation equations for each phase, is used. To describe the rotation of impellers, multiple reference frame (MRF) method is applied. The governing equations are described as

$$\frac{\partial}{\partial t}(\epsilon_i \rho_i) + \nabla \cdot (\epsilon_i \rho_i \vec{u}_i) = 0, \qquad where\ i = g, l \qquad \text{Eq. 4-11}$$

$$\epsilon_g + \epsilon_l = 1, \qquad \text{Eq. 4-12}$$

$$\frac{\partial}{\partial t}(\epsilon_i \rho_i \vec{u}_i) + \nabla \cdot (\epsilon_i \rho_i \vec{u}_i \vec{u}_i)$$
$$= -\epsilon_i \nabla P + \nabla \cdot \left(\epsilon_i \mu_{eff,i} (\nabla \vec{u}_i + (\nabla \vec{u}_i)^T)\right) + \epsilon_i \rho_i \vec{g} \qquad \text{Eq. 4-13}$$
$$+ \vec{F}_i + \vec{B}_i + S_i \vec{u}_i,$$

$$\vec{B}_i = -2\epsilon_i \rho_i \vec{N} \times \vec{u}_i - \epsilon_i \rho_i \vec{N} \times (\vec{N} \times \vec{r}). \qquad \text{Eq. 4-14}$$

The term S_i is applied at the gas sparger (gas inlet) and liquid surface (gas outlet) as the mass sink and source, respectively. In addition, $\vec{F}_i$ is a generalized term for the interphase forces, and $\vec{B}_i$ corresponds to Coriolis and centrifugal forces applied to the rotating reference frame.

Interaction forces such as the drag force, lift force, and virtual mass force are exerted between the gas and liquid phases. However, it was reported that only the drag force has a critical impact on the flow pattern in a stirred tank [117, 118]. Therefore, in this work, $\vec{F}_i$ is reduced to account for only the drag force:

$$\vec{F}_l = -\vec{F}_g = \frac{3}{4} C_D \frac{\epsilon_l \epsilon_g \rho_l}{d_b} |\vec{u}_g - \vec{u}_l| (\vec{u}_g - \vec{u}_l). \qquad \text{Eq. 4-15}$$

$$C_D = \begin{cases} \dfrac{24(1 + 0.15 {Re_p}^{0.687})}{Re_p} & Re_p \leq 1000 \\ 0.44 & Re_p > 1000 \end{cases}. \qquad \text{Eq. 4-16}$$

$$Re_p = \frac{\rho_l |\vec{u}_g - \vec{u}_l| d_b}{\mu_l + C\mu_{t,l}}. \qquad \text{Eq. 4-17}$$

The bubble diameter, d_b, was assumed to have a constant value of 3 mm based on

the research by [75], in which the bubble diameter was within the range of 1–5 mm. For the drag coefficient, the correlation of Schiller and Naumann [119], which describes particles in a stagnant liquid, was implemented as a basic form, and modified viscosity term in Eq. 4-17 to consider the turbulence effect in the stirred tank [120] was added. The parameter C in Eq. 4-17 is introduced into the turbulence effect, and is set to 0.9.

Standard k-epsilon model and the dispersed phase zero equation were used to describe the turbulence behavior of the liquid and the gas phase, respectively. However, this model has a weakness in reproducing the hydrodynamics of the near-wall regions. Therefore, to compensate this weakness as well as to avoid a violation of the recommended Y^+ range, a scalable wall function, which virtually displaces the near-wall mesh to have a Y^+ value of 11.225, is applied before applying the wall function. The scalable wall function is useful in industrial applications, in which Y^+ values vary considerably in a single unit, and makes the results independent of the range of their values.

4.4.3. Simulation methods

The commercial software ANSYS CFX, Release 17.0, is used for the transient simulation. The time step is set to 0.02 s at the initialization stage, and increased to 0.04 s after the calculation is stabilized. Although these time step sizes seem to be large, it is ascertained that the results were not different to a test case in which the time step was set to 0.001 s. To boost the speed of the simulations, only one half of the reactor was simulated, and the rotational symmetry was applied on the other half.

The number of mesh elements is 306,943, which is maintained at a similar level during the rest of the optimization. No-slip and free-slip boundary conditions are applied in all walls for the liquid and gas phases, respectively. For the advection scheme, a high-resolution method, in which the first- and second-order advection schemes are blended with different blending factors for different locations, is used, and for the transient scheme, the second-order backward Euler method is used. For the turbulence numeric, a first-order upwind advection scheme is used.

The effective gas holdup and power consumption values are obtained after reaching the steady-state by taking the average values of the transient data. It takes about 3 h with 16 CPU cores to earn a sufficient amount of steady-state data. The computational times required for other designs are also similar.

4.5. Results and discussion

4.5.1. CFD model validation

The simulation results were compared with the previously reported experimental data on the gas holdup by Alves et al. [75]. Figure 4-6 shows the local gas holdup trends along the radial and axial positions of the CFD simulations and experiments. The simulation data are not constant, but change over time. Thus, they are represented with the mean and $\pm 1\sigma$ range of the time-series data. There are no significant discrepancies in the values or tendencies except for the region near the outer liquid surface. The global gas holdup also agrees well with the actual value. The CFD model and the experiment provide values of 2.4% and 2.5%, respectively.

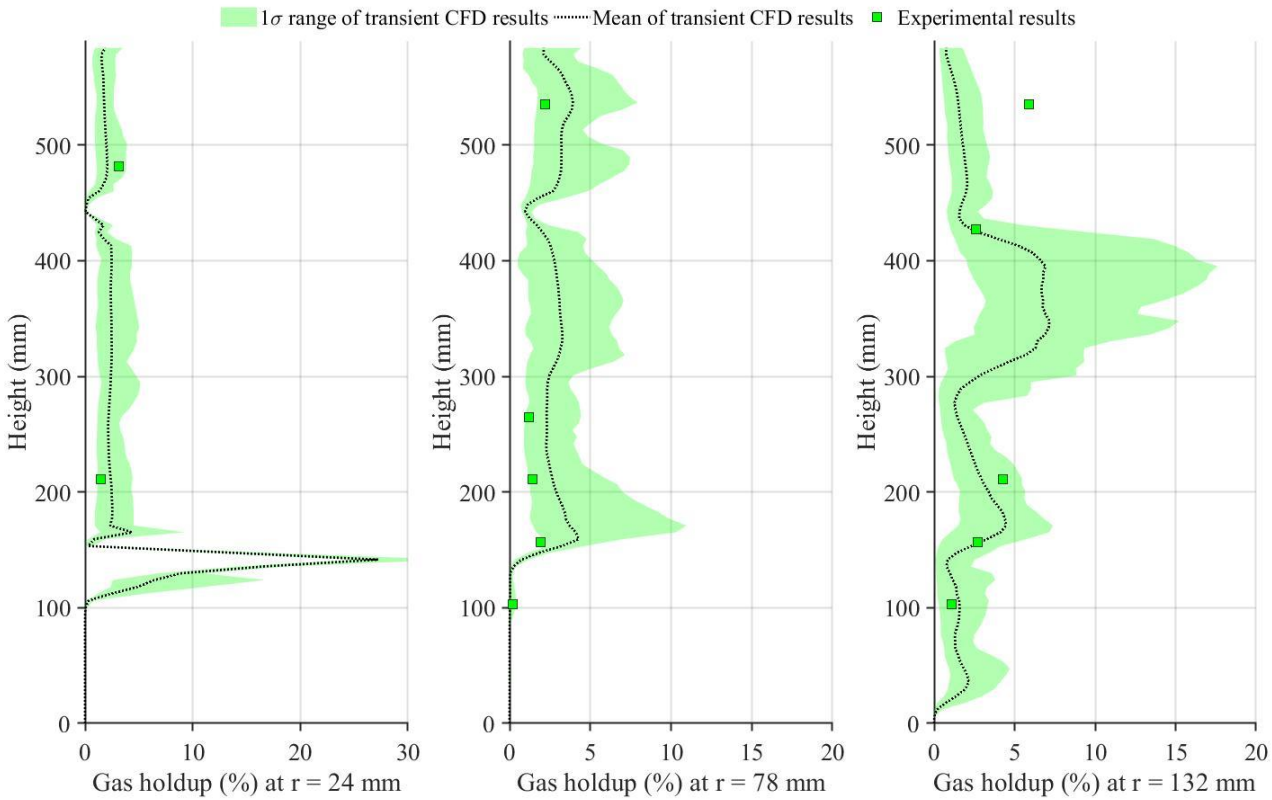

Figure 4-6. Comparison between the modeling and experimental local gas holdup data.

4.5.2. Optimization results

The saturated Pareto front was earned after 100 iterations including the ten initial samples and ten constraint violations. Figure 4-7 (a) shows a graph of the Pareto fronts at every tenth iteration, in which an older Pareto front is drawn on top of the newer ones. If a line with a new color appears to the southwest of the existing lines, it means that the Pareto front progresses during the last ten iterations from that time. In addition, the number in the parentheses indicates the iteration number of that point.

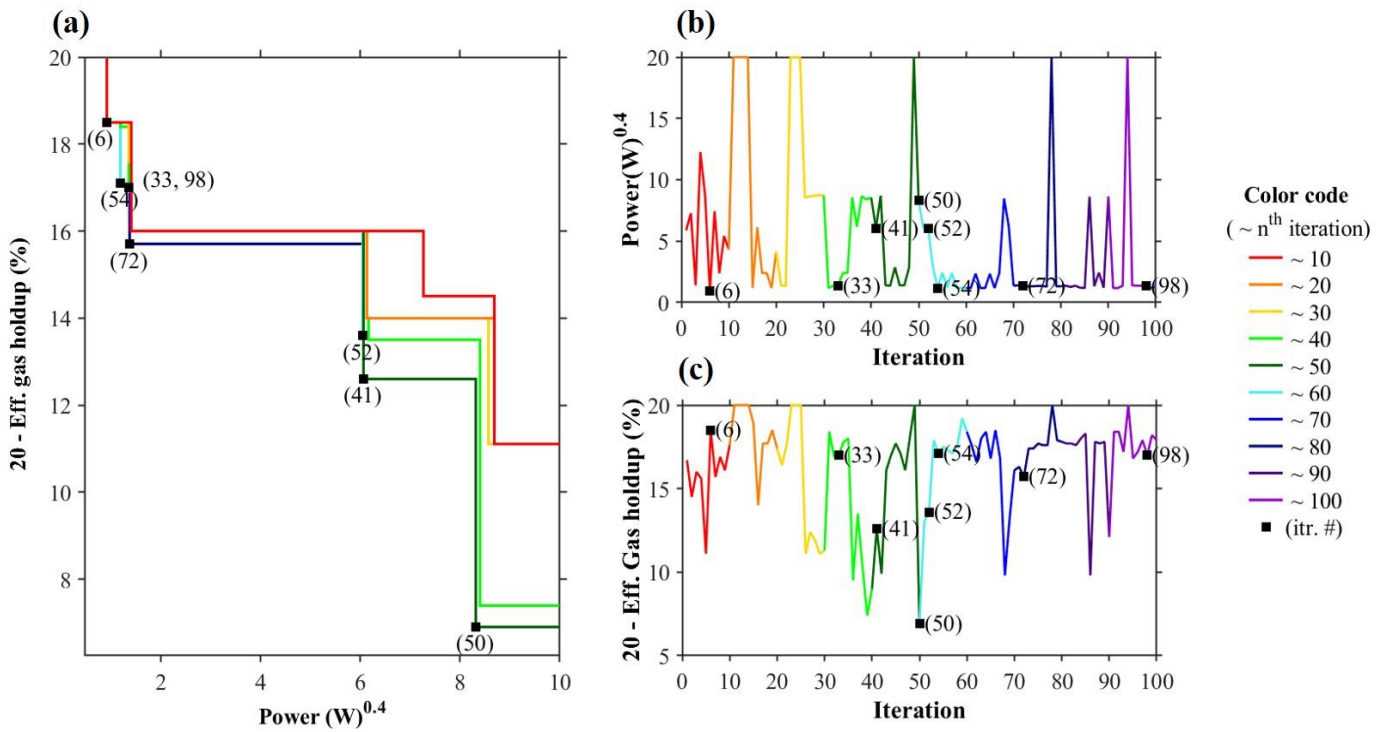

Figure 4-7. (a) Advance of the Pareto front as the number of iteration increases, (b) the trend of the first objective function ($power(\mathrm{x})^{0.4}$) values along the iterations, and (c) the trend of the second objective function ($20 - egh(\mathrm{x})$) values along the iterations.

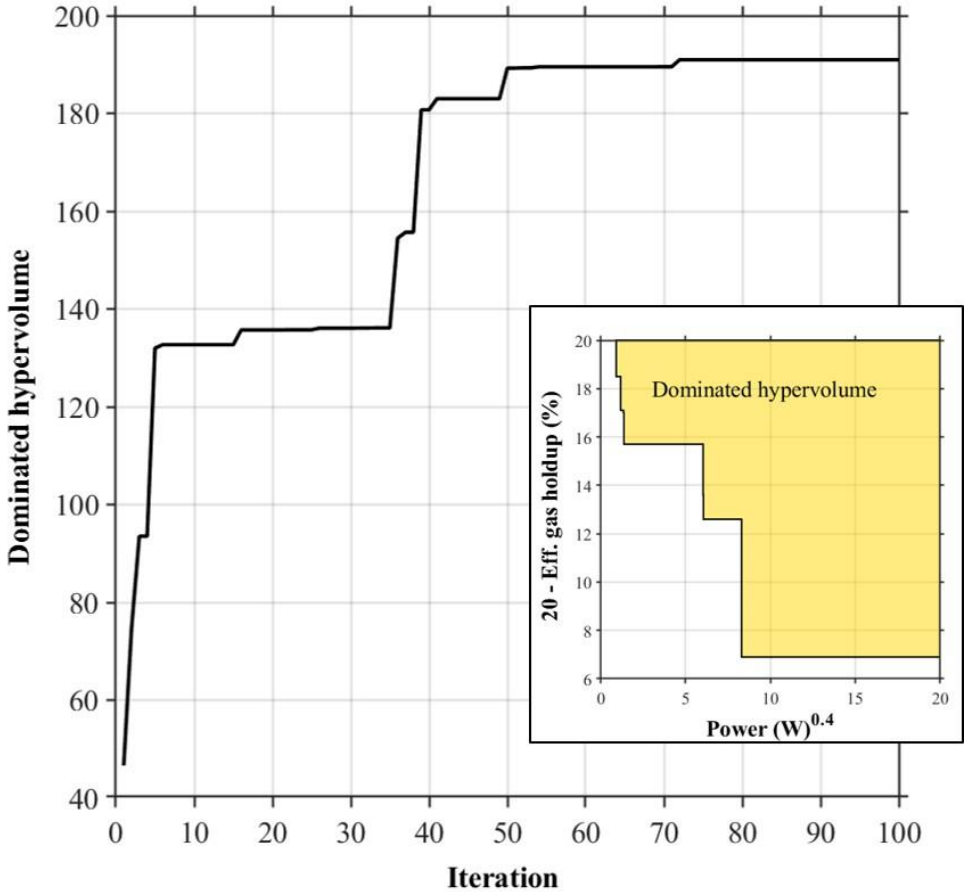

Figure 4-8. Saturation of Pareto front with respect to the concept of dominated hypervolume.

A couple of factors which show the saturation of Pareto front are observed. First, as shown in Figure 4-7 (a), the significant improvement of the Pareto front is not observed after the 72th iteration. Although the last member of the final Pareto front is added at the 98th iteration, it has the exactly the same values as the previous element, added at the 33th iteration. Second, the dominated hypervolume, which is defined as the area between the Pareto front and the maximum values of the objective functions, is negligibly increased after the 50th iteration. Figure 4-8 illustrates well the increase in the dominated hypervolume.

The saturation of the Pareto front does not qualify its global optimality, which means that a further improvement of the Pareto front can still occur after many iterations. However, a few aspects support my decision to stop the optimization after 100 iterations. First, there have been sufficient attempts to explore new areas. In Figure 4-7 (b) and (c), it can be seen how the two objective function values change as the iterations proceed. During the first ten iterations, the plots go up and down without any apparent trends because they are the samples randomly drawn from a Latin hypercube. After the initial evaluations, the CFD-MBO optimizer searches for designs with similar power and gas holdup levels for a certain period of time, and occasionally jumps to designs with different levels. This shows that the optimizer performs both global and local searches during the optimization process. After the 50th iteration, there is a negligible increase in the dominated hypervolume, even though several attempts at exploration have taken place and three more elements are added to the Pareto set. Second, the average u_{EMmi} changes during the optimization can be an indicator. The value of u_{EMmi} not only has a role as a sampling criterion,

it also provides a measure of the expected improvement of the Pareto front because its value is the expected distance advancing from the incumbent Pareto front. The value decreases gradually as the iterations proceed, and reaches below 0.35 at the 100^{th} iteration, which implies that the expected decrease of any objective function reaches below 0.35. It is deduced that an improvement of 0.35 for both objective functions is not critical to this problem, and the designs that are within the Pareto front are close to an optimum. However, it is the user's choice to proceed the iterations until the average u_{EMmi} value becomes much lower and more precise solutions are obtained.

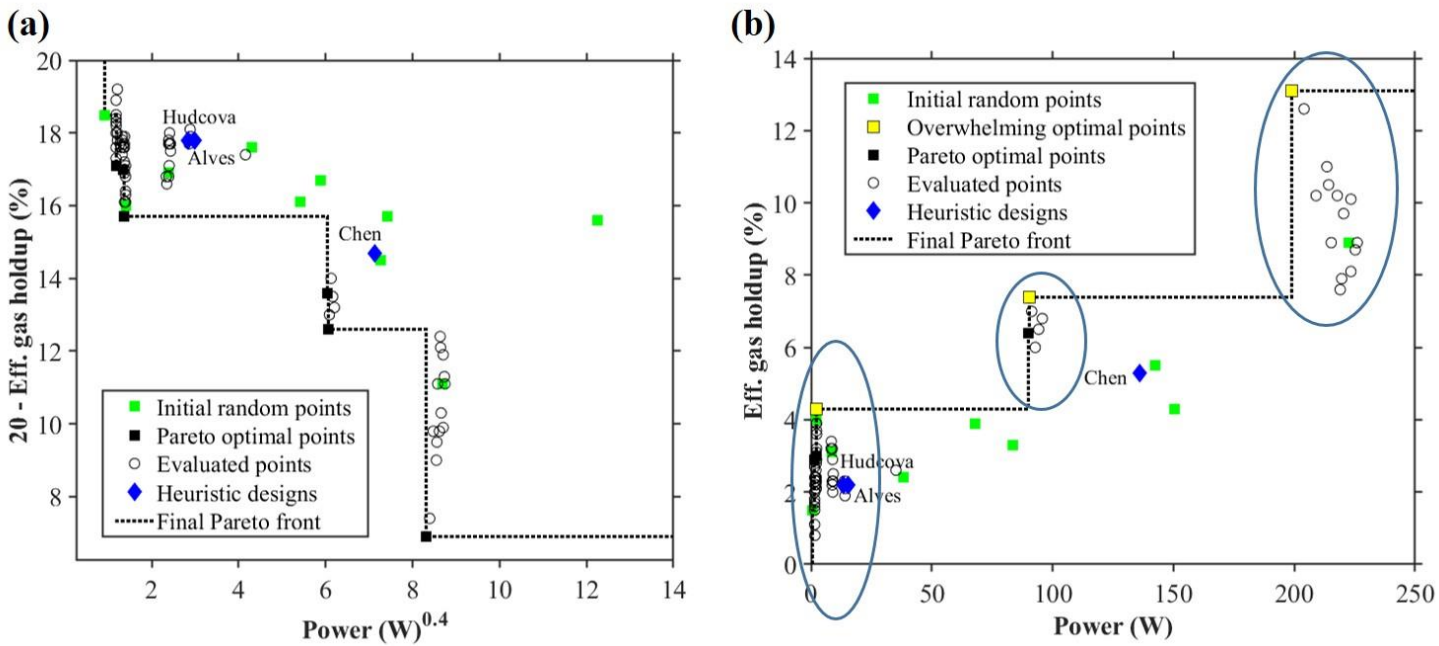

Figure 4-9. Optimization results (a) in the objective function space and (b) with respect to the original performance functions.

Figure 4-9 shows the results of all designs the optimizer has evaluated. The left graph is based on the actual objective functions, which are the transformed versions of the original performance functions, and the graph on the right side shows the results with respect to the original performance indicators. Three notable points are observed from these graphs. First, although most of the evaluated points are not sharply located at the Pareto front, most are close to it. It is the strength of Bayesian optimization that does not waste the computational resource to evaluate unlikely points. The superior results of general BO samples to random initial samples also reveal the efficiency of the BO sampling strategy. Second, the designs in the saturated Pareto set outperform the reference designs reported in the literature. To compare the resulting optimal designs, three designs from Alves et al. [75], Hudcova et al. [121], and M. Chen et al. [43] were chosen, as references, all of which are gas-liquid stirred tank reactors with dual Rushton impellers and their design parameters fallen into this problem's range. For fair comparisons, only the ratios between the design parameters were extracted and simulations were carried out in the same volume reactor with those ratios. This is a reasonable treatment because the design heuristics also provide instructions in terms of the ratios. In Figure 4-9, it can be seen that the performances of the Pareto front designs are superior to the reference designs. Third, the Pareto front seems to be discontinuous, particularly in the *x*-axis direction. One reason is that the two objective functions are not always in a trade-off relationship. If they were in a strict trade-off relationship, the Pareto front would take a continuous shape. It is true that a high level of power is required to obtain a high level of gas holdup because the strong liquid flow from the large impellers, which consume a large amount of

power, can distribute a large amount of gas. However, saving power and increasing the gas holdup do not conflict at small scales, at which the positions of the sparger and the impellers can make a difference. Another reason is the discontinuous input domain in the problem formulation. The discrete input values result in discrete output values. In particular, the power consumption has a strong positive correlation with a single parameter, the impeller diameter (see Figure 4-10), whereas the gas holdup is affected by more parameters. This explains why the Pareto front is more discontinuous with respect to the *abscissa*.

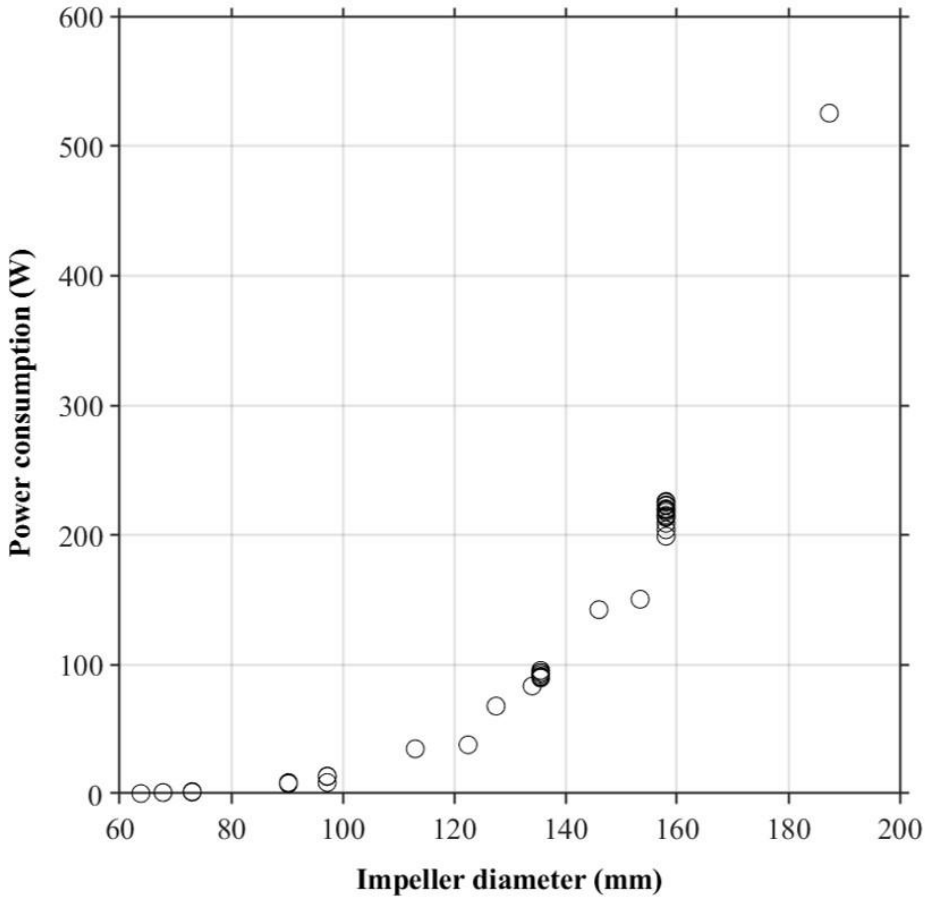

Figure 4-10. Relationship between the impeller diameter and power consumption based on the data obtained during the optimization.

4.5.3. Analysis of optimal designs

This section discusses the optimal designs found from the optimization process, as well as their performances. The final designs were selected based on the plot shown in Figure 4-9 (b). Even within the final Pareto front, there are three designs that outperformed the others from a practical point of view, which are referred to as overwhelming optimal designs, representing the low-power-low-gas holdup, the medium-power-medium gas-holdup, and the high-power-high-gas holdup reactor groups, respectively. For comparison, three outperforming designs were chosen among the initial designs, representing the low, medium, and high groups, respectively. The reference designs, two of which are included in the low group and one of which, in the medium group, are also compared. Unfortunately, it was not possible to find a reference design that can be categorized into the high-power-high-gas holdup group.

Figure 11. (b), (c) and (d) provide two-dimensional side views and contour plots of a gas holdup at the same ratio as the real reactors. The specific values of the design variables and performances of all reactors used in the comparison are given in Table 4-2.

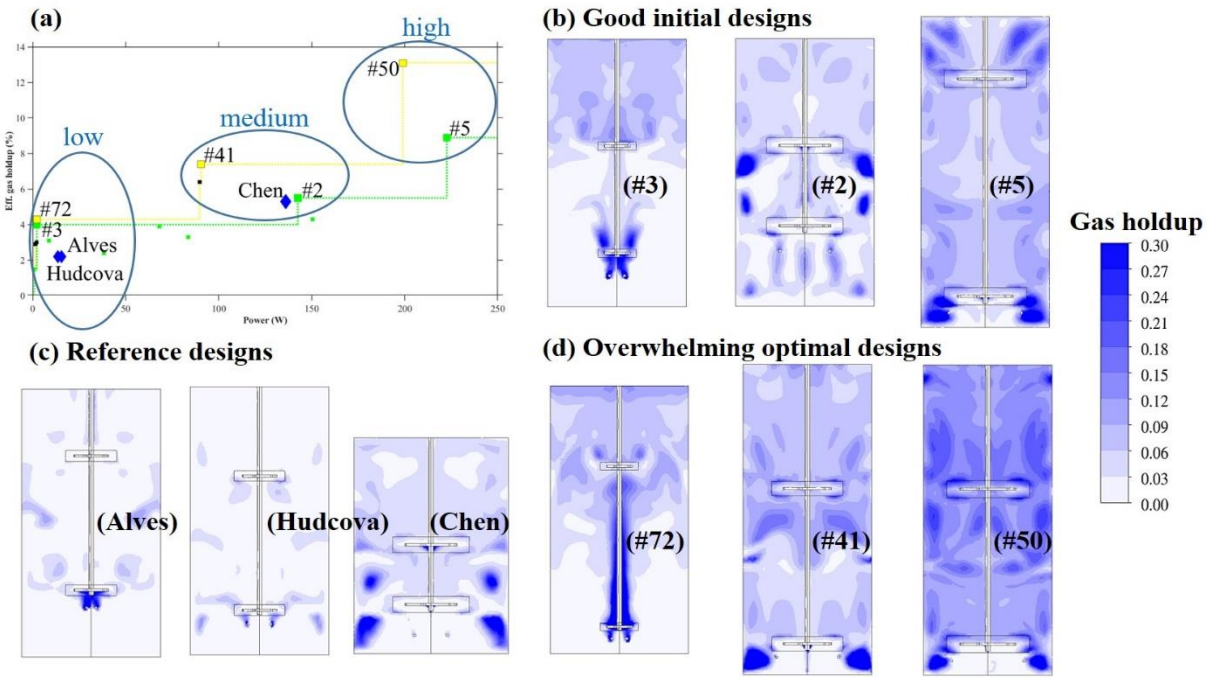

Figure 4-11. (a) The location of each group in the objective function space, (b) the structures and 2D contours of a gas holdup in good initial designs, (c) the structures and 2D contours of the gas holdup in the reference designs, and (d) the structures and 2D contours of the gas holdup in overwhelming optimal designs.

Table 4-2. Detailed specifications and the performances of the initial, reference, and optimal reactors.

	#	Category	Power (W)	Effective gas holdup	H/T	C_1/H	C_2/H	d/D	D/T	h/ C_1
Initial designs	3	Low	2.3	4.0%	2	0.2	0.6	0.5	0.25	0.6
	2	Medium	142.5	5.5%	2	0.3	0.6	0.75	0.5	0.7
	5	High	222.6	8.9%	2.5	0.1	0.8	1	0.583	0.5
Reference designs	Alves	Low	15.5	2.2%	2	0.25	0.5	0.247	0.333	0.75
	Hudcova	Low	13.6	2.2%	2	0.167	0.667	0.54	0.333	0.714
	Chen	Medium	136.1	5.3%	1.447	0.228	0.504	0.5	0.45	0.394
Optimal designs	72	Low	2.2	4.3%	2	0.1	0.7	0.5	0.25	0.6
	41	Medium	90.5	7.4%	2.5	0.1	0.6	1	0.5	0.6
	50	High	199.1	13.1%	2.5	0.1	0.6	1	0.583	0.5

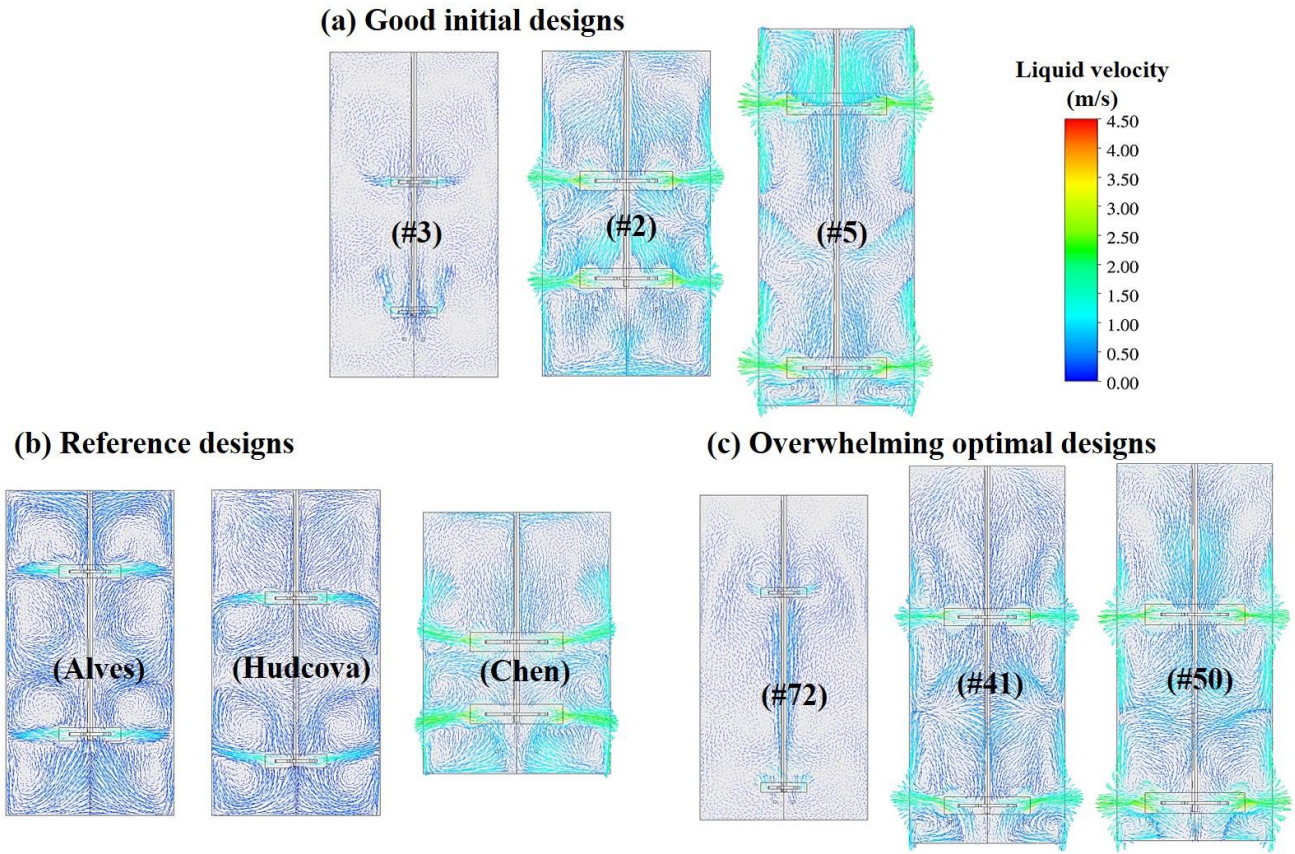

Figure 4-12. Liquid velocity vector space in reactors shown in Figure 4-11.

First, to discuss the designs in the low-power-low-gas holdup group, the optimal design #72 and initial design #3 have an impeller diameter to tank diameter ratio of 0.25, whereas the two reference designs have a ratio of 0.33. The liquid velocity fields of designs #72 and #3, illustrated in Figure 4-12, are weaker than those of Alves and Hudcova. In addition, the gas volume fraction contours of designs #72 and #3 in Figure 4-11 indicates that these reactors are under flooding operations. However, both designs show a superior gas distribution compared to the reference designs. Gas is particularly well distributed in the region above the upper impeller. From this phenomenon, it is suspected that the strong flow field near the surface in Alves and Hudcova may hinder the accumulation of gas in this region.

In the medium group, the distance between impellers seems important. If two impellers are too close, as in design #5 and Chen's design, the flow developed by one impeller is disturbed by the other. In addition, it is advantageous to locate the sparger as low as possible to minimize the volume of the no-gas zone below the sparger.

In the high-power-high gas holdup group, it is observed that the upper impeller close to the surface deteriorates the global gas holdup. The only difference between designs #5 and #50 is the location of the upper impeller. In design #5, the strong liquid flow developed by the high upper impeller location may cause the surface air to become entrapped. In addition, the weak flow field between the impellers owing to the large spacing results in a loss of gas holdup in that region. On the other hand, the high group has the largest impellers among the three groups, which means that such impellers are a critical factor bringing about a high level flow and gas distribution.

4.6. Conclusions

A CFD-MBO optimizer which implements a multi-objective Bayesian optimization to CFD-based optimal design problems was successfully developed. Bayesian optimization is a proper algorithm for functions that are expensive to evaluate, such as CFD-based black-box functions, because it can reduce the number of function evaluations by avoiding a search in regions that are unlikely to be the optimum. The efficiency of the CFD-MBO optimizer was proved in the design problem of a gas-sparged stirred tank reactor with two objectives, six design variables, and topology constraints.

The saturated Pareto front is obtained only after 100 iterations. It consists of eight near-optimal designs that show greatly enhanced performances compared to the initial designs. In addition, the other designs that are sampled by the optimizer tell that the optimizer not only successfully balances the exploitation and exploration, but also finds the suboptimal designs that lie close to the final Pareto front.

The optimal designs on the final Pareto curve are compared with the reference designs from the literature that are designed based upon heuristic rules. As a result, the optimal designs turned out to show better performances in terms of power and gas holdup than these reference designs.

There are three overwhelming designs from the optimal Pareto group that are superior to the other elements in a practical sense. They can represent low-power-low-gas holdup, medium-power-medium-gas holdup, and high-power-high-gas holdup, and the engineers can choose one of them depending on their needs. However,

when there is a specific performance target, one can attempt to achieve the target optimization by setting the objective functions as $target\ gas\ holdup - gas\ holdup$ and $target\ power - power$ and using the transfer learning strategy suggested by [56]. Because the new objective functions are correlated with the current functions, all CFD results obtained in the optimal design process could be good initial points for the new optimization problem, which can be an area of further study.

Finally, the CFD-MBO optimizer can be applied to other CFD-based design problems as well as the reactor design problems. Adjustments of the details such as the number of initial samples, the penalty values for constraint violations, and the number of samples used in the Monte Carlo method may be needed. Although analyzing the effects of these factors is outside the scope of this work, the settings of this study can be applied to other problems as well.

Chapter 5.

Concluding Remarks

The problem of industrial-scale chemical reactor designs can be resolved by taking advantage of cutting-edge techniques developed in the process systems engineering community. Firstly, multi-scale modeling techniques can take account of hugely varying length and time scales in important variables of industrial-scale reactors. In the example of the industrial-scale aqueous mineral carbonation reactor, the sizes of an entire reactor and the portion of the reactor (compartment), in which homogeneous mixing status is ensured, are in big difference. In addition, the time consumptions to numerically solve the governing equations of chemical system (reaction kinetics) and the physical system (hydrodynamics) are so different that it is impossible to solve them simultaneously. The CFD-based compartmental model, which regards a big reactor as a network of homogenous zones and uses CFD simulation results for macro-flows between the zones, can be a great solution for such systems.

Secondly, first-principle reactor models can be intensified by the model calibration. It can be done by introducing parameters at uncertain parts of the model and estimating them to explain the experimental observations most accurately. Bayesian parameter estimation not only derives constant values for the parameters, but also obtains probabilistic distributions of the parameters. Therefore, it helps understanding the lying uncertainties of the predicted results from the model and making safe decisions for the reactor design. The ability of this method is shown in the

intensification of aqueous mineral carbonation reactor model; it was shown that Bayesian parameter estimation generates more accurate model outputs as well as their confidence bound than conventional parameter estimation methods.

Lastly, precisely developed reactor models can be plugged into optimization algorithms to obtain the optimal design; objective function be the reactor performance and optimization variables be the design parameters. Black-box optimization algorithms are simple-to-use and powerful tools to combine with the reactor models which have high non-linearity or are built on commercial software. Bayesian optimization is recommended for expensive models like CFD models in that it reduces the number of iterations by introducing selection criteria for point-to-be-evaluated. Multi-objective Bayesian optimization to maximize the gas holdup and minimize the power consumption in a gas-liquid stirred reactor was successfully executed and produced several optimal design candidates (on Pareto curve) which outperform the heuristic designs.

The process of modeling, calibration and optimization that this thesis suggests for the successful design of industrial chemical reactors can be illustrated as in Figure 5-1.

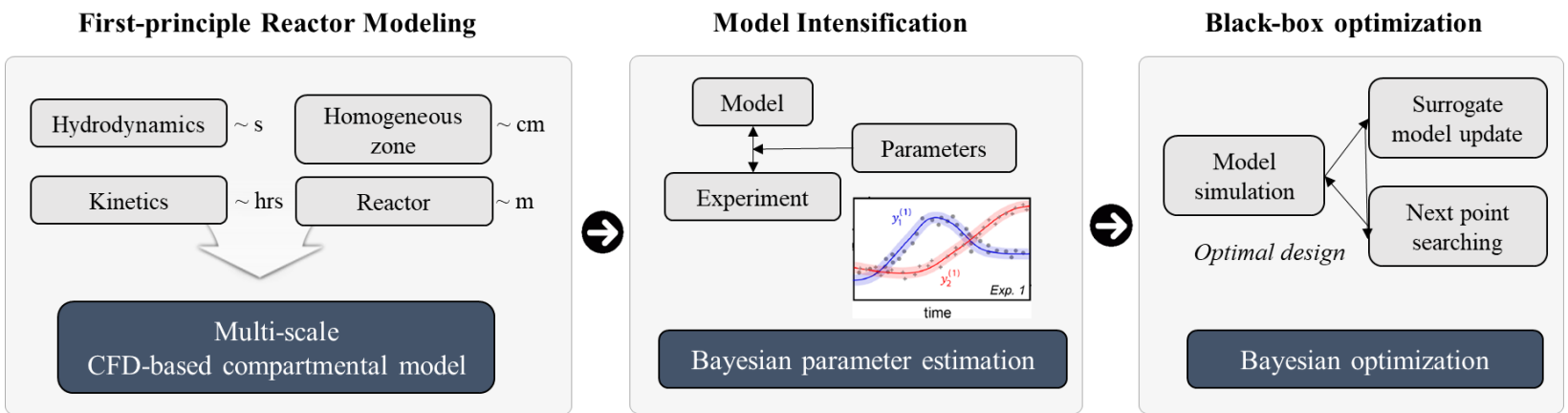

Figure 5-1. Optimal design process of industrial-scale chemical reactor.

Bibliography

[1] G. Kasat, A. Khopkar, V. Ranade, and A. Pandit, "CFD simulation of liquid-phase mixing in solid–liquid stirred reactor," *Chemical Engineering Science,* vol. 63, pp. 3877-3885, 2008.

[2] E. Delnoij, J. Kuipers, and W. Van Swaaij, "A three-dimensional CFD model for gas–liquid bubble columns," *Chemical Engineering Science,* vol. 54, pp. 2217-2226, 1999.

[3] A. G. Dixon and M. Nijemeisland, "CFD as a design tool for fixed-bed reactors," *Industrial & Engineering Chemistry Research,* vol. 40, pp. 5246-5254, 2001.

[4] F. Kerdouss, A. Bannari, P. Proulx, R. Bannari, M. Skrga, and Y. Labrecque, "Two-phase mass transfer coefficient prediction in stirred vessel with a CFD model," *Computers & chemical engineering,* vol. 32, pp. 1943-1955, 2008.

[5] M. Kim, J. Na, S. Park, J.-H. Park, and C. Han, "Modeling and validation of a pilot-scale aqueous mineral carbonation reactor for carbon capture using computational fluid dynamics," *Chemical Engineering Science,* vol. 177, pp. 301-312, 2018.

[6] S.-C. Kong, "A study of natural gas/DME combustion in HCCI engines using CFD with detailed chemical kinetics," *Fuel,* vol. 86, pp. 1483-1489, 2007.

[7] Z. Bao, F. Yang, Z. Wu, S. N. Nyamsi, and Z. Zhang, "Optimal design of metal hydride reactors based on CFD–Taguchi combined method," *Energy conversion and management,* vol. 65, pp. 322-330, 2013.

[8] J. Ding, X. Wang, X.-F. Zhou, N.-Q. Ren, and W.-Q. Guo, "CFD optimization of continuous stirred-tank (CSTR) reactor for biohydrogen production," *Bioresource technology,* vol. 101, pp. 7005-7013, 2010.

[9] Á. Frías-Ferrer, I. Tudela, O. Louisnard, V. Sáez, M. D. Esclapez, M. I. Díez-García*, et al.*, "Optimized design of an electrochemical filter-press

reactor using CFD methods," *Chemical engineering journal,* vol. 169, pp. 270-281, 2011.

[10] I. K. Gamwo, J. S. Halow, D. Gidaspow, and R. Mostofi, "CFD models for methanol synthesis three-phase reactors: reactor optimization," *Chemical Engineering Journal,* vol. 93, pp. 103-112, 2003.

[11] S. Tavelli, R. Rota, and M. Derudi, "A critical comparison between CFD and zone models for the consequence analysis of fires in congested environments," *CHEMICAL ENGINEERING,* vol. 36, 2014.

[12] A. Delafosse, F. Delvigne, M.-L. Collignon, M. Crine, P. Thonart, and D. Toye, "Development of a compartment model based on CFD simulations for description of mixing in bioreactors," *Biotechnol. Agron. Soc. Environ,* vol. 14, pp. 517-522, 2010.

[13] P. Vrabel, R. Van der Lans, Y. Cui, and K. C. A. Luyben, "Compartment model approach: Mixing in large scale aerated reactors with multiple impellers," *Chemical Engineering Research and Design,* vol. 77, pp. 291-302, 1999.

[14] P. Vrábel, R. G. van der Lans, F. N. van der Schot, K. C. A. Luyben, B. Xu, and S.-O. Enfors, "CMA: integration of fluid dynamics and microbial kinetics in modelling of large-scale fermentations," *Chemical engineering journal,* vol. 84, pp. 463-474, 2001.

[15] J. Zahradník, R. Mann, M. Fialova, D. Vlaev, S. Vlaev, V. Lossev*, et al.*, "A networks-of-zones analysis of mixing and mass transfer in three industrial bioreactors," *Chemical engineering science,* vol. 56, pp. 485-492, 2001.

[16] U. Boltersdorf, G. Deerberg, and S. Schlüter, "Computational study of the effects of process parameters on the product distribution for mixing sensitive reactions and on distribution of gas in stirred tank reactors," *Recent research developments in chemical engineering,* pp. 15-43, 2000.

[17] A. Nørregaard, C. Bach, U. Krühne, U. Borgbjerg, and K. V. Gernaey, "Hypothesis-driven compartment model for stirred bioreactors utilizing computational fluid dynamics and multiple pH sensors," *Chemical*

Engineering Journal, vol. 356, pp. 161-169, 2019.

[18] S. Yang, S. Kiang, P. Farzan, and M. Ierapetritou, "Optimization of Reaction Selectivity Using CFD-Based Compartmental Modeling and Surrogate-Based Optimization," *Processes,* vol. 7, p. 9, 2019.

[19] F. Bezzo, S. Macchietto, and C. Pantelides, "General hybrid multizonal/CFD approach for bioreactor modeling," *AIChE Journal,* vol. 49, pp. 2133-2148, 2003.

[20] M. Gresch, R. Brügger, A. Meyer, and W. Gujer, "Compartmental models for continuous flow reactors derived from CFD simulations," *Environmental science & technology,* vol. 43, pp. 2381-2387, 2009.

[21] W. Zhao, A. Buffo, V. Alopaeus, B. Han, and M. Louhi-Kultanen, "Application of the compartmental model to the gas–liquid precipitation of CO2-Ca (OH) 2 aqueous system in a stirred tank," *AIChE Journal,* vol. 63, pp. 378-386, 2017.

[22] S. Hosder, R. Walters, and R. Perez, "A non-intrusive polynomial chaos method for uncertainty propagation in CFD simulations," in *44th AIAA aerospace sciences meeting and exhibit*, 2006, p. 891.

[23] H. N. Najm, "Uncertainty quantification and polynomial chaos techniques in computational fluid dynamics," *Annual review of fluid mechanics,* vol. 41, pp. 35-52, 2009.

[24] A. Mesbah, "Stochastic model predictive control with active uncertainty learning: A survey on dual control," *Annual Reviews in Control,* vol. 45, pp. 107-117, 2018.

[25] J. A. Paulson and A. Mesbah, "An efficient method for stochastic optimal control with joint chance constraints for nonlinear systems," *International Journal of Robust and Nonlinear Control,* vol. 29, pp. 5017-5037, 2019.

[26] X. Huan and Y. M. Marzouk, "Simulation-based optimal Bayesian experimental design for nonlinear systems," *Journal of Computational Physics,* vol. 232, pp. 288-317, 2013.

[27] C. A. Kastner, A. Braumann, P. L. Man, S. Mosbach, G. P. Brownbridge, J. Akroyd*, et al.*, "Bayesian parameter estimation for a jet-milling model using Metropolis–Hastings and Wang–Landau sampling," *Chemical Engineering Science,* vol. 89, pp. 244-257, 2013.

[28] B. A. Konomi, G. Karagiannis, K. Lai, and G. Lin, "Bayesian Treed Calibration: an application to carbon capture with AX sorbent," *Journal of the American Statistical Association,* vol. 112, pp. 37-53, 2017.

[29] K. Li, P. Mahapatra, K. S. Bhat, D. C. Miller, and D. S. Mebane, "Multi-scale modeling of an amine sorbent fluidized bed adsorber with dynamic discrepancy reduced modeling," *Reaction Chemistry & Engineering,* vol. 2, pp. 550-560, 2017.

[30] M. C. Coleman and D. E. Block, "Bayesian parameter estimation with informative priors for nonlinear systems," *AIChE journal,* vol. 52, pp. 651-667, 2006.

[31] J. H. Bak and J. W. Pillow, "Adaptive stimulus selection for multi-alternative psychometric functions with lapses," *Journal of vision,* vol. 18, pp. 4-4, 2018.

[32] N. Christensen, R. Meyer, L. Knox, and B. Luey, "Bayesian methods for cosmological parameter estimation from cosmic microwave background measurements," *Classical and Quantum Gravity,* vol. 18, p. 2677, 2001.

[33] G. Xiao, M. Brady, J. A. Noble, and Y. Zhang, "Segmentation of ultrasound B-mode images with intensity inhomogeneity correction," *IEEE Transactions on medical imaging,* vol. 21, pp. 48-57, 2002.

[34] Z. Ghahramani, "Probabilistic machine learning and artificial intelligence," *Nature,* vol. 521, pp. 452-459, 2015.

[35] S. Mosbach, A. Braumann, P. L. Man, C. A. Kastner, G. P. Brownbridge, and M. Kraft, "Iterative improvement of Bayesian parameter estimates for an engine model by means of experimental design," *Combustion and Flame,* vol. 159, pp. 1303-1313, 2012.

[36] M. Abbasi and A. Gholami, "Polynomial chaos expansion for nonlinear geophysical inverse problems," *Geophysics,* vol. 82, pp. R259-R268, 2017.

[37] M. B. Giles and N. A. Pierce, "An introduction to the adjoint approach to design," *Flow, turbulence and combustion,* vol. 65, pp. 393-415, 2000.

[38] S. Kim, J. J. Alonso, and A. Jameson, "Two-dimensional high-lift aerodynamic optimization using the continuous adjoint method," *AIAA paper,* vol. 4741, 2000.

[39] A. Jameson, S. Shankaran, L. Martinelli, and B. Haimes, "Aerodynamic shape optimization of complete aircraft configurations using unstructured grids," in *42nd AIAA Aerospace Sciences Meeting and Exhibit*, 2004, p. 533.

[40] K. Deb, A. Pratap, S. Agarwal, and T. Meyarivan, "A fast and elitist multiobjective genetic algorithm: NSGA-II," *IEEE transactions on evolutionary computation,* vol. 6, pp. 182-197, 2002.

[41] C. Poloni, A. Giurgevich, L. Onesti, and V. Pediroda, "Hybridization of a multi-objective genetic algorithm, a neural network and a classical optimizer for a complex design problem in fluid dynamics," *Computer Methods in Applied Mechanics and Engineering,* vol. 186, pp. 403-420, 2000.

[42] K. Uebel, P. Rößger, U. Prüfert, A. Richter, and B. Meyer, "CFD-based multi-objective optimization of a quench reactor design," *Fuel Processing Technology,* vol. 149, pp. 290-304, 2016.

[43] M. Chen, J. Wang, S. Zhao, C. Xu, and L. Feng, "Optimization of Dual-Impeller Configurations in a Gas–Liquid Stirred Tank Based on Computational Fluid Dynamics and Multiobjective Evolutionary Algorithm," *Industrial & Engineering Chemistry Research,* vol. 55, pp. 9054-9063, 2016.

[44] J. Na, K. S. Kshetrimayum, U. Lee, and C. Han, "Multi-objective optimization of microchannel reactor for Fischer-Tropsch synthesis using computational fluid dynamics and genetic algorithm," *Chemical*

Engineering Journal, vol. 313, pp. 1521-1534, 2017.

[45] K. Deb and T. Goel, "A hybrid multi-objective evolutionary approach to engineering shape design," in *International conference on evolutionary multi-criterion optimization*, 2001, pp. 385-399.

[46] L. Dumas, B. Druez, and N. Lecerf, "A fully adaptive hybrid optimization of aircraft engine blades," *Journal of Computational and Applied Mathematics,* vol. 232, pp. 54-60, 2009.

[47] F. Muyl, L. Dumas, and V. Herbert, "Hybrid method for aerodynamic shape optimization in automotive industry," *Computers & Fluids,* vol. 33, pp. 849-858, 2004.

[48] I. Jung, K. S. Kshetrimayum, S. Park, J. Na, Y. Lee, J. An*, et al.*, "Computational fluid dynamics based optimal design of guiding channel geometry in U-type coolant layer manifold of large-scale microchannel Fischer–Tropsch reactor," *Industrial & Engineering Chemistry Research,* vol. 55, pp. 505-515, 2016.

[49] Y. S. Ong, P. Nair, A. Keane, and K. Wong, "Surrogate-assisted evolutionary optimization frameworks for high-fidelity engineering design problems," in *Knowledge Incorporation in Evolutionary Computation*, ed: Springer, 2005, pp. 307-331.

[50] P. Rößger and A. Richter, "Performance of different optimization concepts for reactive flow systems based on combined CFD and response surface methods," *Computers & Chemical Engineering,* vol. 108, pp. 232-239, 2018.

[51] E. Rigoni and A. Turco, "Metamodels for Fast Multi-objective Optimization: Trading Off Global Exploration and Local Exploitation," in *SEAL*, 2010, pp. 523-532.

[52] B. Shahriari, K. Swersky, Z. Wang, R. P. Adams, and N. de Freitas, "Taking the human out of the loop: A review of bayesian optimization," *Proceedings of the IEEE,* vol. 104, pp. 148-175, 2016.

[53] M. Emmerich, K. Yang, A. Deutz, H. Wang, and C. M. Fonseca, "A

multicriteria generalization of bayesian global optimization," in *Advances in Stochastic and Deterministic Global Optimization*, ed: Springer, 2016, pp. 229-242.

[54] P. Feliot, J. Bect, and E. Vazquez, "A Bayesian approach to constrained single-and multi-objective optimization," *Journal of Global Optimization,* vol. 67, pp. 97-133, 2017.

[55] M. A. Gelbart, J. Snoek, and R. P. Adams, "Bayesian optimization with unknown constraints," *arXiv preprint arXiv:1403.5607,* 2014.

[56] K. Swersky, J. Snoek, and R. P. Adams, "Multi-task bayesian optimization," in *Advances in neural information processing systems*, 2013, pp. 2004-2012.

[57] P. Chen, J. Xia, B. M. Merrick, and T. J. Brazil, "Multiobjective Bayesian optimization for active load modulation in a broadband 20-W GaN Doherty power amplifier design," *IEEE Transactions on Microwave Theory and Techniques,* vol. 65, pp. 860-871, 2017.

[58] C. Li, D. R. de Celis Leal, S. Rana, S. Gupta, A. Sutti, S. Greenhill*, et al.*, "Rapid Bayesian optimisation for synthesis of short polymer fiber materials," *Scientific reports,* vol. 7, p. 5683, 2017.

[59] J. Park and K. H. Law, "A Bayesian optimization approach for wind farm power maximization," in *Smart Sensor Phenomena, Technology, Networks, and Systems Integration 2015*, 2015, p. 943608.

[60] J. Snoek, H. Larochelle, and R. P. Adams, "Practical bayesian optimization of machine learning algorithms," in *Advances in neural information processing systems*, 2012, pp. 2951-2959.

[61] L. R. Zuhal, C. Amalinadhi, Y. B. Dwianto, P. S. Palar, and K. Shimoyama, "Benchmarking Multi-Objective Bayesian Global Optimization Strategies for Aerodynamic Design," in *2018 AIAA/ASCE/AHS/ASC Structures, Structural Dynamics, and Materials Conference*, 2018, p. 0914.

[62] M. Bui, C. S. Adjiman, A. Bardow, E. J. Anthony, A. Boston, S. Brown,

et al., "Carbon capture and storage (CCS): the way forward," *Energy & Environmental Science,* vol. 11, pp. 1062-1176, 2018.

[63] A. Otto, T. Grube, S. Schiebahn, and D. Stolten, "Closing the loop: Captured CO 2 as a feedstock in the chemical industry," *Energy & environmental science,* vol. 8, pp. 3283-3297, 2015.

[64] J. A. Herron, J. Kim, A. A. Upadhye, G. W. Huber, and C. T. Maravelias, "A general framework for the assessment of solar fuel technologies," *Energy & Environmental Science,* vol. 8, pp. 126-157, 2015.

[65] S.-Y. Pan, R. Adhikari, Y.-H. Chen, P. Li, and P.-C. Chiang, "Integrated and innovative steel slag utilization for iron reclamation, green material production and CO2 fixation via accelerated carbonation," *Journal of Cleaner Production,* vol. 137, pp. 617-631, 2016.

[66] A. Sanna, M. Uibu, G. Caramanna, R. Kuusik, and M. Maroto-Valer, "A review of mineral carbonation technologies to sequester CO 2," *Chemical Society Reviews,* vol. 43, pp. 8049-8080, 2014.

[67] E. Rubin and H. De Coninck, "IPCC special report on carbon dioxide capture and storage," *UK: Cambridge University Press. TNO (2004): Cost Curves for CO2 Storage, Part,* vol. 2, p. 14, 2005.

[68] Orica. http://www.orica.com/ (accessed July 2018).

[69] Futurism. https://futurism.com/revolutionary-carbon-capture-method-makes-building-materials-out-of-emissions/ (accessed July 2018).

[70] Calera Corporation. http://www.calera.com/beneficial-reuse-of-co2/scale-up.html (accessed July 2018).

[71] Cleantech Group. https://www.cleantech.com/between-a-rock-and-hard-place-commercializing-co2-through-mineralization/, (accessed July 2018).

[72] Chosun Biz internet news. http://biz.chosun.com/site/data/html_dir/2017/06/26/2017062600894.

html (accessed July 2018).

[73] The Asia Business Daily internet news. http://www.asiae.co.kr/news/view.htm?idxno=2015070916592973869, (accessed July 2018).

[74] A. Scott, "Learning to love CO2," *Chemical & Engineering News,* vol. 93, pp. 10-16, 2015.

[75] S. Alves, C. Maia, and J. Vasconcelos, "Experimental and modelling study of gas dispersion in a double turbine stirred tank," *Chemical Engineering Science,* vol. 57, pp. 487-496, 2002.

[76] M. J. Mitchell, O. E. Jensen, K. A. Cliffe, and M. M. Maroto-Valer, "A model of carbon dioxide dissolution and mineral carbonation kinetics," *Proceedings of the Royal Society A: Mathematical, Physical and Engineering Sciences,* vol. 466, pp. 1265-1290, 2009.

[77] J. Na, S. Park, J. H. Bak, M. Kim, D. Lee, Y. Yoo*, et al.*, "Bayesian inference of aqueous mineral carbonation kinetics for carbon capture and utilization," *Industrial & Engineering Chemistry Research,* 2019.

[78] O. Velts, M. Uibu, J. Kallas, and R. Kuusik, "Waste oil shale ash as a novel source of calcium for precipitated calcium carbonate: Carbonation mechanism, modeling, and product characterization," *Journal of hazardous materials,* vol. 195, pp. 139-146, 2011.

[79] N. G. Deen, T. Solberg, and B. H. Hjertager, "Large eddy simulation of the gas–liquid flow in a square cross-sectioned bubble column," *Chemical Engineering Science,* vol. 56, pp. 6341-6349, 2001.

[80] D. Zhang, N. Deen, and J. Kuipers, "Numerical modeling of hydrodynamics, mass transfer and chemical reaction in bubble Columns," 2007.

[81] S. Kakaraniya, A. Gupta, and A. Mehra, "Reactive Precipitation in Gas-Slurry Systems: The CO2− Ca (OH) 2− CaCO3 System," *Industrial & engineering chemistry research,* vol. 46, pp. 3170-3179, 2007.

[82] E. L. Paul, V. A. Atiemo-Obeng, and S. M. Kresta, *Handbook of industrial mixing: science and practice*: John Wiley & Sons, 2004.

[83] A. C. Hindmarsh, P. N. Brown, K. E. Grant, S. L. Lee, R. Serban, D. E. Shumaker*, et al.*, "SUNDIALS: Suite of nonlinear and differential/algebraic equation solvers," *ACM Transactions on Mathematical Software (TOMS),* vol. 31, pp. 363-396, 2005.

[84] D. Kang, M.-G. Lee, H. Jo, Y. Yoo, S.-Y. Lee, and J. Park, "Carbon capture and utilization using industrial wastewater under ambient conditions," *Chemical Engineering Journal,* vol. 308, pp. 1073-1080, 2017.

[85] D. Kang, S. Park, H. Jo, and J. Park, "Carbon fixation using calcium oxide by an aqueous approach at moderate conditions," *Chemical Engineering Journal,* vol. 248, pp. 200-207, 2014.

[86] H. Brauer, "Particle/fluid transport processes," *Prog. Chem. Eng.,* vol. 19, pp. 61-99, 1981.

[87] G. Ratcliff and J. Holdcroft, "Diffusivities of gases in aqueous electrolyte solutions," *Trans. Inst. Chem. Eng,* vol. 41, pp. 315-319, 1963.

[88] K. R. Westerterp, W. Van Swaaij, A. Beenackers, and H. Kramers, "Chemical reactor design and operation," 1984.

[89] D. Zhang, N. Deen, and J. Kuipers, "Numerical modeling of hydrodynamics, mass transfer and chemical reaction in bubble Columns," in *6th International Conference on Multiphase Flow, ICMF 2007, Leipzig, Germany*, 2007.

[90] G. F. Versteeg and W. P. Van Swaaij, "Solubility and diffusivity of acid gases (carbon dioxide, nitrous oxide) in aqueous alkanolamine solutions," *Journal of Chemical & Engineering Data,* vol. 33, pp. 29-34, 1988.

[91] S. Weisenberger and d. A. Schumpe, "Estimation of gas solubilities in salt solutions at temperatures from 273 K to 363 K," *AIChE Journal,*

vol. 42, pp. 298-300, 1996.

[92] K. Johannsen and S. Rademacher, "Modelling the kinetics of calcium hydroxide dissolution in water," *Acta hydrochimica et hydrobiologica,* vol. 27, pp. 72-78, 1999.

[93] H. Wiechers, P. Sturrock, and G. Marais, "Calcium carbonate crystallization kinetics," *Water Research,* vol. 9, pp. 835-845, 1975.

[94] R. Pohorecki and W. d. w. Moniuk, "Kinetics of reaction between carbon dioxide and hydroxyl ions in aqueous electrolyte solutions," *Chemical Engineering Science,* vol. 43, pp. 1677-1684, 1988.

[95] H. Hikita, S. Asai, and T. Takatsuka, "Absorption of carbon dioxide into aqueous sodium hydroxide and sodium carbonate-bicarbonate solutions," *The Chemical Engineering Journal,* vol. 11, pp. 131-141, 1976.

[96] M. Eigen, "Methods for investigation of ionic reactions in aqueous solutions with half-times as short as 10–9 sec. Application to neutralization and hydrolysis reactions," *Discussions of the Faraday Society,* vol. 17, pp. 194-205, 1954.

[97] A. Cents, D. W. F. Brilman, and G. Versteeg, "CO2 absorption in carbonate/bicarbonate solutions: The Danckwerts-criterion revisited," *Chemical Engineering Science,* vol. 60, pp. 5830-5835, 2005.

[98] T. Edwards, G. Maurer, J. Newman, and J. Prausnitz, "Vapor-liquid equilibria in multicomponent aqueous solutions of volatile weak electrolytes," *AIChE Journal,* vol. 24, pp. 966-976, 1978.

[99] P. V. Danckwerts, "The absorption of carbon dioxide into solutions of alkalis and amines (with some notes on hydrogen sulfide and carbonyl sulfide)," *The Chemical Engineer,* pp. 244-280, 1966.

[100] L. N. Plummer and E. Busenberg, "The solubilities of calcite, aragonite and vaterite in CO2-H2O solutions between 0 and 90 C, and an evaluation of the aqueous model for the system CaCO3-CO2-H2O," *Geochimica et cosmochimica acta,* vol. 46, pp. 1011-1040, 1982.

[101] A. Atkinson, A. Donev, and R. Tobias, *Optimum experimental designs, with SAS* vol. 34: Oxford University Press, 2007.

[102] G. E. Box and N. R. Draper, *Empirical model-building and response surfaces*: John Wiley & Sons, 1987.

[103] G. E. Box, W. G. Hunter, and J. S. Hunter, "Statistics for experimenters," 1978.

[104] J. Chen and K.-P. Wang, "Sequential experimental design strategy for optimal batch profiles using hybrid function approximations," *Industrial & engineering chemistry research,* vol. 43, pp. 5260-5274, 2004.

[105] M. D. McKay, R. J. Beckman, and W. J. Conover, "Comparison of three methods for selecting values of input variables in the analysis of output from a computer code," *Technometrics,* vol. 21, pp. 239-245, 1979.

[106] N. Metropolis, A. W. Rosenbluth, M. N. Rosenbluth, A. H. Teller, and E. Teller, "Equation of state calculations by fast computing machines," *The journal of chemical physics,* vol. 21, pp. 1087-1092, 1953.

[107] D. E. Finkel and C. Kelley, "Convergence analysis of the DIRECT algorithm," *Optimization Online,* vol. 14, pp. 1-10, 2004.

[108] D. R. Jones, C. D. Perttunen, and B. E. Stuckman, "Lipschitzian optimization without the Lipschitz constant," *Journal of optimization Theory and Applications,* vol. 79, pp. 157-181, 1993.

[109] J. Na, Y. Lim, and C. Han, "A modified DIRECT algorithm for hidden constraints in an LNG process optimization," *Energy,* vol. 126, pp. 488-500, 2017.

[110] G. Lane, M. Schwarz, and G. M. Evans, "Numerical modelling of gas–liquid flow in stirred tanks," *Chemical Engineering Science,* vol. 60, pp. 2203-2214, 2005.

[111] J. Mockus, *Bayesian approach to global optimization: theory and*

applications vol. 37: Springer Science & Business Media, 2012.

[112] E. Brochu, V. M. Cora, and N. De Freitas, "A tutorial on Bayesian optimization of expensive cost functions, with application to active user modeling and hierarchical reinforcement learning," *arXiv preprint arXiv:1012.2599,* 2010.

[113] D. R. Jones, M. Schonlau, and W. J. Welch, "Efficient global optimization of expensive black-box functions," *Journal of Global optimization,* vol. 13, pp. 455-492, 1998.

[114] J. Svenson and T. Santner, "Multiobjective optimization of expensive-to-evaluate deterministic computer simulator models," *Computational Statistics & Data Analysis,* vol. 94, pp. 250-264, 2016.

[115] J. Bect, E. Vazquez, and others. (2017). *STK: a Small (Matlab/Octave) Toolbox for Kriging. Release 2.5.* Available: http://kriging.sourceforge.net

[116] F. Kerdouss, A. Bannari, and P. Proulx, "CFD modeling of gas dispersion and bubble size in a double turbine stirred tank," *Chemical Engineering Science,* vol. 61, pp. 3313-3322, 2006.

[117] A. Khopkar, A. Rammohan, V. Ranade, and M. Dudukovic, "Gas–liquid flow generated by a Rushton turbine in stirred vessel: CARPT/CT measurements and CFD simulations," *Chemical Engineering Science,* vol. 60, pp. 2215-2229, 2005.

[118] M. Ljungqvist and A. Rasmuson, "Numerical simulation of the two-phase flow in an axially stirred vessel," *Chemical Engineering Research and Design,* vol. 79, pp. 533-546, 2001.

[119] M. Ishii and N. Zuber, "Drag coefficient and relative velocity in bubbly, droplet or particulate flows," *AIChE Journal,* vol. 25, pp. 843-855, 1979.

[120] A. Bakker and H. Van den Akker, "A computational model for the gas-liquid flow in stirred reactors," *Chemical Engineering Research and Design,* vol. 72, pp. 594-606, 1994.

[121] V. Hudcova, V. Machon, and A. Nienow, "Gas–liquid dispersion with dual Rushton impellers," *Biotechnology and Bioengineering,* vol. 34, pp. 617-628, 1989.

Abstract in Korean (국문초록)

본 박사학위논문에서는 멀티 스케일 모델링, 실험 결과를 이용한 모델 보정법, 최적화 순으로 진행되는 산업용 화학 반응기의 설계 전략을 제시한다. 반응기는 화학 공정에서 제일 중요한 단위이지만, 그 설계에 있어서는 최신 수치적 기법들보다는 여전히 간단한 모델이나 실험 및 경험 규칙에 의존하고 있는 현실이다. 산업 규모의 반응기는 물리, 화학적으로 몹시 복잡하고, 관련 변수 간의 스케일이 크게 차이나는 경우가 많아 수학적 모델링 및 수치적 해법을 구하기가 어렵다. 모델을 만들더라도 부정확하거나 시뮬레이션 시간이 너무 긴 문제가 있어 최적화 알고리즘에 적용하기가 힘들다.

반응기 내 현상의 복잡성과 스케일 차이 문제는 멀티 스케일 모델링을 통해 접근할 수 있다. 전산유체역학 기반 구획 모델(CFD-based compartmental model)을 이용하면, 불균일한 혼합 패턴을 보이는 대형 반응기에서도 긴 시간 동안의 동적 모사가 가능하다. 이 모델은 큰 반응기를 완벽하게 균일한 작은 구획들의 네트워크로 간주하고, 각 구획을 반응 속도식들과 CFD 결과로부터 가져온 유동 정보가 포함된 질량 및 에너지 균형 방정식으로 표현한다. 기체, 액체, 고체 3상이 상호작용하며 복잡한 유동을 보이는 수성 광물 탄산화 반응기를 이 방법을 사용해 모델링하였다. 이 때 모델은 미분 대수 방정식(DAE)의 형태를 띠며, 메커

니즘 상 모든 반응들(기-액 간 물질 전달 반응, 고체 용해 반응, 이온 간 반응, 앙금 침전 반응)과 유체 역학, 반응열, 열역학적 변화 및 운전 상의 이벤트 발생을 모두 고려할 수 있다. 모델을 이용해 이산화탄소 제거 효율, pH 및 온도 변화를 예측하여 실제 운전 데이터와 비교한 결과, 파라미터를 통한 보정이 전혀 없이도 7 % 이내의 오차를 보여주었다.

모델의 부정확성 문제는 모델링 후 실험 결과를 이용한 모델 보정으로 극복 할 수 있다. 본 논문에서는 광물 탄산화 반응기 모델을 베이지안 보정(Bayesian calibration)을 통해 강화하는 방법을 제시한다. 먼저 모델 중 불확실한 부분에 8개의 파라미터를 도입한 후, 베이지안 파라미터 추정법(Bayesian parameter estimation) 및 실험실 규모에서의 실험 결과들을 이용하여 파라미터들의 사후 확률 분포를 추정하였다. 얻어진 파라미터의 확률 분포들은 모델 및 실험의 불완전성으로 인해 나타나는 파라미터의 불확실성 및 다중 봉우리 특성을 반영하고 있다. 이를 이용하여 실험 결과를 잘 따라가는 확률론적 모델 예측치(stochastic model response)를 얻을 수 있었다. 16개의 실험 데이터셋 및 테스트셋의 피팅 에러(fitting error)는 결정론적인 최적화 알고리즘(deterministic optimization)을 사용할 때보다 비슷하거나 낮은 것으로 측정되었다.

수학적 최적화에 쓰이기에 너무 긴 시뮬레이션 시간 문제는 베이지안 최적화 알고리즘을 적용하여 해결할 수 있다. 화학 반응기 설계 최적화를 위해 본 논문에서는 다중 목적 베이지안 최적화(Multi-objective

Bayesian Optimization, MBO)를 사용해 시뮬레이션 횟수를 최소화 하는 CFD 기반 최적 설계 방법을 제안하였다. 여섯 가지 설계 변수를 가지는 기-액 교반 탱크 반응기에서 전력 소비를 최소화하고 가스 분율(gas holdup)를 극대화하기 위해 이 방법을 이용한 결과, 단 100 회의 시뮬레이션 만으로 최적 파레토 커브(Pareto curve)를 얻을 수 있었다. 제안된 최적 설계안들은 문헌에 보고된 기존 반응기들과 비교해 뛰어난 성능을 보여주었다. .

본 논문을 통해 제안된 CFD 기반 구획 모델링법, 베이지안 모델 보정법 및 베이지안 최적화 방법은 복잡한 물리적 및 화학적 특징을 갖는 산업 규모의 화학 반응기에 적용될 수 있을 것으로 기대된다.

주요어: 반응기; 반응기 모델링; CFD 반응기 모델; CFD 기반 구획 모델; 베이지안 파라미터 추정; 베이지안 최적화; 반응기 최적 설계; 수성 광물 탄산화; 이산화탄소 포집 이용 저장 (CCUS)

학 번: 2015-21062